ANTI-HIV DRUG HUMAN BIOTRANSFORMATION AND STRUCTURE-ACTIVITY RELATIONSHIP OF PREGNANE X RECEPTOR ACTIVATION

By
Julie Maylor Lade

A dissertation submitted to Johns Hopkins University in conformity with the requirements for the degree of Doctor of Philosophy

Baltimore, MD
November 2016

Abstract

With the advent of antiretroviral drug therapy in the late 1980s, human immunodeficiency virus (HIV) is no longer a death sentence, but remains to be a chronic disease. Of concern, however, an estimated 2.1 million individuals were newly infected with HIV globally as of 2015. Further, HIV remains to be a pandemic that requires attention from scientific researchers to push forward the development of novel drug therapies that mitigate viral resistance and improve overall safety profiles. Rilpivirine (RPV) a second generation non-nucleoside reverse transcriptase inhibitor (NNRTI) was FDA approved in 2011 for administration to treatment-naïve HIV-infected individuals. Prior to this work, the hepatic metabolism of RPV was unknown. By *in vitro* assay, we observed that cytochrome P450s CYP3A4 and CYP3A5 primarily contributed to the oxidative metabolism of RPV and that uridine diphosphate glucuronosyl transferases UGT1A1 and UGT1A4 could contribute to the conjugative metabolism of RPV and its metabolites. In these studies, it was observed RPV could modulate CYP3A4 mRNA expression through activation of the nuclear receptor and xenobiotic sensor pregnane X receptor (PXR). In line with this, efavirenz (EFV) a first generation NNRTI and the most-widely prescribed antiretroviral despite exhibiting a poor safety profile, has been previously observed to activate PXR. Using an array of structural analogs of EFV, we explored the structure-activity relationship of EFV-mediated activation of PXR. In doing so, we identified a lower size limit ranging of > 223 Da to < 289 Da for ligand-dependent activation of PXR. In addition, we observed that the addition of a hydroxyl group to the Cl-phenyl ring of EFV did not impede ligand binding but attenuated PXR activation potentially through destabilizing a key hydrophobic area within the ligand-binding

pocket. Building upon this work, we investigated other hepatic pathways that may be stimulated by EFV and/or impacted by PXR activation. To this end, we observed EFV, but not RPV, could disrupt hepatic cholesterol homeostasis by stimulating lipid droplet formation as evidenced in primary mouse hepatocytes. EFV was also observed to increase the expression of the nuclear receptor small heterodimer partner (SHP), which has been implicated in facilitating the developments of dyslipidemia. However, further studies need to be performed in order to determine whether an EFV-mediated increase of SHP has a causal role in lipid droplet formation. In addition to studying antiretrovirals within the context of chronic HIV maintenance therapy, we also investigated RPV and the nucleoside reverse transcriptase inhibitor tenofovir (TFV) as pharmacological agents for HIV pre-exposure prophylaxis (PrEP). Moreover, in retrospective analyses, we identified genetic variants in the genes encoding enzymes responsible for RPV and TFV metabolism and activation, respectively. These findings lay the groundwork for future pharmacogenetic studies investigating inter-individual variability and toxicity associated with HIV PrEP.

Doctoral advisor:	Dr. Namandjé N. Bumpus
Thesis readers:	Dr. Namandjé N. Bumpus
	Dr. Herschel V. Wade
Thesis committee:	Dr. Namandjé N. Bumpus
	Dr. Craig W. Hendrix
	Dr. Herschel V. Wade
	Dr. G. William Wong

Copyright Disclaimer

Acknowledgements

Over the past four and a half years of graduate school, I have received an infinite amount of support and encouragement from several individuals at Johns Hopkins University. Most importantly, however, I would like to thank my thesis advisor, Dr. Namandjé Bumpus. I will forever be indebted to her for the numerous sacrifices she has made in order to facilitate my own progression. Under her training, I was able to cultivate confidence in my own scientific abilities and comprehension as well as in my written and oral communication skills. This was in part due to the countless opportunities that arose through Namandjé, ranging from attending national and international conferences to completing an internship at a high-profile pharmaceutical company. The overall breadth and depth of training I have received under Namandjé's mentorship not only has primed me for a successful career in science, but has especially molded me into a well-rounded and informed member of society.

I would also like to thank my thesis committee members Dr. Craig Hendrix, Dr. Herschel Wade and Dr. Will Wong. I feel extremely lucky to have had the opportunity to receive guidance and inspiration from such accomplished scientists. In particular, I would like to thank Herschel for truly going above and beyond as a committee member, and I am very grateful for his mentorship throughout my ultimate year of graduate school.

In addition to my advisor and thesis committee members, I am thankful for the support I have received from the entire Pharmacology & Molecular Sciences department, especially the administrative staff who has demonstrated immense dedication to facilitating all graduate students to succeed by allowing us to focus on our research.

Table of Contents

List of Tables

List of Figures

Chapter 4

Chapter 1: Introduction

HIV Maintenance Therapy and Pre-Exposure Prophylaxis

With the advent of antiretroviral drug therapy in the late 1980s, human immunodeficiency virus (HIV) is no longer a death sentence, but a chronic disease that can be alleviated pharmacologically (1). That being said, as of 2015, the Joint United Nations Programme on HIV/AIDS estimated 2.1 million individuals were newly infected with HIV globally, with the greatest prevalence of infections occurring in eastern and south Africa (2). Further, within the scope of the United States, over 1.2 million Americans are reported to be HIV infected, with approximately 50,000 new infections occurring annually (3). These alarming statistics demonstrate HIV remains to be a global pandemic that requires attention from scientific researchers to push forward the development of novel drug therapies that mitigate viral resistance and improve overall safety profiles.

Several druggable targets of the HIV replication cycle have been elucidated to date, however, the most pharmacologically exploited steps of the HIV lifecycle are viral entry, reverse transcription of viral RNA, integration of viral DNA into the host cell genome, transcription of proviral DNA, viral assembly as well as proteolytic processing (4). Zidovudine, a thymidine analog that competitively inhibits the HIV reverse transcriptase enzyme, was the first FDA-approved drug for the treatment of HIV infection as a monotherapy in 1987 (1, 5). Nearly a decade later, a clinical trial demonstrated that zidovudine dosed in combination with lamivudine, a cytidine analog that also targets the HIV reverse transcriptase enzyme, improved drug efficacy in terms of viral suppression and resistance in addition to immunologic response compared to

when either agent was administered independently to HIV-infected patients (6). Since these initial findings, current clinical guidelines by the World Health Organization (WHO) have evolved to recommend a triple drug combination as first-line antiretroviral therapy consisting of two nucleoside/nucleotide reverse transcriptase inhibitors (NRTIs) plus a non-nucleoside reverse transcriptase inhibitor (NNRTI) (7).

Unlike NRTIs, NNRTIs non-competitively inhibit HIV reverse transcriptase by binding allosterically to a hydrophobic binding pocket causing a conformational change and rendering the enzyme inactive. Efavirenz (EFV; Figure 1) is a first-generation NNRTI FDA-approved in 1998 and remains to be the most prescribed antiretroviral worldwide. This is primarily impart to WHO guidelines that recommend EFV be dosed as a third agent to treatment-naïve HIV-infected adults in combination with two NRTIs tenofovir disoproxil fumarate and emtricitabine (7). Further, this coformulated tablet, marketed as Atripla^{TM}, was the first triple drug combination approved by the FDA for treating HIV infection (8). Yet, despite being the most widely prescribed antiretroviral, EFV is associated with several serious adverse events, the most notably being psychiatric and nervous system symptoms, rash, hepatotoxicity and dyslipidemia (9). A dose reduction study comparing 400 mg EFV to the standard of care 600 mg EFV-containing once-daily drug regimen demonstrated an improved toxicity profile and fewer treatment discontinuations without compromising viral suppression, however, the relatively high risk for the emergence of treatment-resistance mutations has continued to drive the development of new antiretroviral therapies (10).

Rilpivirine (RPV; Figure 1) is a second-generation NNRTI that was one of a family of diarylpyrimidine (DAPY) small molecules designed using a novel

multidisciplinary approach by Janssen Pharmaceuticals (11). This drug class has an inherent degree of flexibility and rotational freedom that enable the DAPY molecules to bind in multiple modalities to the NNRTI binding pocket of the HIV reverse transcriptase enzyme thereby allowing for adaptation to potential resistance mutations (11). By *in vitro* assay, RPV was observed to be 10 to 20 times more potent than EFV towards the inhibition of wild-type HIV reverse transcriptase and, more compelling, phase II clinical trials of once-daily dosing of RPV at 25, 75 and 150 mg all demonstrated a more favorable safety profile relative to 600 mg EFV once-daily dosing with decreased frequency of psychiatric and neurological adverse events as well as rash and lipid abnormalities (11, 12). RPV was eventually FDA-approved in 2011 for administration to treatment-naïve HIV infected adults. Further, because RPV was found to be highly efficacious and well tolerated with chronic oral administration, it was concurrently developed into a long-acting injectable formulation (RPV-LA) (13). One can envision that less frequent dosing of an antiretroviral due to an extended drug half-life may improve compliance as this is a primary contributor to the development of resistance. In addition to use for HIV maintenance therapy, RPV-LA is presently under investigation for use in pre-exposure prophylaxis (PrEP).

PrEP is a preventative drug strategy for uninfected adults at risk of acquiring HIV by either sexual or blood-born transmission. As of 2015, WHO guidelines recommend PrEP should be offered to populations with an HIV infection rate of 3 in 100 people per year, which includes but is not limited to serodiscordant couples, men who have sex with men, transgender women and people who inject drugs (14). The notion of dosing a healthy individual long-term with an antiretroviral first became most plausible with the

2001 approval of the NRTI tenofovir (TFV; Figure 1). TFV is a nucleoside monophosphate analog administered as the prodrug TFV disoproxil fumarate (TDF) due to poor oral bioavailability and is generally well-tolerated with the exclusion of rare incidences of renal toxicity as well as decreased bone density with chronic administration (15-17). To counter these potential risks associated with long-term exposure to TFV, a key benefit of this NRTI is the extensive intracellular half-life of its active metabolite, TFV-diphosphate, ranging from 60 to > 175 h, which may contribute to improved efficacy and allow for flexibility in dosing frequency (18).

Moreover, as TFV was proven to be an effective agent for use in treating HIV infection, it became a clear candidate for further exploration in PrEP under varying formulations and in differing target populations. For example, the CAPRISA 004 trial provided the first evidence that a 1% TFV microbicide gel applied vaginally before and after sex could reduce the risk of infection by 39%, 54% when corrected for adherence, in HIV-uninfected women (19). TFV, however, is only approved for oral administration as the prodrug TDF and is commonly coformulated with the nucleoside analog emtricitabine (FTC) as a backbone for NNRTIs, such as EFV and RPV, for HIV maintenance therapy. To that end, the Preexposure Prophylaxis Initiative (iPrEx) trial was the first study to report efficacy for oral dosing of TDF-FTC in seronegative men and transgender women, observing a 44% risk reduction in HIV transmission, an overall 92% reduction when adjusting for detectable levels of TFV in blood (20). Taking this work a step further in serodiscordant couples, our laboratory contributed to the Partners PrEP study showing once-daily TDF alone or TDF-FTC decreased the rate of HIV infection by 67% and 75%, respectively, with a greater than 85% relative risk reduction in participants who had

detectable TFV concentrations in blood regardless of the formulation (21). Furthermore, the data acquired from pivotal clinical trials, such as iPrEx and Partners PrEP, clearly demonstrated that the coformulation of TDF-FTC is effective at reducing the risk of HIV infection through sexual transmission giving way to Truvada as the first, and currently the only, approved drug for HIV PrEP in 2012 (22). As has been aforementioned, TFV as well as other classes of antiretrovirals remain to be under intensive investigation for indication in HIV PrEP with > 40 open label, demonstration and implementation projects reported to be planned or underway across Africa, Europe, Latin America and the United States as of June 2016 (23).

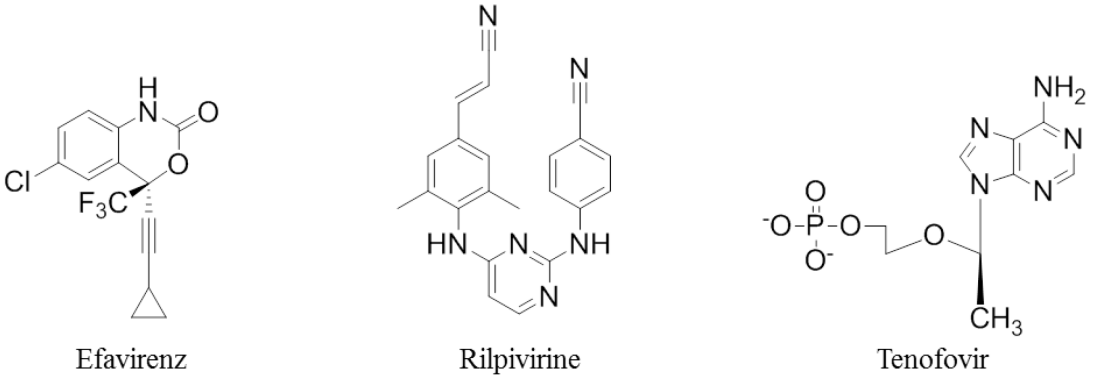

Figure 1. Structural comparison of NNRTIs efavirenz and rilpivirine and the NRTI tenofovir. EFV is a first-generation NNRTI and is the most widely-prescribed antiretroviral to date. RPV is a second-generation NNRTI that has an increased genetic barrier to resistance relative to EFV as well as an improved safety profile. Both EFV and RPV are coformulated with the prodrug of TFV known as TFV disoproxil fumarate and emtricitabine (not shown) marketed as Atripla™ and Complera™, respectively, for administration to treatment-naïve HIV-infected adults. In addition, the coformulation of

TFV disoproxil fumarate and emtricitabine alone, also known as Truvada, is the only FDA-approved drug strategy for HIV pre-exposure prophylaxis.

Pharmacokinetics and Small Molecule Drug Metabolism

The most common routes for drug administration are (1) enteral by oral ingestion, in which the drug passes through the gastrointestinal tract prior to reaching systemic circulation, (2) parenteral injection, in which the drug rapidly reaches systemic circulation and (3) topical application, in which drug exposure is localized and may or may not reach systemic circulation. Regardless of the route of administration, each drug will have its own unique pharmacokinetic parameters for absorption, distribution, metabolism and elimination (Figure 2). Although there are limitations, oral dosing in general is considered the safest, most convenient and most economical route of administration for medications. All currently approved anti-HIV drugs for both maintenance therapy and PrEP are small molecules (< 900 Da) dosed orally; therefore, the pharmacokinetic properties most relevant to oral tablets will be described herein.

Absorption is the movement of drug from the site of administration into the bloodstream. Following ingestion of a drug, there are several mechanisms by which a small molecule can traverse cell membranes for absorption into the gastrointestinal tract, those being passive or facilitated diffusion as well as active transport. Orally dosed drugs tend to be highly lipophilic and, therefore, will passively diffuse across lipid bilayers driven by the concentration gradient. The rate at which this occurs is primarily regulated by the surface area at the site of absorption. The intestinal mucosa, for example, has a large surface area thereby facilitating rapid absorption. The overall absorption of a drug determines its bioavailability, which is the extent to which a drug can access its site of

action when administered orally. Drugs that are readily absorbed by the stomach and the intestinal wall will be transported through the portal vein into the liver. Drug metabolizing enzymes highly expressed in the liver can then biotransform the parent drug into an inactive metabolite ultimately decreasing the amount of active drug that reaches systemic circulation to take pharmacological effect. This phenomenon is commonly referred to as "first-pass metabolism" and can have a significant impact on drug bioavailability. Following absorption into the bloodstream, a drug can distribute from the systemic circulation and permeate into extra- and/or intra-cellular spaces. A compound will distribute to highly perfused organs, such as the heart, liver, kidney and brain, more quickly after absorption has occurred compared to less perfused tissues, such as muscle and fat. The rate of blood flow to these organs and tissues will further impact the extent of distribution that takes place. In addition, the concentration of "free" drug actually distributed to the periphery and ultimately the site of action is directly dependent upon the degree of plasma protein binding.

As previously mentioned, drugs absorbed by the stomach or intestinal wall will be subjected to first-pass metabolism. This is a process in which a lipophilic molecule is biotransformed into a more polar species in order to facilitate excretion. Moreover, a polar compound will have physiochemical properties less favorable for reabsorption by the kidneys to reenter the bloodstream. This is presumably an evolved defense mechanism of the body's in order to prevent the recirculation of potentially toxic foreign substances. That being said, although drug metabolites usually do not exert a biological effect, drug metabolizing enzymes do have the propensity to catalyze the formation of unstable and/or toxic metabolites. A well-studied example of this phenomenon is the

reactive metabolite *N*-acetyl-*p*-benzoquinoneimine formed from the cytochrome P450-dependent metabolism of acetaminophen (25). The biotransformation of xenobiotics primarily occurs in the hepatocytes of the liver and to a lesser extent in the intestinal epithelium due to the high concentration of drug metabolizing enzymes in these organs. Further, the biotransformation of drugs can be categorized into two types of mechanisms, phase I and phase II reactions, which do not imply order but the type of modifications that can occur to a substrate (Figure 3). Phase I drug metabolizing enzymes catalyze "functionalizing" reactions in which a functional group, such as –OH, $–NH_2$ and –SH, is introduced to or unmasked on a substrate, whereas phase II drug metabolizing enzymes are generally transferases and conjugate an endogenous, polar cofactor onto a substrate (26). As previously alluded to, phase I and phase II metabolism can occur either sequentially or concurrently, conceivably yielding several metabolites for each parent drug. With respect to anti-HIV drugs, our laboratory alone has demonstrated the NNRTIs, EFV, RPV, etravirine and dapivirine, as well as the HIV entry inhibitor maraviroc undergo extensive phase I and phase II metabolism (27-31).

The cytochromes P450 are heme-containing monooxygenases that insert an oxygen onto a substrate and are responsible for 75% of phase I metabolism, with more marginal contribution by alcohol dehydrogenases, esterases, aldehyde dehydrogenases, epoxide hydrolases, NADPH:quinone oxidoreductases and dihydropyrimidine dehydrogenases (32). Uridine diphosphate glucuronosyltransferases contribute to approximately 30% of phase II reactions through the conjugation of glucuronic acid onto its substrate, producing a glucuronide. Sulfotransferases are then responsible for an estimated 25% of phase II reactions followed by glutathione S-transferases, N-acetyl

transferases, catechol *O*-methyl transferases and thiopurine methyl transferases (32, 33). Several of these drug metabolizing enzymes are highly polymorphic thereby modifying the biotransformation of a drug. The presence of such genetic variants can lead to heterogeneity in the way in which an individual may respond to a medication in terms of efficacy and/or toxicity.

Following absorption, distribution and metabolism, an ingested drug is eventually excreted from the body either unchanged or as a more polar metabolite. The process of elimination can occur through several biological fluids, mainly urine, bile or feces. In addition, depending on the physiochemical properties of parent drug and/or metabolites, elimination can also occur through excretory gland secretion, such as sweat, saliva, tears as well as breast milk. Renal excretion, however, is considered to be the primary route by which a drug and its metabolites are eliminated followed by biliary and fecal excretion.

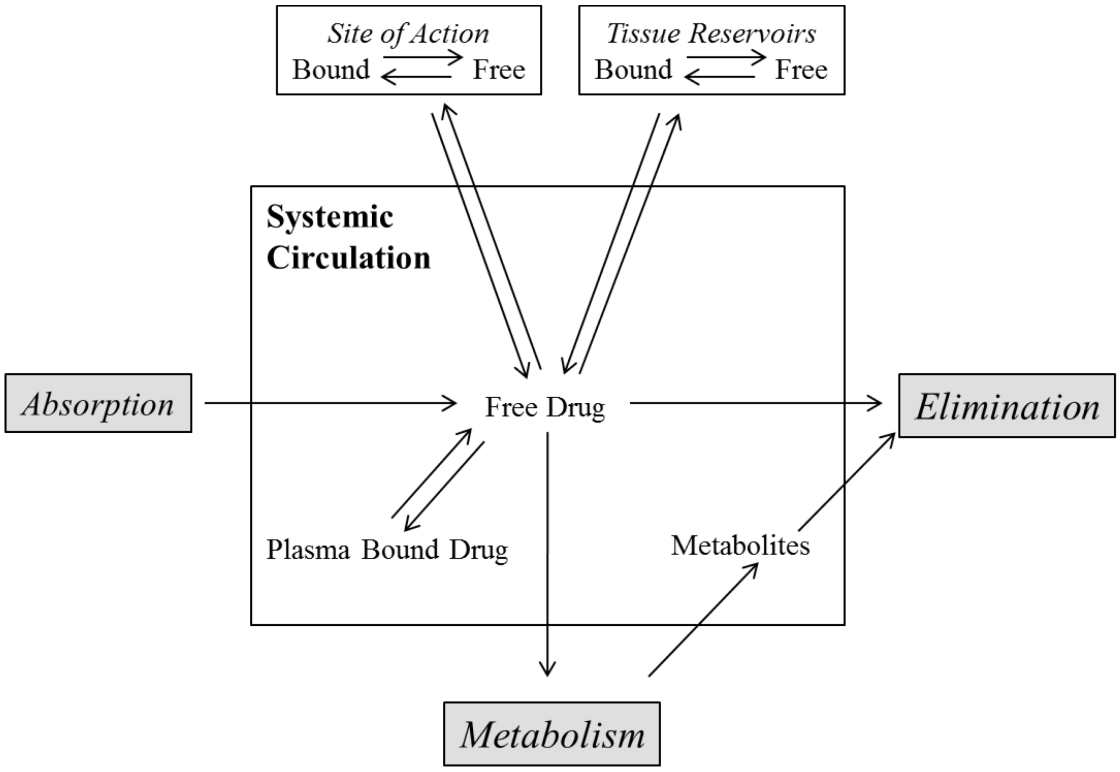

Figure 2. Pharmacokinetic parameters of a drug. Schematic demonstrating the interrelationship of absorption, distribution, metabolism and elimination of a drug. These four pharmacokinetic properties are unique to each drug and the extent and rate at which these processes occur will be dependent on the route of administration. (Schematic adapted from Goodman and Gilman's The Pharmacological Basis of Therapeutics (24).)

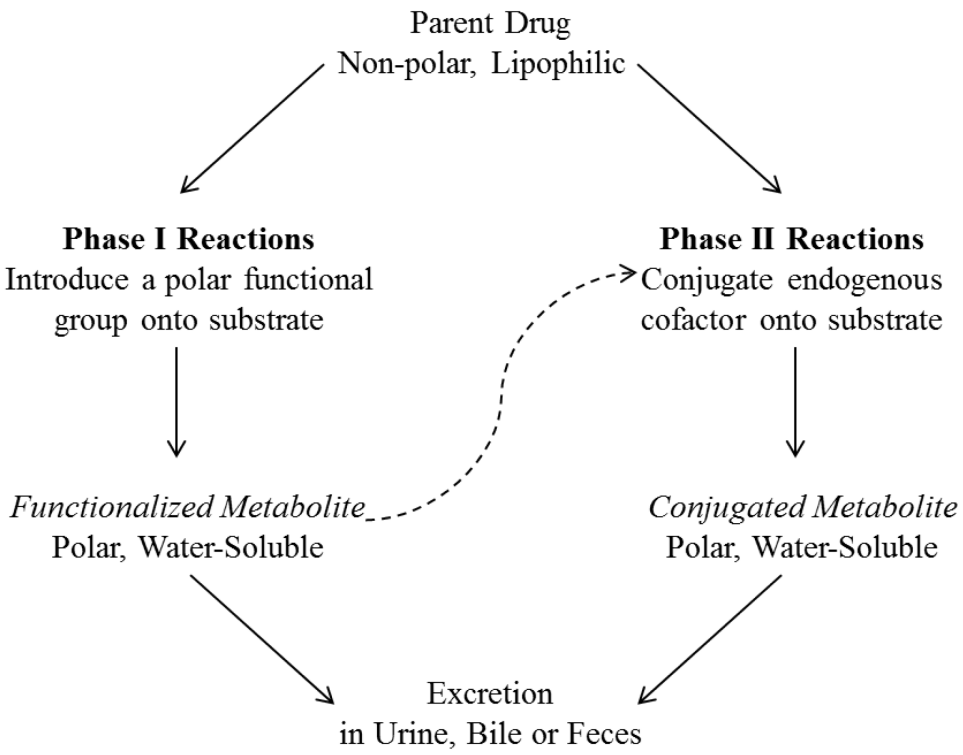

Figure 3. Phase I and phase II biotransformation. Drug metabolizing enzymes can be classified into catalyzing two types of mechanisms, phase I and phase II reactions. Phase I enzymes either introduce or unmask a polar functional group onto their substrates, whereas phase II enzymes conjugate an endogenous cofactor onto their substrates. Both mechanisms yield a metabolite with increased polarity relative to the parent drug in order to facilitate excretion from the body.

The Cytochromes P450

A "microsomal carbon monoxide-binding pigment" was first observed in rat subcellular liver fractions in the late 1950s (34). Shortly thereafter, in 1962, this heme-containing pigment was further characterized and designated as "cytochrome P450" (P450) due to the characteristic red tint of the microsomes enriched with this protein and the distinct absorption of light at 450nm in the presence of carbon monoxide (35). In

rapid succession, the first reports describing P450 function were published demonstrating monooxygenation of both endogenous and exogenous substrates, such as the steroid hormone 17-hydroxyprogesterone and the analgesic acetanilide, respectively (36, 37). P450s, now preferably termed "heme-thiolate proteins" as will be later discussed, are an established superfamily of enzymes, with over 18,000 protein-coding genes identified in nature thus far (38, 39). Due to the extensive diversity of P450s, each isozyme of the superfamily is identified using a specific gene nomenclature. A P450 is named starting with the gene symbol "CYP" for cytochrome P450, followed by an Arabic number designating the P450 family, then a letter indicating the subfamily, and lastly an Arabic number specific to the individual gene, for example, CYP3A4 (38). P450s within a given family share > 40% amino acid sequence identity and > 55% amino acid sequence identity for subfamilies (38). The human genome itself comprises of 18 P450 families and 44 subfamilies, encoding a total of 57 putatively functional genes (39).

Mammalian P450s are localized in subcellular compartments, primarily in the endoplasmic reticulum and to a lesser extent the inner mitochondrial membrane (39, 40). Moreover, P450s are highly concentrated in hepatocytes, the parenchymal cell of the liver, with certain isozymes also expressed in a range of extrahepatic tissues, such as the intestines, kidneys, testes and uterus to name a few (41). Microsomal P450s are anchored to the ER membrane by their N-terminus exposing the remainder of the polypeptide to the cytosol, whereas mitochondrial P450s are synthesized in the cytoplasm as soluble precursors, imported into the mitochondria, proteolytically processed and then incorporated into the inner membrane (42, 43). Interestingly, conversely to higher order eukaryotic P450s that are restricted to a subcellular membrane, prokaryotic P450s are

soluble enzymes that lack an N-terminal membrane anchor. Moreover, the relative ease in the expression and purification of bacterial P450s allowed for the swift progression of structural studies with first high-resolution P450 crystal structure solved in 1987 of P450cam isolated from *Pseudomonas putida* (44).

Although differing in terms of cellular localization and solubility, P450s across all eukaryotic and prokaryotic organisms exhibit a similar tertiary structure arranged in a series of helices and folds, with the most conserved helices denoted as A through L (45). Helices I and L contact the active site heme, and helices B, F and I can form electrostatic interactions with the substrate, thereby influencing catalytic selectivity as demonstrated through extensive site-directed mutagenesis experiments (45). At the level of the primary structure, the most conserved amino acid residue across P450s is a cysteine residue that acts as a thiolate ligand to the heme iron, hence the preferred terminology of "heme-thiolate protein" as previously mentioned (45). A somewhat less conserved amino acid is a threonine residue, which can donate a proton during substrate oxidation in the P450 catalytic cycle (45).

P450s primarily catalyze mixed-function oxidation reactions, in which an oxygen is inserted onto their substrate using molecular oxygen and NADPH as an electron source (45). The major events of the P450 catalytic cycle can be grossly simplified into a series of nine steps (45) (Figure 4). The cycle begins by the binding of substrate in proximity to the active site heme iron poised for catalysis in the ferric state (Fe^{+3}) (45). An electron is then transferred to the ferric iron from NADPH via a neighboring accessory protein NADPH-P450 reductase, yielding reduced ferrous (Fe^{+2}) iron and forming an unstable intermediate with molecular oxygen (45). A second electron is then transferred to the

Fe^{+2}-O_2 complex by either NADPH-reductase or an alternative redox partner cytochrome b_5, followed by the addition of a proton from surrounding water or a nearby threonine residue, cleavage of the O-O bond and formation of one water molecule (45). The resulting P450-compound intermediate undergoes a series of rearrangements, yielding oxidation of the substrate and release of a hydroxylated product (45). It is important to note, that the P450 catalytic cycle can become "uncoupled" once molecular oxygen is bound to the ferrous iron, producing superoxide as well as hydrogen peroxide byproducts, and the extent to which this uncoupling occurs impacts the rate of catalytic efficiency and substrate turnover (46). That being said, the most common oxidation reactions that result from the P450 catalytic cycle are carbon hydroxylation, heteroatom (N, S, P or I) oxygenation, heteroatom release or dealkylation following hydroxylation of an adjacent carbon atom and epoxidation (45).

Although P450s generally exhibit similar tertiary structure, they do differ substantially in terms of active site size even within the same species. For example, the active sites of human P450s 2E1 and 3A4 range from 190 $Å^3$ to 1385 $Å^3$ in volume, respectively (47, 48). In addition to size, P450 active sites can also vary drastically in three-dimensional shape as well, with the human P450 2C8 observed to have an L-shaped cavity compared to P450 3A4 which exhibits a more open cavity (40). Taken together, both the size and shape of the hydrophobic P450 active site are key determinants for substrate specificity. While human P450s tend to exhibit substrate overlap, families 1 through 4 are commonly considered to primarily contribute to xenobiotic metabolism, whereas the remaining P450 families are responsible for the metabolism of endogenous

compounds such as sterols, fatty acids, eicosanoids and vitamins in addition to several orphan P450s with unknown biological function (40).

Reiterating the former discussion of first-pass drug metabolism, human P450s contribute to roughly 75% of phase I biotransfromation (32). There are a total of 16 P450s expressed at the protein level in the human liver and these isozymes are ranked here in order of relative hepatic content from lowest to highest concentration: CYP2C18, -2J2, -3A43, -1A1, -3A7, -2C19, -4F2, -2D6, -2B6, -3A5, -2C8, -2A6, -1A2, -2C9, -2E1 and -3A4 (49-51). Drawing from the literature, the major hepatic isozymes that participate in the metabolism of drugs either under development or currently on the market are the P450s 3A4 (27%), 2D6 (13%), 2C9 (10%), 2C19 (9%) and 1A2 (9%), with more minor contribution from the P450s 3A5 (6%), 1A1 and 2C8 (5%), 2B6 (4%), 2E1 (3%) and 2A6 (2%) (52). From these data, one can see that the CYP3A subfamily account for the largest fraction of P450-mediated drug metabolism which allows for an increased frequency of potential drug-drug interactions. Of additional concern, the highly polymorphic P450s 2D6 and 2C19 combined account for almost the second largest fraction of P450-metabolited drug metabolism, allowing for greater heterogeneity or inter-individual variability in the response to a medication.

The common occurrence of polymorphisms in drug metabolizing enzymes, particularly in P450s, gave rise to the practice of "pharmacogenetics," in which the existence of a genetic variant for a drug metabolizing enzyme is translated into a predicted outcome or drug response (53). Variants in the genes encoding these enzymes can result in amino acid mutations that cause high, low or no activity towards a substrate due to decreased expression or loss-of-function of the enzyme at the protein level

allowing for a profound effect on toxicity and efficacy of a drug. In the past, clinically relevant polymorphisms in enzymes responsible for drug metabolism and disposition were initially identified by phenotypic observation in a study population administered drug (32). Presently, functionally important polymorphisms are typically elucidated pre-clinically using basic molecular pharmacology techniques. For example, individual cDNA-expressed hepatic P450s, mainly for CYP1A2, -2B6, -2C8, -2C9, -2C19, -2D6, -3A4 and -3A5, are commonly employed to determine their relative contribution to a drug's oxidative metabolism. If a polymorphic P450 is found to metabolize an investigational new drug, then this work can be taken a step further into a more complex system using genotyped human liver microsomes, allowing for a better representation of the global impact of the polymorphism on hepatic metabolism and for potential extrapolation to an *in vivo* outcome. An excellent proof of concept of this method for identifying clinically relevant polymorphisms was recently demonstrated by our laboratory in which we found that the HIV entry inhibitor maraviroc was primarily metabolized by the polymorphic P450 3A5 by *in vitro* assay (28). We then translated this work *in vivo* and observed the presence of a CYP3A5 loss of function allele significantly increased maraviroc plasma concentrations and decreased clearance (54). Moving forward, although the regulation of P450 expression and activity is multifactorial, there is a clear utility for understanding genotype-phenotype correlations in order to better predict clinical outcomes.

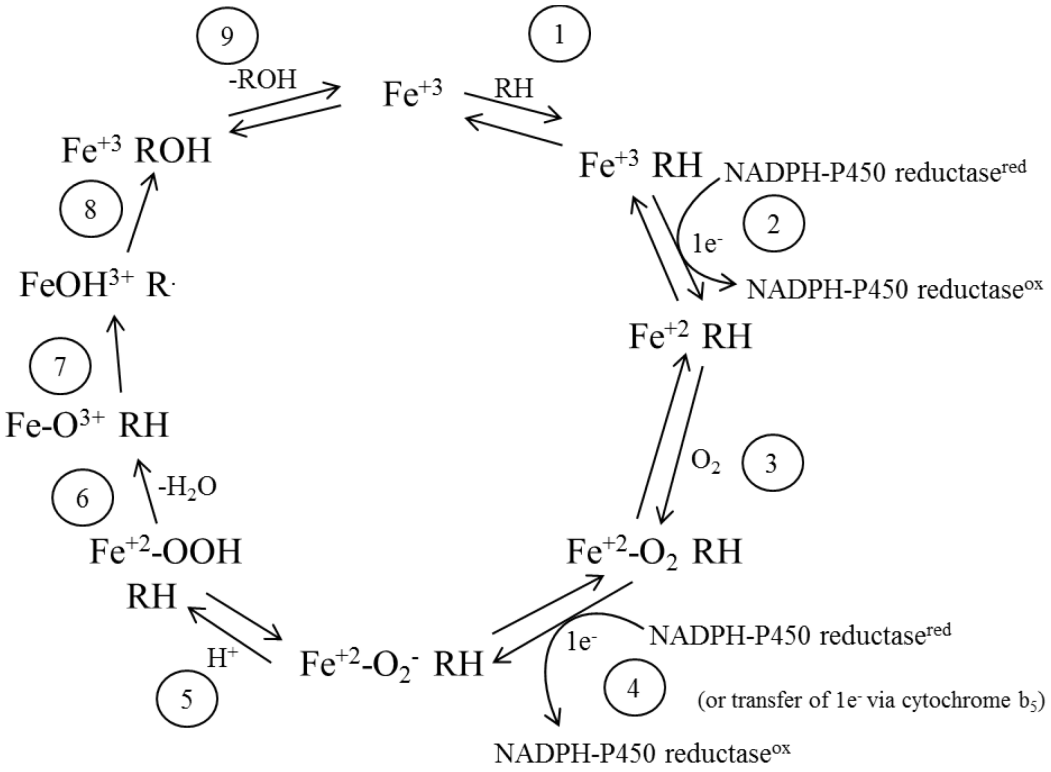

Figure 4. The cytochrome P450 catalytic cycle. Schematic demonstrating the nine primary events of the P450 catalytic cycle. The substrate (RH) binds in proximity to the ferric heme causing a conformational change and inducing an electron transfer from NADPH-P450 reductase. Molecular oxygen binds to the now ferrous heme, which then undergoes a second electron transfer from either NADPH- P450 reductase or cytochrome b_5. This is followed by rapid protonation, release of water and formation of a P450-compound intermediate. Following a series of rearrangements, this intermediate yields oxidation of the substrate and is ultimately released as a hydroxylated product. (Schematic adapted from F. Peter Guengerich, Common and Uncommon Cytochrome P450 Reactions Related to Metabolism and Chemical Toxicity (45).)

Uridine Diphosphate Glucuronosyltransferases

In contrast to the extensive studies published characterizing the cytochromes P450, uridine diphosphate glucuronosyltransferases (UGTs) have been historically less well investigated. Glucuronidation, however, is indeed a major detoxification pathway that has evolved to conjugate endogenous molecules, most notably bilirubin, and a wide-array of pharmacological agents, such as morphine and acetaminophen (55, 56). Similarly to P450s, however, UGTs are a superfamily of enzymes expressed in all kingdoms of life and as such require the utilization of a gene nomenclature for the identification of individual isozymes. A UGT is named starting with the gene symbol "UGT" for uridine diphosphate glucuronosyltransferase, followed by an Arabic number designating the UGT family, then a letter indicating the subfamily, and lastly an Arabic number specific to the individual gene, for example, UGT1A1 (57). UGTs within a given family share > 45% amino acid sequence identity and > 60% amino acid sequence identity for subfamilies (57). The human genome itself comprises of four UGT families, UGT1, -2, -3 and -8, encoding a total of 22 putatively functional genes (58, 59).

Mammalian UGTs are almost exclusively localized to the endoplasmic reticulum (ER) and, in parallel to P450s as well as other drug metabolizing enzymes, are highly expressed in hepatocytes (60). Although glucuronidation primarily occurs in the liver in addition to the intestines, UGTs are also expressed in a variety of extrahepatic tissues, such as the brain, kidneys, prostate and uterus (61, 62). In the initial studies of this superfamily, two opposing hypotheses were formed regarding the topology of UGTs. The first hypothesis proposed the enzyme is buried in the ER membrane and transport of the substrate across the membrane is required in order to reach the catalytic site, contrary to

the alternate hypothesis which proposed the enzyme is extensively membrane bound, however, the catalytic site is freely exposed to the cytosol for substrate binding (63-65). Subsequent studies observed UGT activity was proportional to substrate lipophilicity, suggesting the presence of a membrane barrier preventing access of hydrophilic substrates to the enzyme's active site (66). The implementation of cDNA cloning in addition to the use of hydropathy analyses put forth the current topological model that the enzyme is indeed located within the ER membrane (63). It is now well-accepted that UGTs are synthesized as precursors containing an N-terminal signal peptide, thereby mediating integration of the polypeptide into the ER membrane (67). The signal peptide is then cleaved, yielding a 505 residue transmembrane protein, with approximately 95% of the polypeptide chain retained in the lumen of the ER and a 20 residue C-terminal cytoplasmic tail (68, 69). Interestingly, across all UGTs there is a highly conserved 44 residue long region in the C-terminus and the cytoplasmic portion of this signature sequence is the proposed binding site for the nucleotide moiety of uridine diphosphate glucuronic acid (UDPGA) (57, 70). Unfortunately, obtaining further structural detail of UGTs has remained a challenge due to the protein's extensive membrane binding.

The general mechanism catalyzed by UGTs can be reduced to a second order nucleophilic substitution reaction, in which a substrate or aglycone attacks UDPGA at the electrophilic C_1 position of the sugar yielding a glucuronide conjugate and a uridine diphosphate byproduct (Figure 5) (71). The UDPGA cofactor is synthesized exclusively in the cytosol from UDP-glucose mediated by UDP-glucose-6-dehydrogenase (60). In addition, recent studies have demonstrated UGTs have the ability to conjugate other endogenous uridine-based sugars to their substrates, such as glucose and xylose (71).

Several substrate nucleophiles can serve as an acceptor functional group for glucuronic acid primarily aliphatic alcohols, phenols, carboxylic acids, aromatic or aliphatic amines, and thiols (71).

As previously discussed, there is substantial experimental evidence demonstrating the UGT active site is located within the lumen of the ER, however, data is severely lacking in regards as to how charged and bulky species, mainly UDPGA and the resulting glucuronide conjugate, move into and out of the luminal compartment, respectively. Over decades of work, studies using membrane vesicles have demonstrated and confirmed that active transport of UDPGA is certainly required to cross the microsomal membrane, yet the discrete membrane protein(s) responsible for its translocation remains ambiguous (72-75). UGT itself has been hypothesized to facilitate the efflux of glucuronide conjugates from the luminal space into the cytosol, however, there is no experimental evidence supporting this theory. One publication thus far has reported that glucuronides synthesized in the lumen of the ER can leave via an "antiport" driven by the concurrent uptake of UDPGA into the compartment though supporting evidence demonstrating the existence of such a protein carrier has not been published (76). In addition to these hypotheses, it is also highly probably that a glucuronide can bypass active transport and instead undergo vesicular trafficking from the lumen of the ER to the plasma membrane following a path similar to secreted proteins (63).

Of the four human UGT families, UGT1 and UGT2 members are expressed in the liver with the exception of UGT1A5, -1A7, -1A8, -1A10 and -2A1. Moreover, the most abundantly expressed hepatic isozyme is UGT2B4 (44.5% of total UGT hepatic content) followed by UGT2B15 (12.8%), -2B10 (10.6%), -2B7 (6.9%), -1A1 (6.7%), -1A9

(6.1%), -1A4 (4.9%), -1A6 (4.5%), -2B17 (1.5%) and -1A3 (1.3%) (71). As previously mentioned UGTs catalyze the glucuronidation of both endogenous and xenobiotic substrates and correspondingly to P450s tend to exhibit substrate overlap. For example, within the liver and intestines, UGT1A subfamily members actively conjugate bilirubin, steroid hormones and bile acids, with the exclusion of UGT1A5, -1A6 and -1A7 which have no known function (63). Further, UGT2B subfamily members also share activity towards steroid hormones and bile acids in addition to acidic steroids with no known endogenous substrate for UGT2B4 (63). With respect to drug metabolism, however, the most clinically relevant isozymes are UGT1A1, -1A3, -1A4, -1A6, -1A9 and -2B7, contributing to approximately 30% of phase II drug-conjugating reactions (32, 33, 71). Similarly to P450s, several of the UGT isozymes are highly polymorphic and as such have been correlated to the establishment of a disease state and/or interindividual variability for a drug response.

To date, genetic variants demonstrated to have a functional impact have been detected within the promoter and coding regions of *UGT1A1*, *-1A3*, *-1A4*, *-1A6*, *-1A7*, *-1A8*, *-1A9*, *-1A10*, *-2B7* and *-2B17* (71). Of these isoforms, polymorphisms within the gene encoding *UGT1A1* have been the most well-studied as the clinical manifestation of hyperbilirubinaemia is a direct result of reduced UGT1A1 protein expression and activity (77, 78). Bilirubin, a byproduct of red blood cell lysis, is toxic and lack of excretion in the bile as a glucuronide conjugate can result in kernicterus, a type of neurotoxicity due to high levels of circulating bilirubin, and even death if left untreated (79). Further, *UGT1A1* loss-of-function polymorphisms also have a causal role in the toxicity associated with administration of the chemotherapeutic agent irinotecan, due to

compromised clearance of the reactive metabolite SN-38 (80). As previously discussed within the context of P450s, functionally important polymorphisms for UGTs can also be elucidated pre-clinically. Individual cDNA-expressed hepatic and intestinal UGTs, mainly for UGT1A1, -1A3, -1A4, -1A6, -1A7, -1A8, -1A9, -1A10, -2B4, -2B7, -2B15 and -2B17 are routinely employed to determine their relative contribution to the glucuronidation of a drug. If a polymorphic UGT is found to conjugate an investigational new drug, then this work can be taken a step further into a more complex system using genotyped human liver microsomes, allowing for a better representation of the global impact of the polymorphism on hepatic metabolism and for potential extrapolation to an *in vivo* outcome.

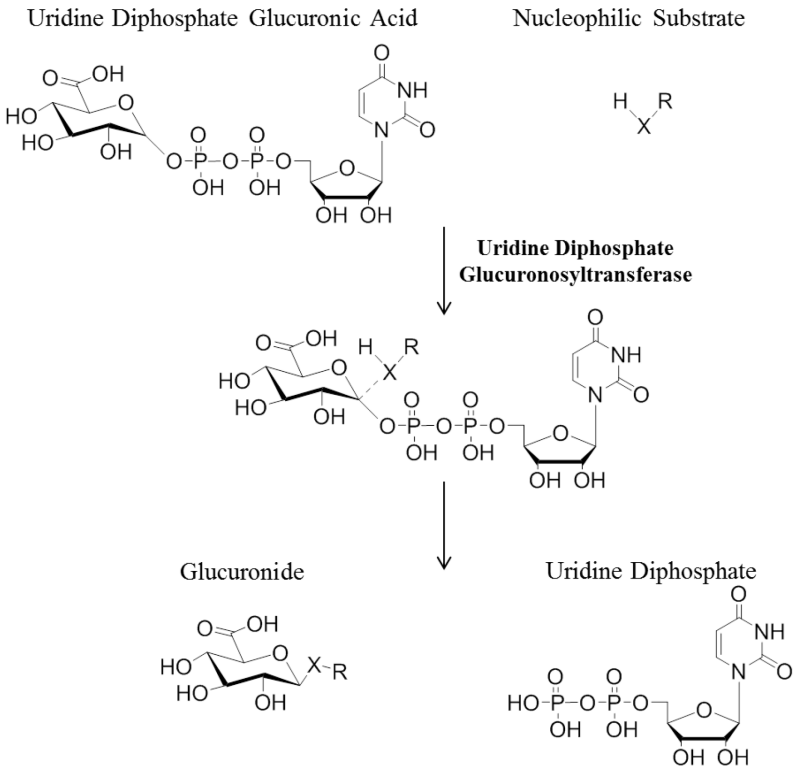

Figure 5. Mechanism of glucuronidation. Schematic demonstrating the conjugation of an aglycone (H-X-R) with uridine diphosphate (UDP) glucuronic acid. UDP-

glucuronosyltransferases covalently link an endogenous cofactor, glucuronic acid, to an acceptor functional group on a substrate through nucleophilic substitution, yielding a glucuronide conjugate and uridine diphosphate. (Schematic adapted from A. Rowland et al., The UDP-glucuronosyltransferases (71).)

Transcriptional Regulation of Drug Metabolizing Enzymes by the Pregnane X Receptor

The notion of a "general adaption syndrome" was put forth in the *Journal of Pharmaceutical Sciences* in 1971 describing a phenomenon in which the body has a physiologic response to a foreign stimulus initiating rapid induction of drug metabolizing enzymes to "destroy the aggressor" and accelerate its excretion (81). This "catatoxic effect" was believed to be distinct from classic hormonal action, yet correlated with increased levels of circulating glucocorticoids (81). Concurrent studies observed a similar effect *in vitro* demonstrating the induction of P450 and UGT activity through the treatment of isolated rat hepatocytes with the glucocorticoid dexamethasone and the anti-glucocorticoid pregnenolone 16α-carbonitrile (PCN), thereby suggesting activation of a cellular mechanism independent of the glucocorticoid receptor (82-85). Not until 1998 was the novel nuclear receptor, pregnane X receptor (PXR; NR1I2), first identified as the signaling pathway primarily responsible for the transcriptional modulation of these drug metabolizing enzymes (86).

PXR is part of an extensive superfamily of transcription factors that contribute to the regulation of cellular growth, development and homeostasis through either gene activation or repression. There are 48 nuclear receptors (NRs) expressed in humans, categorized into six subfamilies and further divided into 28 groups based on phylogeny

and sequence homology (87, 88). In a manner similar to the nomenclatures used for identifying P450s and UGTs, a receptor is named starting with the gene symbol "NR," followed by an Arabic number designating the subfamily, then a letter indicating the group, and lastly an Arabic number specific to the individual gene, such as the NR subfamily 1 group I member 2, or NR1I2, as an alternative name for PXR (89). NRs in general exhibit a modular structure organized into five to six domains, designated as A through F moving from N- to C-terminus, respectively (87). Of these domains, the most conserved regions are C, the DNA-binding domain (DBD) containing two zinc fingers, and E, the ligand-binding domain (LBD) which serves as the docking site for a ligand, and the coordinated actions of these domains culminate into the modulation of target gene expression (87).

PXR was first cloned from mouse liver, as a 431 residue long isoform PXR.1 and a 390 residue splice variant PXR.2, with both isoforms exhibiting high sequence homology with the human vitamin D receptor of 64% and 29% within the DBD and LBD, respectively (86). By northern blot analyses, murine PXR (mPXR) mRNA transcripts were highly abundant in the liver and intestines and to a lesser extent the stomach and kidneys, exhibiting an expression pattern similar to drug metabolizing enzymes (86). In addition, using a yeast-two hybrid system in which the LBD of mPXR was fused with the DBD of the yeast transcription factor GAL4, both isoforms were activated to varying degrees by dexamethasome and PCN, the same synthetic steroids previously reported to induce P450 and UGT activity in rodent hepatocytes (86). Taking this work a step further, pregnenolone was identified as a potent ligand of mPXR suggesting a pregnane was the likely natural ligand of the NR hence its namesake (86).

In rapid succession, two subsequent reports were published characterizing a 434 residue long human ortholog denoted simply as human PXR (hPXR) and formerly as the "steroid and xenobiotic receptor," respectively, with mRNA expression detected in the liver, intestines and colon (86, 90, 91). Interestingly, sequence alignments demonstrated hPXR exhibits 95% identity to the mPXR DBD, yet 73% identity to the mPXR LBD, suggesting an evolutionary divergence potentially pressured by exposure to toxins in the diets of rodents relative to primates (91). Adding to this observation, PCN was observed to have a low to modest activation of hPXR in contrast to the potent activation of mPXR, while rifampicin, an antibiotic used to treat tuberculosis, was an effective activator of hPXR but not mPXR (90, 91). The successive cloning of additional orthologs from rat and rabbit further demonstrated PXR is pharmacologically distinct due to sequence divergence in the LBD (92).

In the initial reports investigating PXR, it was observed that the NR requires heterodimerization with 9-cis retinoic acid receptor (RXR, NR2B1) in order to bind to response elements within the proximal and distal promoter regions of target genes, the most prototypic being *CYP3A*, to facilitate transcription (86, 90, 91). Its overall mechanism of action, however, was largely unknown until relatively recently and was primarily informed by preceding studies pertaining to the fellow NR1I group member constitutive androstane receptor (CAR; NR1I3), which has a less prominent role in the regulation of drug metabolism. Experimental evidence using a murine model has demonstrated that under basal conditions PXR is sequestered in the cytosol by the chaperones cytoplasmic CAR retention protein and heat shock protein 90 (Figure 6) (93, 94). Upon ligand binding, PXR dissociates from the chaperone protein complex and

translocates to the nucleus where it can then heterodimerize with RXR and bind to response elements in the promoter regions of target genes to facilitate transcription (95). PXR/RXR binding sites of a direct repeat (DR-3) and/or an everted repeat (ER-6) motif have been characterized in proximal promoter regions of *CYP3A* genes across species (96). In addition, to these proximal promoter binding sites, a distal xenobiotic response element consisting of DR-3 and ER-6 motifs has been extensively studied in the human *CYP3A4* gene (97). Although this is not an exhaustive list, PXR/RXR binding sites have also been detected in the promoter regions of other P450 subfamilies and drug metabolizing enzymes such as *CYP1A*, *CYP2A*, *CYP2B*, *CYP2C*, *CYP4F12*, the carboxyesterases *CES1* and *CES2*, *UGT1A1*, *UGT1A3*, *UGT1A6*, as well as the drug transporter multidrug resistance gene *MDR1* (98-103).

DNA binding, however, is spurred by ligand-dependent activation and to that end PXR requires broad ligand specificity in order to function as a "xenobiotic sensor." The first crystal structure of the hPXR-LBD were solved in 2001, which identified a unique 13 residue flexible loop (residues 309 to 321) flanking the ligand-binding cavity (Figure 7) (104). In addition, the ligand-binding pocket itself was estimated to have a volume of 1150 $Å^3$ and relatively hydrophobic in nature (104). Of the 28 residues that line the ligand-binding pocket, there are six polar amino acids that commonly form electrostatic interactions with ligands, Met243, Ser247, Gln285, Trp299, His407 and Phe420, with the large macrolide rifampicin (823 Da) making additional contacts to Ser208 and Arg410 (95). Interestingly, a single residue Leu308 adjacent to the flexible loop has been observed to confer hPXR ligand specificity through mutagenesis studies (105). Although extensive structural studies have been performed, experimental evidence is lacking as to

whether electrostatic interactions alone within the binding pocket are sufficient to stabilize an active conformation of the LBD. Steroid receptor coactivator 1 (SRC-1) is a coregulator that enhances NR-mediated transcription by acting as a weak histone acetyltransferase and facilitating the recruitment of basal machinery, such a CREB-binding protein and p300 (106, 107). SRC-1 contains three LXXLL motifs that can bind to the surface of PXR adjacent to a highly mobile AF-2 helix forming a stabilizing "charge clamp" (108). Previous work has demonstrated that the concurrent binding of a prototypic hPXR agonist SR12813 and a 25-mer SRC-1 peptide to the LBD exerted an additive effect on receptor stabilization as observed using circular dichroism thermal denaturation studies (108). However, despite mounting structural studies, predicting ligand regulation of PXR remains to be a confounding problem for drug discovery and development. Extensive structure-activity studies of novel PXR activators are required in order to identify key pharmacophores that may inform the design of pharmacological agents that attenuate PXR activation without compromising target site activity.

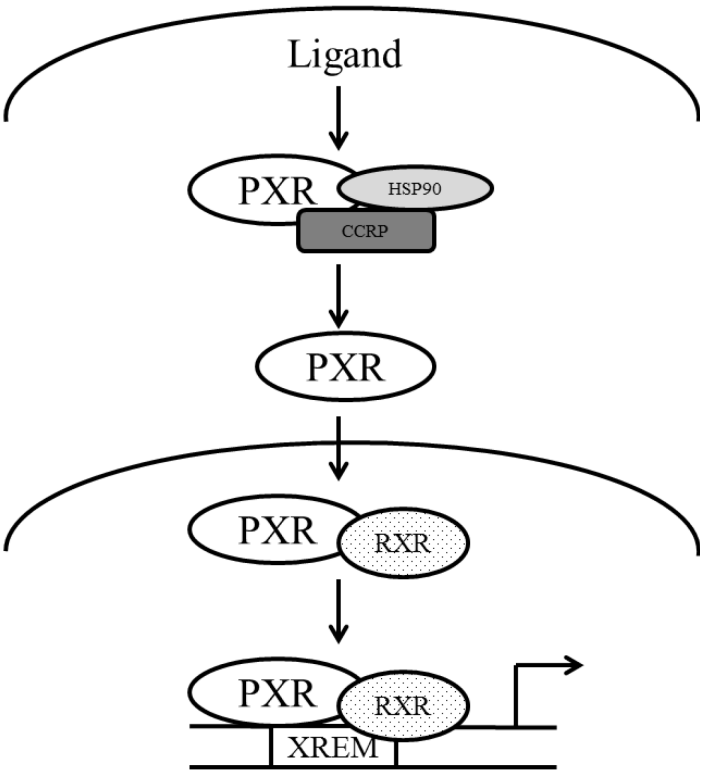

Figure 6. Ligand-dependent activation of the pregnane X receptor. PXR is sequestered in the cytosol by cytoplasmic CAR retention protein (CCRP) and heat shock protein 90 (HSP90). Upon ligand binding, PXR dissociates and translocates to the nucleus where it can then heterodimerize with RXR and bind to xenobiotic response elements (XREM) in the promoter regions of target genes to facilitate transcription. (Schematic adapted from Y. Timsit et al., CAR and PXR, the Xenobiotic-sensing receptors (95).)

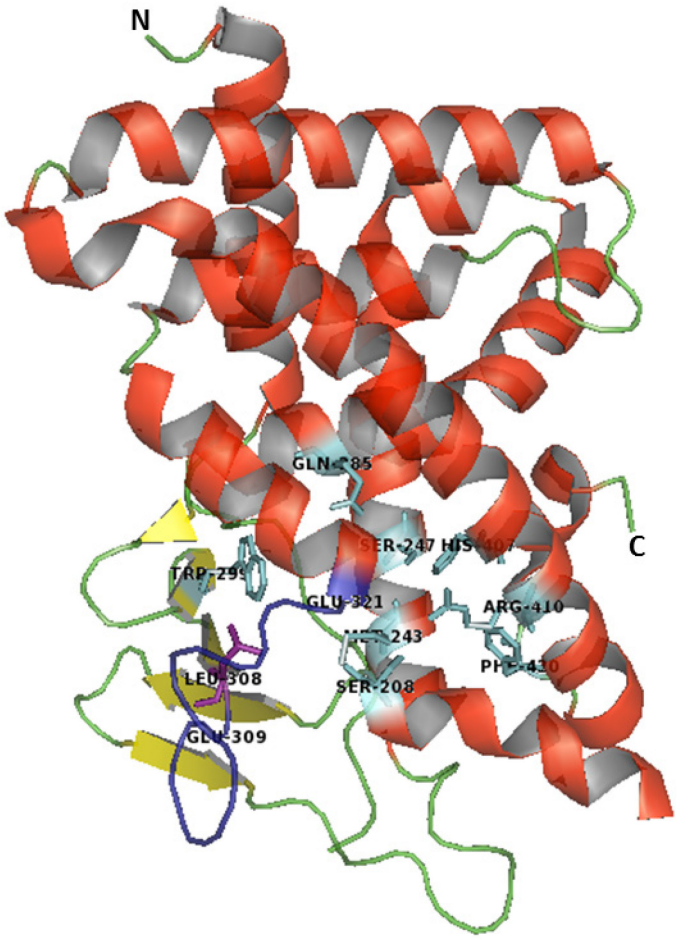

Figure 7. Crystal structure of human pregnane X receptor ligand-binding domain. Three-dimensional structure of the apo form of hPXR-LBD (PDB ID 1ILG). A flexible loop (dark blue, residues Glu309 to Glu321) is well-conserved across species and allows for expansion of the hydrophobic pocket to accommodate a variety of ligands. The polar residues, Met243, Ser247, Gln285, Trp299, His407, Phe420, Ser208 and Arg410 (shown in light blue), line the ligand-binding cavity and commonly form stabilizing electrostatic interactions with ligands. A single residue Leu308 (shown in purple) adjacent to the flexible loop has been observed to confer hPXR ligand specificity. Crystal structure was visualized and annotated using PyMol.

References

1. Kolata G. FDA approves AZT. Science. 1987;235(4796):1570.

2. Lau AJ, Yang G, Rajaraman G, Baucom CC, Chang TK. Species-dependent and receptor-selective action of bilobalide on the function of constitutive androstane receptor and pregnane X receptor. Drug Metab Dispos. 2012;40(1):178-86.

3. Kleywegt GJ, Jones TA. Detecting folding motifs and similarities in protein structures. Methods Enzymol. 1997;277:525-45.

4. Arts EJ, Hazuda DJ. HIV-1 antiretroviral drug therapy. Cold Spring Harb Perspect Med. 2012;2(4):a007161. PMCID: 3312400.

5. Furman PA, Fyfe JA, St Clair MH, Weinhold K, Rideout JL, Freeman GA, et al. Phosphorylation of 3'-azido-3'-deoxythymidine and selective interaction of the 5'-triphosphate with human immunodeficiency virus reverse transcriptase. Proc Natl Acad Sci U S A. 1986;83(21):8333-7. PMCID: 386922.

6. Eron JJ, Benoit SL, Jemsek J, MacArthur RD, Santana J, Quinn JB, et al. Treatment with lamivudine, zidovudine, or both in HIV-positive patients with 200 to 500 CD4+ cells per cubic millimeter. North American HIV Working Party. N Engl J Med. 1995;333(25):1662-9.

7. Dallakyan S, Olson AJ. Small-molecule library screening by docking with PyRx. Methods Mol Biol. 2015;1263:243-50.

8. Huey R, Morris GM, Olson AJ, Goodsell DS. A semiempirical free energy force field with charge-based desolvation. J Comput Chem. 2007;28(6):1145-52.

9. Ostberg T, Bertilsson G, Jendeberg L, Berkenstam A, Uppenberg J. Identification of residues in the PXR ligand binding domain critical for species specific and constitutive activation. Eur J Biochem. 2002;269(19):4896-904.

10. Carey D, Puls R, Amin J, Losso M, Phanupak P, Foulkes S, et al. Efficacy and safety of efavirenz 400 mg daily versus 600 mg daily: 96-week data from the randomised, double-blind, placebo-controlled, non-inferiority ENCORE1 study. Lancet Infect Dis. 2015;15(7):793-802.

11. Janssen PA, Lewi PJ, Arnold E, Daeyaert F, de Jonge M, Heeres J, et al. In search of a novel anti-HIV drug: multidisciplinary coordination in the discovery of 4-[[4-[[4-[(1E)-2-cyanoethenyl]-2,6-dimethylphenyl]amino]-2- pyrimidinyl]amino]benzonitrile (R278474, rilpivirine). J Med Chem. 2005;48(6):1901-9.

12. Pozniak AL, Morales-Ramirez J, Katabira E, Steyn D, Lupo SH, Santoscoy M, et al. Efficacy and safety of TMC278 in antiretroviral-naive HIV-1 patients: week 96 results of a phase IIb randomized trial. AIDS. 2010;24(1):55-65.

13. Baert L, van 't Klooster G, Dries W, Francois M, Wouters A, Basstanie E, et al. Development of a long-acting injectable formulation with nanoparticles of rilpivirine (TMC278) for HIV treatment. Eur J Pharm Biopharm. 2009;72(3):502-8.

14. WHO Expands Recommendation on Oral Preexposure Prophylaxis of HIV Infection (PrEP) World Health Organization; [November 2015; cited]; Available from: http://apps.who.int/iris/bitstream/10665/197906/1/WHO_HIV_2015.48_eng.pdf?ua=1.

15. Cundy KC, Sueoka C, Lynch GR, Griffin L, Lee WA, Shaw JP. Pharmacokinetics and bioavailability of the anti-human immunodeficiency virus nucleotide analog 9-[(R)-

2-(phosphonomethoxy)propyl]adenine (PMPA) in dogs. Antimicrob Agents Chemother. 1998;42(3):687-90. PMCID: 105518.

16. Robbins BL, Tran TT, Pinkerton FH, Jr., Akeb F, Guedj R, Grassi J, et al. Development of a new cartridge radioimmunoassay for determination of intracellular levels of lamivudine triphosphate in the peripheral blood mononuclear cells of human immunodeficiency virus-infected patients. Antimicrob Agents Chemother. 1998;42(10):2656-60. PMCID: 105914.

17. Package Insert: Highlights of Prescribing Information for Viread (Tenofovir Disoproxil Fumarate). Foster City, CA: Gilead Sciences.

18. Hawkins T, Veikley W, St Claire RL, 3rd, Guyer B, Clark N, Kearney BP. Intracellular pharmacokinetics of tenofovir diphosphate, carbovir triphosphate, and lamivudine triphosphate in patients receiving triple-nucleoside regimens. J Acquir Immune Defic Syndr. 2005;39(4):406-11.

19. Abdool Karim Q, Abdool Karim SS, Frohlich JA, Grobler AC, Baxter C, Mansoor LE, et al. Effectiveness and safety of tenofovir gel, an antiretroviral microbicide, for the prevention of HIV infection in women. Science. 2010;329(5996):1168-74. PMCID: 3001187.

20. Grant RM, Lama JR, Anderson PL, McMahan V, Liu AY, Vargas L, et al. Preexposure chemoprophylaxis for HIV prevention in men who have sex with men. N Engl J Med. 2010;363(27):2587-99. PMCID: 3079639.

21. Baeten JM, Donnell D, Ndase P, Mugo NR, Campbell JD, Wangisi J, et al. Antiretroviral prophylaxis for HIV prevention in heterosexual men and women. N Engl J Med. 2012;367(5):399-410. PMCID: 3770474.

22. U. S. Food and Drug Administration Approves Gilead's Truvada for Reducing the Risk of Acquiring HIV. Foster, CA: Gilead Sciences, Inc.; [July 2012; cited]; Available from: http://www.gilead.com/news/press-releases/2012/7/us-food-and-drug-administration-approves-gileads-truvada-for-reducing-the-risk-of-acquiring-hiv.

23. Ongoing and Planned PrEP Demonstration and Implementation Studies. AIDS Vaccine Advocacy Coalition - Global Advocacy for HIV Prevention; [June 2016; cited]; Available from: http://www.avac.org/sites/default/files/resource-files/PrEP_Trials_Demonstration_Projects_June_2016.pdf.

24. Gilman AG, Rall, T. W., Nies, A. S., Taylor, P., editor. Goodman and Gilman's: The Pharmacological Basis of Therapuetics. 8 ed: Pergamon Press; 1990.

25. Lee SS, Buters JT, Pineau T, Fernandez-Salguero P, Gonzalez FJ. Role of CYP2E1 in the hepatotoxicity of acetaminophen. J Biol Chem. 1996;271(20):12063-7.

26. Iyer KR, Sinz MW. Characterization of Phase I and Phase II hepatic drug metabolism activities in a panel of human liver preparations. Chem Biol Interact. 1999;118(2):151-69.

27. Yanakakis LJ, Bumpus NN. Biotransformation of the antiretroviral drug etravirine: metabolite identification, reaction phenotyping, and characterization of autoinduction of cytochrome P450-dependent metabolism. Drug Metab Dispos. 2012;40(4):803-14. PMCID: 3310427.

28. Lu Y, Hendrix CW, Bumpus NN. Cytochrome P450 3A5 plays a prominent role in the oxidative metabolism of the anti-human immunodeficiency virus drug maraviroc. Drug Metab Dispos. 2012;40(12):2221-30. PMCID: 3500548.

29. Avery LB, VanAusdall JL, Hendrix CW, Bumpus NN. Compartmentalization and antiviral effect of efavirenz metabolites in blood plasma, seminal plasma, and cerebrospinal fluid. Drug Metab Dispos. 2013;41(2):422-9. PMCID: 3558859.

30. Lade JM, Avery LB, Bumpus NN. Human biotransformation of the nonnucleoside reverse transcriptase inhibitor rilpivirine and a cross-species metabolism comparison. Antimicrob Agents Chemother. 2013;57(10):5067-79. PMCID: 3811466.

31. To EE, Hendrix CW, Bumpus NN. Dissimilarities in the metabolism of antiretroviral drugs used in HIV pre-exposure prophylaxis in colon and vagina tissues. Biochem Pharmacol. 2013;86(7):979-90. PMCID: 3807636.

32. Evans WE, Relling MV. Pharmacogenomics: translating functional genomics into rational therapeutics. Science. 1999;286(5439):487-91.

33. Jancova P, Anzenbacher P, Anzenbacherova E. Phase II drug metabolizing enzymes. Biomed Pap Med Fac Univ Palacky Olomouc Czech Repub. 2010;154(2):103-16.

34. Klingenberg M. Pigments of rat liver microsomes. Arch Biochem Biophys. 1958;75(2):376-86.

35. Omura T, Sato R. A new cytochrome in liver microsomes. J Biol Chem. 1962;237:1375-6.

36. Estabrook RW, Cooper DY, Rosenthal O. The Light Reversible Carbon Monoxide Inhibition of the Steroid C21-Hydroxylase System of the Adrenal Cortex. Biochem Z. 1963;338:741-55.

37. Cooper DY, Levin S, Narasimhulu S, Rosenthal O. Photochemical Action Spectrum of the Terminal Oxidase of Mixed Function Oxidase Systems. Science. 1965;147(3656):400-2.

38. Nelson DR, Koymans L, Kamataki T, Stegeman JJ, Feyereisen R, Waxman DJ, et al. P450 superfamily: update on new sequences, gene mapping, accession numbers and nomenclature. Pharmacogenetics. 1996;6(1):1-42.

39. Nebert DW, Wikvall K, Miller WL. Human cytochromes P450 in health and disease. Philos Trans R Soc Lond B Biol Sci. 2013;368(1612):20120431. PMCID: 3538421.

40. Guengerich FP, Waterman MR, Egli M. Recent Structural Insights into Cytochrome P450 Function. Trends Pharmacol Sci. 2016;37(8):625-40. PMCID: 4961565.

41. Koch I, Weil R, Wolbold R, Brockmoller J, Hustert E, Burk O, et al. Interindividual variability and tissue-specificity in the expression of cytochrome P450 3A mRNA. Drug Metab Dispos. 2002;30(10):1108-14.

42. Sakaguchi M, Mihara K, Sato R. A short amino-terminal segment of microsomal cytochrome P-450 functions both as an insertion signal and as a stop-transfer sequence. EMBO J. 1987;6(8):2425-31. PMCID: 553649.

43. Omura T, Ito A. Biosynthesis and intracellular sorting of mitochondrial forms of cytochrome P450. Methods Enzymol. 1991;206:75-81.

44. Poulos TL, Finzel BC, Howard AJ. High-resolution crystal structure of cytochrome P450cam. J Mol Biol. 1987;195(3):687-700.

45. Guengerich FP. Common and uncommon cytochrome P450 reactions related to metabolism and chemical toxicity. Chem Res Toxicol. 2001;14(6):611-50.

46. Cook DJ, Finnigan JD, Cook K, Black GW, Charnock SJ. Cytochromes P450: History, Classes, Catalytic Mechanism, and Industrial Application. Adv Protein Chem Struct Biol. 2016;105:105-26.

47. Porubsky PR, Meneely KM, Scott EE. Structures of human cytochrome P-450 2E1. Insights into the binding of inhibitors and both small molecular weight and fatty acid substrates. J Biol Chem. 2008;283(48):33698-707. PMCID: 2586265.

48. Yano JK, Wester MR, Schoch GA, Griffin KJ, Stout CD, Johnson EF. The structure of human microsomal cytochrome P450 3A4 determined by X-ray crystallography to 2.05-A resolution. J Biol Chem. 2004;279(37):38091-4.

49. Achour B, Barber J, Rostami-Hodjegan A. Expression of hepatic drug-metabolizing cytochrome p450 enzymes and their intercorrelations: a meta-analysis. Drug Metab Dispos. 2014;42(8):1349-56.

50. Drahushuk AT, McGarrigle BP, Larsen KE, Stegeman JJ, Olson JR. Detection of CYP1A1 protein in human liver and induction by TCDD in precision-cut liver slices incubated in dynamic organ culture. Carcinogenesis. 1998;19(8):1361-8.

51. Zanger UM, Schwab M. Cytochrome P450 enzymes in drug metabolism: regulation of gene expression, enzyme activities, and impact of genetic variation. Pharmacol Ther. 2013;138(1):103-41.

52. Rendic S, Guengerich FP. Survey of Human Oxidoreductases and Cytochrome P450 Enzymes Involved in the Metabolism of Xenobiotic and Natural Chemicals. Chem Res Toxicol. 2015;28(1):38-42. PMCID: 4303333.

53. Nebert DW. Polymorphisms in drug-metabolizing enzymes: what is their clinical relevance and why do they exist? Am J Hum Genet. 1997;60(2):265-71. PMCID: 1712416.

54. Lu Y, Fuchs EJ, Hendrix CW, Bumpus NN. CYP3A5 genotype impacts maraviroc concentrations in healthy volunteers. Drug Metab Dispos. 2014;42(11):1796-802. PMCID: 4201129.

55. Cohen M. The diagnosis and management of jaundice. Can Med Assoc J. 1963;88:319-23. PMCID: 1921047.

56. Miners JO, Mackenzie PI. Drug glucuronidation in humans. Pharmacol Ther. 1991;51(3):347-69.

57. Mackenzie PI, Owens IS, Burchell B, Bock KW, Bairoch A, Belanger A, et al. The UDP glycosyltransferase gene superfamily: recommended nomenclature update based on evolutionary divergence. Pharmacogenetics. 1997;7(4):255-69.

58. Bock KW. The UDP-glycosyltransferase (UGT) superfamily expressed in humans, insects and plants: Animal-plant arms-race and co-evolution. Biochem Pharmacol. 2016;99:11-7.

59. Mackenzie PI, Bock KW, Burchell B, Guillemette C, Ikushiro S, Iyanagi T, et al. Nomenclature update for the mammalian UDP glycosyltransferase (UGT) gene superfamily. Pharmacogenet Genomics. 2005;15(10):677-85.

60. Burchell B, Coughtrie MW. UDP-glucuronosyltransferases. Pharmacol Ther. 1989;43(2):261-89.

61. Tukey RH, Strassburg CP. Human UDP-glucuronosyltransferases: metabolism, expression, and disease. Annu Rev Pharmacol Toxicol. 2000;40:581-616.

62. Guillemette C. Pharmacogenomics of human UDP-glucuronosyltransferase enzymes. Pharmacogenomics J. 2003;3(3):136-58.

63. Radominska-Pandya A, Czernik PJ, Little JM, Battaglia E, Mackenzie PI. Structural and functional studies of UDP-glucuronosyltransferases. Drug Metab Rev. 1999;31(4):817-99.

64. Dutton GJ. Commentary: Control of UDP-glucuronyltransferase activity. Biochem Pharmacol. 1975;24(20):1835-41.

65. Hanninen O, Alanen K. The competitive inhibition of p-nitrophenyl-beta-D-glucopyranosiduronic acid synthesis by aliphatic alcohols in vitro. Biochem Pharmacol. 1966;15(10):1465-7.

66. Paul H, Illing A. Lipophilicity of acceptor substrate as a factor in "late foetal" rat liver microsomal UDP-glucuronosyltransferase activity. Biochem Pharmacol. 1980;29(7):999-1006.

67. Mackenzie PI, Owens IS. Cleavage of nascent UDP glucuronosyltransferase from rat liver by dog pancreatic microsomes. Biochem Biophys Res Commun. 1984;122(3):1441-9.

68. Mackenzie PI. Rat liver UDP-glucuronosyltransferase. Sequence and expression of a cDNA encoding a phenobarbital-inducible form. J Biol Chem. 1986;261(13):6119-25.

69. Mackenzie PI. Rat liver UDP-glucuronosyltransferase. Identification of cDNAs encoding two enzymes which glucuronidate testosterone, dihydrotestosterone, and beta-estradiol. J Biol Chem. 1987;262(20):9744-9.

70. Miley MJ, Zielinska AK, Keenan JE, Bratton SM, Radominska-Pandya A, Redinbo MR. Crystal structure of the cofactor-binding domain of the human phase II drug-metabolism enzyme UDP-glucuronosyltransferase 2B7. J Mol Biol. 2007;369(2):498-511. PMCID: 1976284.

71. Rowland A, Miners JO, Mackenzie PI. The UDP-glucuronosyltransferases: their role in drug metabolism and detoxification. Int J Biochem Cell Biol. 2013;45(6):1121-32.

72. Hauser SC, Ziurys JC, Gollan JL. A membrane transporter mediates access of uridine 5'-diphosphoglucuronic acid from the cytosol into the endoplasmic reticulum of rat hepatocytes: implications for glucuronidation reactions. Biochim Biophys Acta. 1988;967(2):149-57.

73. Bossuyt X, Blanckaert N. Carrier-mediated transport of intact UDP-glucuronic acid into the lumen of endoplasmic-reticulum-derived vesicles from rat liver. Biochem J. 1994;302 (Pt 1):261-9. PMCID: 1137218.

74. Berg CL, Radominska A, Lester R, Gollan JL. Membrane translocation and regulation of uridine diphosphate-glucuronic acid uptake in rat liver microsomal vesicles. Gastroenterology. 1995;108(1):183-92.

75. Rowland A, Mackenzie PI, Miners JO. Transporter-mediated uptake of UDP-glucuronic acid by human liver microsomes: assay conditions, kinetics, and inhibition. Drug Metab Dispos. 2015;43(1):147-53.

76. Banhegyi G, Braun L, Marcolongo P, Csala M, Fulceri R, Mandl J, et al. Evidence for an UDP-glucuronic acid/phenol glucuronide antiport in rat liver microsomal vesicles. Biochem J. 1996;315 (Pt 1):171-6. PMCID: 1217167.

77. de Wildt SN, Kearns GL, Leeder JS, van den Anker JN. Glucuronidation in humans. Pharmacogenetic and developmental aspects. Clin Pharmacokinet. 1999;36(6):439-52.

78. Bosma PJ, Chowdhury JR, Bakker C, Gantla S, de Boer A, Oostra BA, et al. The genetic basis of the reduced expression of bilirubin UDP-glucuronosyltransferase 1 in Gilbert's syndrome. N Engl J Med. 1995;333(18):1171-5.

79. Bosma PJ, Seppen J, Goldhoorn B, Bakker C, Oude Elferink RP, Chowdhury JR, et al. Bilirubin UDP-glucuronosyltransferase 1 is the only relevant bilirubin glucuronidating isoform in man. J Biol Chem. 1994;269(27):17960-4.

80. Iyer L, King CD, Whitington PF, Green MD, Roy SK, Tephly TR, et al. Genetic predisposition to the metabolism of irinotecan (CPT-11). Role of uridine diphosphate glucuronosyltransferase isoform 1A1 in the glucuronidation of its active metabolite (SN-38) in human liver microsomes. J Clin Invest. 1998;101(4):847-54. PMCID: 508633.

81. Selye H. Hormones and resistance. J Pharm Sci. 1971;60(1):1-28.

82. Schuetz EG, Wrighton SA, Barwick JL, Guzelian PS. Induction of cytochrome P-450 by glucocorticoids in rat liver. I. Evidence that glucocorticoids and pregnenolone 16 alpha-carbonitrile regulate de novo synthesis of a common form of cytochrome P-450 in cultures of adult rat hepatocytes and in the liver in vivo. J Biol Chem. 1984;259(3):1999-2006.

83. Gonzalez FJ, Song BJ, Hardwick JP. Pregnenolone 16 alpha-carbonitrile-inducible P-450 gene family: gene conversion and differential regulation. Mol Cell Biol. 1986;6(8):2969-76. PMCID: 367867.

84. Watkins JB, Klaassen CD. Induction of UDP-glucuronosyltransferase activities in Gunn, heterozygous, and Wistar rat livers by pregnenolone-16 alpha-carbonitrile. Drug Metab Dispos. 1982;10(6):590-4.

85. Schuetz EG, Guzelian PS. Induction of cytochrome P-450 by glucocorticoids in rat liver. II. Evidence that glucocorticoids regulate induction of cytochrome P-450 by a nonclassical receptor mechanism. J Biol Chem. 1984;259(3):2007-12.

86. Kliewer SA, Moore JT, Wade L, Staudinger JL, Watson MA, Jones SA, et al. An orphan nuclear receptor activated by pregnanes defines a novel steroid signaling pathway. Cell. 1998;92(1):73-82.

87. Germain P, Staels B, Dacquet C, Spedding M, Laudet V. Overview of nomenclature of nuclear receptors. Pharmacol Rev. 2006;58(4):685-704.

88. Aranda A, Pascual A. Nuclear hormone receptors and gene expression. Physiol Rev. 2001;81(3):1269-304.

89. A unified nomenclature system for the nuclear receptor superfamily. Cell. 1999;97(2):161-3.

90. Lehmann JM, McKee DD, Watson MA, Willson TM, Moore JT, Kliewer SA. The human orphan nuclear receptor PXR is activated by compounds that regulate CYP3A4 gene expression and cause drug interactions. J Clin Invest. 1998;102(5):1016-23. PMCID: 508967.

91. Blumberg B, Sabbagh W, Jr., Juguilon H, Bolado J, Jr., van Meter CM, Ong ES, et al. SXR, a novel steroid and xenobiotic-sensing nuclear receptor. Genes Dev. 1998;12(20):3195-205. PMCID: 317212.

92. Jones SA, Moore LB, Shenk JL, Wisely GB, Hamilton GA, McKee DD, et al. The pregnane X receptor: a promiscuous xenobiotic receptor that has diverged during evolution. Mol Endocrinol. 2000;14(1):27-39.

93. Squires EJ, Sueyoshi T, Negishi M. Cytoplasmic localization of pregnane X receptor and ligand-dependent nuclear translocation in mouse liver. J Biol Chem. 2004;279(47):49307-14.

94. Kawana K, Ikuta T, Kobayashi Y, Gotoh O, Takeda K, Kawajiri K. Molecular mechanism of nuclear translocation of an orphan nuclear receptor, SXR. Mol Pharmacol. 2003;63(3):524-31.

95. Timsit YE, Negishi M. CAR and PXR: the xenobiotic-sensing receptors. Steroids. 2007;72(3):231-46. PMCID: 1950246.

96. Moore JT, Kliewer SA. Use of the nuclear receptor PXR to predict drug interactions. Toxicology. 2000;153(1-3):1-10.

97. Sueyoshi T, Negishi M. Phenobarbital response elements of cytochrome P450 genes and nuclear receptors. Annu Rev Pharmacol Toxicol. 2001;41:123-43.

98. Moore LB, Maglich JM, McKee DD, Wisely B, Willson TM, Kliewer SA, et al. Pregnane X receptor (PXR), constitutive androstane receptor (CAR), and benzoate X receptor (BXR) define three pharmacologically distinct classes of nuclear receptors. Mol Endocrinol. 2002;16(5):977-86.

99. Hariparsad N, Chu X, Yabut J, Labhart P, Hartley DP, Dai X, et al. Identification of pregnane-X receptor target genes and coactivator and corepressor binding to promoter elements in human hepatocytes. Nucleic Acids Res. 2009;37(4):1160-73. PMCID: 2651806.

100. Kojima K, Nagata K, Matsubara T, Yamazoe Y. Broad but distinct role of pregnane x receptor on the expression of individual cytochrome p450s in human hepatocytes. Drug Metab Pharmacokinet. 2007;22(4):276-86.

101. Xu C, Wang X, Staudinger JL. Regulation of tissue-specific carboxylesterase expression by pregnane x receptor and constitutive androstane receptor. Drug Metab Dispos. 2009;37(7):1539-47. PMCID: 2698945.

102. Shang W, Liu J, Chen R, Ning R, Xiong J, Liu W, et al. Fluoxetine reduces CES1, CES2, and CYP3A4 expression through decreasing PXR and increasing DEC1 in HepG2 cells. Xenobiotica. 2016;46(5):393-405.

103. Vyhlidal CA, Rogan PK, Leeder JS. Development and refinement of pregnane X receptor (PXR) DNA binding site model using information theory: insights into PXR-mediated gene regulation. J Biol Chem. 2004;279(45):46779-86.

104. Watkins RE, Wisely GB, Moore LB, Collins JL, Lambert MH, Williams SP, et al. The human nuclear xenobiotic receptor PXR: structural determinants of directed promiscuity. Science. 2001;292(5525):2329-33.

105. Tirona RG, Leake BF, Podust LM, Kim RB. Identification of amino acids in rat pregnane X receptor that determine species-specific activation. Mol Pharmacol. 2004;65(1):36-44.

106. Onate SA, Tsai SY, Tsai MJ, O'Malley BW. Sequence and characterization of a coactivator for the steroid hormone receptor superfamily. Science. 1995;270(5240):1354-7.

107. Onate SA, Boonyaratanakornkit V, Spencer TE, Tsai SY, Tsai MJ, Edwards DP, et al. The steroid receptor coactivator-1 contains multiple receptor interacting and

activation domains that cooperatively enhance the activation function 1 (AF1) and AF2 domains of steroid receptors. J Biol Chem. 1998;273(20):12101-8.

108. Watkins RE, Davis-Searles PR, Lambert MH, Redinbo MR. Coactivator binding promotes the specific interaction between ligand and the pregnane X receptor. J Mol Biol. 2003;331(4):815-28.

Chapter 2: Human Biotransformation of the Non-nucleoside Reverse Transcriptase Inhibitor Rilpivirine and a Cross Species Metabolism Comparison

Abstract

Rilpivirine is a non-nucleoside reverse transcriptase inhibitor used to treat HIV-1. In the present study, the pathways responsible for the biotransformation of rilpivirine were defined. Using human liver microsomes, the formation of two mono- and two di-oxygenated metabolites were detected via ultra high-performance liquid chromatography-tandem mass spectrometry (UHPLC-MS/MS). Mass spectral analysis of the products suggested that these metabolites resulted from oxygenation of the 2,6-dimethylphenyl ring and methyl groups of rilpivirine. Chemical inhibition studies and cDNA-expressed cytochromes P450 (CYP) assays indicated that oxygenations were catalyzed primarily by CYP3A4 and CYP3A5. Glucuronide conjugates of rilpivirine and a monomethylhydroxylated metabolite of rilpivirine were also detected and were found to be formed by UDP-glucuronosyltransferases (UGTs), UGT1A4 and UGT1A1, respectively. All metabolites that were identified *in vitro* were detectable *in vivo*. Further, targeted UHPLC-MS/MS-based *in vivo* metabolomics screening revealed that rilpivirine treatment versus efavirenz treatment may result in differential levels of endogenous metabolites, including tyrosine, homocysteine and adenosine. Rilpivirine biotransformation was also assessed across species using liver microsomes isolated from a range of mammals, and the metabolite profile identified using human liver microsomes was largely conserved for both oxidative and glucuronide metabolite formation. These

studies provide novel insight into the metabolism of rilpivirine and the potential differential effects of rilpivirine- and efavirenz-containing antiretroviral regimens on the endogenous metabolome.

Introduction

Rilpivirine (RPV; Edurant^{TM}), 4-[[4-[[4-[(1E)-2-cyanoethenyl]-2,6-dimethylphenyl]amino]-2-pyrimidinyl]amino]benzonitrile, is a more recently developed non-nucleoside reverse transcriptase inhibitor that has been FDA approved for oral administration in combination therapy for the treatment of drug-naïve individuals infected with the human immunodeficiency virus (HIV)-1 (1). RPV is a cyanovinyl diarylpyrimidine and as such has inherent molecular flexibility, allowing for multiple modes of allosteric binding within the hydrophobic binding pocket of the HIV reverse transcriptase; therefore, RPV has a higher genetic barrier to resistance than the initially developed non-nucleoside reverse transcriptase inhibitors, efavirenz and nevirapine (2, 3). In addition, because of its antiviral efficacy, RPV is being developed as an injectable, long-acting formulation for potential use in HIV pre-exposure prophylaxis (4, 5). ECHO and THRIVE clinical trials, comparing RPV-tenofovir-emtricitabine (Complera^{TM}) treatment to that of efavirenz-tenofovir-emtricitabine (Atripla^{TM}), demonstrated that the RPV co-formulation has more potent antiviral activity and fewer adverse side effects relative to a daily antiretroviral efavirenz-based regimen. In these studies, the most noted adverse events associated with the efavirenz-containing regimen were psychiatric symptoms and rash; however, the molecular mechanism(s) that underlie the differences in the safety profiles of RPV-containing versus efavirenz-containing regimens are unknown

(6, 7). While we recently demonstrated that the primary metabolite of efavirenz, 8-hydroxyefavirenz, may play a causal role in efavirenz-mediated toxicities, including hepatic and neuronal toxicity, this type of analysis is not yet possible for RPV as the metabolites of this drug have yet to be defined (8, 9).

The cytochromes P450 (CYP) superfamily of heme-containing monooxygenases play a major role in the metabolism of a variety of clinically relevant drugs including many antiretrovirals. The package inserts for Edurant™ and Complera™ state that RPV is primarily metabolized in the liver by CYP3A4 (10, 11); however, primary data detailing the identities of the RPV metabolites and the relative contributions of individual CYP isozymes to the formation of these metabolites have yet to be reported. In addition, a potential role for conjugative metabolism of RPV by phase II drug metabolizing enzymes including UDP-glucuronosyltransferases (UGTs) has yet to be demonstrated. Since RPV is taken in combination with other therapeutic agents, defining the routes of RPV metabolism should help to facilitate a more robust and reliable prediction of potential drug-drug interactions involving RPV. Further, elucidation of the pathways of RPV metabolism may lend mechanistic insight to the understanding of potential inter-individual differences in RPV exposure and clearance.

The objectives of this study were to: 1) comprehensively characterize the biotransformation of RPV *in vitro* through the utilization of human liver microsomes, cDNA-expressed CYP and UGT isozymes as well as primary human hepatocytes analyzed by ultra high-performance liquid chromatography-tandem mass spectrometry (UHPLC-MS/MS); 2) gain an understanding of the profiles of endogenous small

molecules that regulate key cellular processes in individuals receiving Complera™ versus Atripla™ in order to spur the elucidation of molecular mechanism(s) that may underlie the observed differences in the safety profiles of RPV and efavirenz clinically. Collectively, these data lend novel insight into the routes of RPV metabolism which we anticipate will help to facilitate the prediction of drug-drug interactions involving RPV. Further, these studies provide a foundation for a mechanistic understanding of the pathways that modulate RPV exposure *in vivo*.

Materials and Methods

Materials

Rilpivirine (RPV) was obtained through the National Institutes of Health AIDS Research and Reference Reagent Program (Germantown, MD). Dimethyl sulfoxide (DMSO) was used as the vehicle for all reagents and purchased from Mediatech Inc. (Manassas, VA). (+)-*N*-3-benzylnirvanol, furafylline, ketoconazole, sulfaphenazole and quinidine were purchased from Sigma-Aldrich, Co. (St. Louis, MO), and 2-phenyl-2-(1-piperidinyl)propane (PPP) from Santa Cruz Biotechnology Inc. (Santa Cruz, CA).

RPV metabolism by liver microsomes, cDNA-expressed CYPs and cDNA-expressed UGTs

RPV (20 μM) was incubated with the following liver microsomes (Xenotech LLC., Lenexa, KS) at a concentration of 2 mg/ml: human (mixed sex, pool of 50), beagle dog (male, pool of 8), Golden Syrian (GS) hamster (male, pool of 100), Hartley Albino (HA) guinea pig (male, pool of 50), Sinclair minipig (male, pool of 3), cynomolgus (CYN) monkey (male, pool of 10), rhesus monkey (male, pool of 6), BALB/c mouse

(male, pool of 800), CD1 mouse (male, pool of 1000), New Zealand (NZ) rabbit (male, pool of 8) and Sprague Dawley (SD) rat (male, pool of 433). For CYP and UGT individual contribution experiments, 20 μM RPV was incubated with the following cDNA-expressed enzymes (Supersomes^{TM}, BD Biosciences): CYP1A2, -2B6, -2C8, -2C9, -2C19, -2D6, -3A4, -3A5 and UGT1A1, -1A3, -1A4, -1A6, -1A7, -1A8, -1A9, -1A10, -2B4, -2B7, -2B15 and -2B17 at concentrations of 10 pmol/ml and 0.2 mg/ml, respectively.

Liver microsomes (2 mg/ml) were pre-incubated with RPV at 37°C for 5 min in 100 mM potassium phosphate buffer pH 7.4 prior to the addition of an NADPH-regenerating system (BD Biosciences). RPV incubations with human liver microsomes and different species liver microsomes proceeded at 37°C for a total of 30 min. Formation of glucuronidated metabolites in the liver microsome preparations required the simultaneous addition of NADPH and a UGT reaction mix (BD Biosciences), containing 25 mM uridine 5'-diphosphoglucuronic acid (UDPGA) and alamethicin, and reactions proceeded at 37°C for 60 min.

cDNA-expressed CYPs (10 pmol/ml) were pre-incubated with RPV at 37°C for 5 min in 100 mM potassium phosphate buffer pH 7.4 prior to the addition of an NADPH-regenerating system from which the reaction proceeded at 37°C for a total of 30 min. cDNA-expressed UGT assays, however, required a modified reaction preparation. RPV was pre-incubated for 30 min at 37°C in 100 mM potassium phosphate buffer pH 7.4 with 10 pmol/ml CYP3A4 and an NADPH-regenerating system in order to allow for hydroxylated metabolite formation, to which the UDPGA and alamethicin-containing

reaction mix was added. Glucuronide metabolite formation was then initiated by the addition of 0.2 mg/ml of each individual UGT isozyme and reactions proceeded at 37°C for an additional 60 min.

Chemical inhibition of CYPs was performed by pre-incubating 2 mg/ml human liver microsomes for 5 min in a reaction mixture containing a NADPH-regenerating system, 100 mM potassium phosphate buffer pH 7.4 and the following concentrations of inhibitor or vehicle: 20 µM furafylline (CYP1A2 inhibitor), 30 µM PPP (CYP2B6 inhibitor), 20 µM sulfaphenazole (CYP2C9 inhibitor), 10 µM (+)-*N*-3-benzylnirvanol (CYP2C19 inhibitor), 1 µM quinidine (CYP2D6 inhibitor), 1 µM ketoconazole (CYP3A4 and -3A5 inhibitor) and 0.2% DMSO. These final concentrations of reagents were based on previously reported studies (12-14). Following the 5 min pre-incubation at 37°C, RPV was added to each inhibitor or DMSO control treatment, and the reactions were allowed to proceed at 37°C for a total of 30 min.

The resulting 100 µl reaction volumes from the previously described metabolism assays were quenched with 100 µl of acetonitrile at the indicated times and incubated on ice for 10 min prior to centrifuging at 10,000 × *g* for 10 min at 4°C. Following centrifugation, supernatants of these assays were dried under vacuum before reconstituting in 100 µl of methanol, from which 1 µl was injected for UHPLC-MS/MS analysis.

UHPLC-MS/MS analysis of RPV oxygenated and glucuronide metabolites

A UHPLC-MS/MS method was developed and optimized for the detection of RPV metabolites using a Dionex UltiMate 3000 UHPLC system (Thermo Scientific,

Pittsburgh, PA) coupled to a Thermo Scientific TSQ Vantage Triple Stage Quadrupole mass spectrometer. Samples were resolved using a Polaris C18-A column (5 µm, 100 × 2.0 mm; Agilent Technologies, Santa Clara, CA) at a flow rate of 0.4 ml/min. A multi-step gradient was implemented using mobile phases A (water, 0.1% formic acid) and B (acetonitrile, 0.1% formic acid): 10% B for 0.0 to 1.0 min, increased from 10% B to 55 B% over 1.0 to 8.0 min, held at 100% B from 8.0 to 8.3 min and then decreased to 10% B for 8.3 to 10 min for column re-equilibration. The electrospray ionization interface was set to positive ion mode and the following instrument parameters were used: ion transfer capillary temperature, 300°C; spray voltage, 5500 V; sheath and auxillary nitrogen gas pressures, 60 and 15, respectively; collision energy, 30 V for RPV and oxygenated metabolites and 60 V for glucuronidated metabolites. Metabolite identification was initially performed in product ion (MS/MS) mode, and selected reaction monitoring (SRM) mode was used for the detection of the relative abundance levels of metabolites. Metabolites were identified as those ions with a signal-to-noise ratio of five or greater that exhibited NADPH- and/or UDPGA-dependence. The following transitions in SRM mode were monitored (parent mass, Q1→product ion, Q3): 367→195 *m/z* (RPV), 383→222 *m/z* (monohydroxylated RPV; M1 and M2), 399→183 *m/z* (dihydroxylated RPV; M3), 399→196 *m/z* (dihydroxylated RPV; M4), 543→367 *m/z* (RPV glucuronide conjugate; M5), 559→383 *m/z* (monohydroxylated RPV glucuronide conjugate; M6) and 575→399 *m/z* (dihydroxylated RPV glucuronide conjugate; M7). The approximate retention times for metabolites M1 through M7 were 5.51, 5.66, 5.78, 5.88, 5.74, 5.90, and 5.32 min, respectively, and 6.48 min for RPV.

RPV treatment of primary human hepatocytes

Six- and twelve-well plates of primary human hepatocytes with matrigel overlay were purchased from Xenotech, LLC. that had been isolated from three individual donors (Lots 1155, 1157 and 1158). Ages in years and sex of donors were as follows: 43 female, 59 female and 36 male. Cell viabilities were reported to be 74.7%, 77.9% and 74.9%, respectively. Hepatocytes were incubated overnight in Williams' Medium E (Invitrogen, Carlsbad, CA) supplemented with 10% fetal bovine serum, 1% penicillin-streptomycin and 1% L-glutamine at 37°C in a 5% CO_2 humidified environment. Prior to treatment, hepatocytes were placed into fresh medium to which either 0.1% DMSO vehicle or 10 μM RPV were added for 6, 12 and 24 h incubations. Medium from each DMSO and RPV time point was collected, dried under vacuum and reconstituted in 100 μl of methanol of which 1 μl was injected onto the UHPLC-MS/MS system for analysis.

Human plasma and urine sample preparation for UHPLC-MS/MS analysis

De-identified plasma and urine samples were obtained from participants (a total of six) already on an antiretroviral drug regimen and had been recruited by the Drug Development Unit of the Johns Hopkins University School of Medicine Division of Clinical Pharmacology after providing written informed consent for participation in a protocol approved by the institutional review board of the Johns Hopkins Medical Institutions. Blood and urine samples were obtained from three HIV-1 infected individuals receiving Complera™, a co-formulation of RPV-tenofovir-emtricitabine, and from three HIV-1 infected individuals receiving Atripla™, a co-formulation of efavirenz-tenofovir-emtricitabine. Ages in years and sex of participants being treated with

Complera™ were as follows: 29 male, 45 female and 42 male. Ages in years and sex of participants being treated with Atripla™ were as follows: 50 male, 58 female and 40 male. Whole blood was centrifuged for 10 min at 1,100 × *g* in EDTA-coated tubes, from which the resulting supernatant was collected as plasma and live virus was heat inactivated for 10 min at 60°C. Urine was centrifuged for 10 min at 12,000 × *g* and the resulting supernatant was collected. For UHPLC-MS/MS analysis, 100 µl of plasma or urine was extracted with 500 µl of acetonitrile, incubated on ice for 10 min, followed by centrifugation at 10,000 × *g* for 10 min. For RPV metabolite detection, Complera™ clinical samples were dried under vacuum and then six individual extracts of either plasma or urine were pooled and reconstituted in a total of 100 µl of methanol, of which 5 µl was injected on the UHPLC-MS/MS system for analysis.

UHPLC-MS/MS-based targeted screen of plasma and urine endogenous metabolomic profiles

Plasma and urine from the previously described Complera™ clinical samples were utilized in a targeted screen of endogenous small molecule metabolites. The metabolic profiles of these samples were further analyzed in comparison to plasma and urine of HIV-infected individuals receiving therapeutic treatment with Atripla™. Non-infected, antiretroviral untreated human plasma was prepared by the manufacturer using an EDTA anticoagulant (Lots BRH642964, BRH642965, BRH642967) as the experimental samples were and urine (Lots BRH720679, BRH720681, BRH720682) that was purchased from Bioreclamation, LLC (Westbury, NY) was processed in the same manner as the experimental samples. Separate positive ion and negative ion mode

UHPLC-MS/MS methods were developed and optimized for the detection of a range of metabolites using a Dionex UltiMate 3000 UHPLC system coupled to a Thermo Scientific TSQ Vantage Triple Stage Quadrupole mass spectrometer using the same instrument parameters as defined above. Samples were resolved using a Polaris C18-A column (5 µm, 100 × 2.0 mm; Agilent Technologies). The positive ion mode method used a multi-step gradient of mobile phases A (water, 0.5% acetic acid) and B (methanol, 0.5% acetic acid): 5% B for 0.0 to 1.1 min at 0.3 ml/min, increased from 5 to 95% B for 1.1 to 4.5 min at 0.3 ml/min, held at 95% B for 4.5 to 5.0 min at 0.4 ml/min, then 95% B for 5.0 to 5.1 min at 0.3 ml/min and the column was re-equilibrated with 5% B from 5.1 to 6 min at 0.3 ml/min. The negative ion mode method used a flow gradient at 0.35 ml/min of mobile phases A (water, 0.1% formic acid) and B (acetonitrile, 0.1% formic acid): 10% B for 0.0 to 0.9 min, increased from 10 to 90% B for 0.9 to 4.0 min and the column was re-equilibrated with 10% B for 4.0 to 5 min. Extracted plasma and urine samples as previously described were reconstituted in either 50 µl of mobile phase A (water, 0.1% formic acid) for analysis by positive ion mode or 50 µl of a 1:1 solution of mobile phase A to methanol for negative ion mode analysis, of which 5 µl was injected for both UHPLC-MS/MS analyses. SRM mode transitions were developed for the detection and determination of relative abundance levels of each endogenous metabolite via infusion of synthetic standards for each molecule. The optimized parent mass to product ion transitions and collision energies used for each metabolite in this targeted screen, as well as their approximate retention times, are listed in supplementary Tables 1 and 2 for detection in positive ion and negation ion mode, respectively.

Metabolite	$[M+H]^+$	Product Ion	CE (V)	RT (min)
Aspartate	134.0	88	13	1.15
Homocysteine	136.1	89.99	12	1.15
Lysine	146.85	84.05	15	0.85
Glutamic Acid	148.1	84.01	14	0.97
Methionine	149.97	45.02	54	1.10
Histidine	155.792	83.01	28	0.92
Phenylalanine	166.08	120.04	11	2.61
Arginine	175.1	60.01	14	0.93
Citrulline	176	113	16	0.93
Tyrosine	182.1	91.01	28	1.34
Tryptophan	205.07	146.01	21	3.81
Cytidine	244.1	112	31	1.00
Adenosine	268.1	136	18	2.03

Table 1. Endogenous metabolites detected by positive ionization. SRM transitions were developed for the detection of small molecules present in the plasma and urine of individuals receiving either Complera™ or Atripla™ antiretroviral therapy and for those present in the biological samples of non-infected, antiretroviral untreated individuals. The

above metabolites were detected by a positive ion mode UHPLC-MS/MS screen using the stated parent mass, $[M+H]^+$, to product ion transitions at the specified collision energies (CE) and resulted in the approximate retention times (RT).

Metabolite	$[M-H]^-$	Product Ion	CE (V)	RT (min)
Pyruvate	86.7	42.5	26	0.94
Succinc Acid	116.8	72.99	15	1.04
Malic Acid	132.8	71.2	20	0.86
Citrate	190.926	110.9	13	0.98
Thymidine	241.1	124.96	20	1.08
Uridine	242.9	109.96	20	0.99

Table 2. Endogenous metabolites detected by negative ionization. SRM transitions were developed for the detection of small molecules present in the plasma and urine of individuals receiving either Complera™ or Atripla™ antiretroviral therapy and for those present in the biological samples of non-infected, antiretroviral untreated individuals. The above metabolites were detected by a negative ion mode UHPLC-MS/MS screen using the stated parent mass, $[M-H]^-$, to product ion transitions at the specified collision energies (CE) and resulted in the approximate retention times (RT).

Statistical Analysis

Data analysis was performed using GraphPad Prism (version 6; GraphPad Software Inc., San Diego, CA). Statistical significance was determined by Student's *t* test: *, $p < 0.05$; **, $p < 0.01$; and ***, $p < 0.001$.

Results

In vitro detection of RPV oxygenated and glucuronide metabolites

RPV metabolites were initially characterized using a human liver microsome assay and analyzed by UHPLC-MS/MS. Tandem mass spectrometry was used for metabolite detection and provided structural information of metabolites based on the resulting fragment ions; however, SRM mode allowed for greater sensitivity in detecting metabolites and was, therefore, utilized in determining the relative abundance for all metabolites. Since the metabolites of RPV were previously unreported, synthetic standards of these compounds could not be obtained. Thus, the assays that were developed here for the purpose of metabolite identification are solely qualitative. A total of seven RPV metabolites were detected using the human liver microsome *in vitro* assay and have been denoted as metabolite 1 (M1) through metabolite 7 (M7). Two monohydroxylated metabolites, M1 and M2, (383 *m/z*) and two dihydroxylated metabolites, M3 and M4, (399 *m/z*) resulted from oxygen insertion into RPV (Figure 1). Three glucuronides resulted from direct glucuronidation of RPV (543 *m/z*) and glucuronidation of mono- and di-oxygenated RPV metabolites (559 *m/z* and 575 *m/z*, respectively) (Figure 2). Hydroxylated metabolites were monitored via SRM mode using the following transitions (parent mass, Q1→product ion, Q3): 383→222 *m/z* (M1 and

M2), 399→183 *m/z* (M3), 399→196 *m/z* (M4). From a 30 min human liver microsomal metabolism assay, M2 was observed to be more abundant than M1 by an approximate 13.0-fold, and M4 was more abundant than M3 by an approximate 2.3-fold. The following transitions were used for monitoring glucuronidated metabolites, 543→367 *m/z* (M5), 559→383 *m/z* (M6) and 575→399 *m/z* (M7). From a 60 min human liver microsomal metabolism assay in the presence of UDPGA, glucuronide M6 was observed to be approximately 1500.0-fold and 163.3-fold greater than the relative abundance of M5 and M7 glucuronides, respectively. Other phase II metabolites, such as sulfated metabolites, were not detected under these experimental conditions.

Chemical structures of these metabolites were proposed through use of individual fragmentation spectra observed in MS/MS mode. For monohydroxylated metabolite M1, it is proposed that fragment ions 179.42, 195.15, 206.37 and 221.82 *m/z* correspond to the loss of $C_9H_{14}N_4$, $C_9H_{14}N_4O$, $C_{10}H_{14}N_4O$ and $C_{11}H_{16}N_4O$, respectively. The observed fragment ions 192.48, 221.63 and 247.59 *m/z* for the more abundant monohydroxylated metabolite M2 are proposed to correspond to the loss of $C_9H_{12}N_4O$, $C_{11}H_{16}N_4O$, and $C_{13}H_{20}N_4O$, respectively (Figure 3). For dihydroxylated metabolite M3, the fragment ions 182.82, 209.23, 284.25 and 336.62 *m/z* are proposed to be consistent with the loss of $C_8H_{14}N_4O$, $C_{10}H_{16}N_4O$, $C_{16}H_{20}N_4O$ and $C_{19}H_{21}N_5O$, respectively (Figure 3). Dihydroxylated metabolite M4 fragment ions, 170.24, 194.60 and 234.79 *m/z* were predicted to result from the loss of $C_7H_{14}N_4O$, $C_9H_{14}N_4O$ and $C_{12}H_{18}N_4O$, respectively (Figure 3). The structures of glucuronidated metabolites were elucidated in a similar fashion and the resulting fragmentation spectra were compared to those observed for

RPV or for the predicted corresponding oxidative metabolite. Glucuronide M5 is proposed to result from direct *N*-linked glucuronidation of RPV on the pyrimidine ring as evidenced by the fact that human liver microsomes could form this metabolite in the absence of an NADPH-regenerating system (required for cytochrome P450-dependent activity). In addition, the mass-to-charge ratio of this metabolite as well as the fragmentation pattern was consistent with direct conjugation of glucuronic acid to RPV itself (Figure 4). The most abundant 167.81 *m/z* fragment ion of M5 was commensurate with the loss of $C_8H_{16}N_4$ and was also observed to be a predominant fragment ion for RPV (Figure 4). Comparison of the M6 fragmentation spectrum to that of the monohydroxymethyl metabolite M2 suggested *O*-linked glucuronidation occurring after initial oxidative metabolism with the fragment ion 382.62 *m/z* corresponding to loss of M2 itself, $C_{22}H_{18}N_6O$, and the fragment ion 220.06 *m/z* corresponding to the loss of $C_{11}H_{16}N_4O$ as was similarly observed for the fragmentation of M2 (Figure 4). Furthermore, comparison of the fragment ions of M7 to those of the dihydroxymethyl metabolite M4 also indicated *O*-linked glucuronidation after initial oxidative metabolism with the fragment ions 170.43, 195.36 and 235.10 *m/z* proposed to correlate to the loss of $C_7H_{14}N_4O$, $C_9H_{14}N_4O$ and $C_{12}H_{18}N_4O$, respectively, as was similarly observed for the fragmentation of M4 (Figure 4). From the predicted modes of fragmentation for these metabolites, we propose that M1 results from oxygen insertion on the 2,6-dimethylphenyl ring, M2 results from oxygen insertion on either methyl group, M3 results from oxygen insertion on a methyl group as well as the dimethylphenyl ring and M4 results from oxygen insertion on both methyl groups.

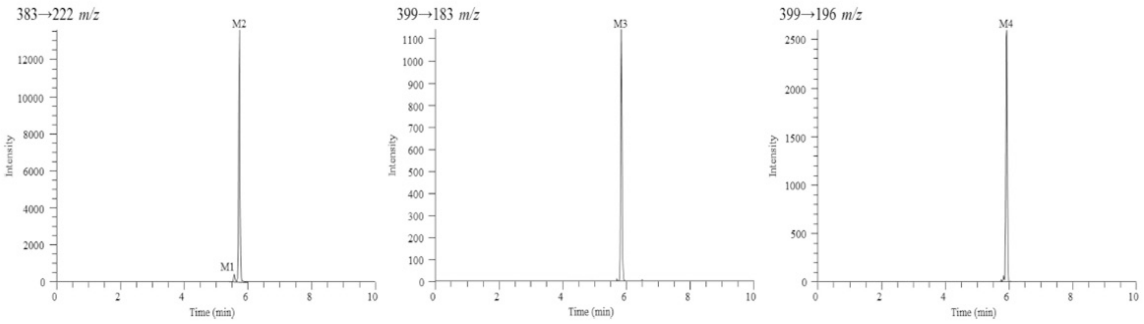

Figure 1. Extracted ion chromatograms for RPV monohydroxylated metabolites, M1 and M2, and dihydroxylated metabolites, M3 and M4. Human liver microsomes (2 mg/ml) were incubated with 20 μM RPV for 30 min at 37°C in the presence of an NADPH-regenerating system. RPV metabolites were detected by UHPLC-MS/MS in SRM mode using the following transitions: 383→222 *m/z* (M1 and M2), 399→183 *m/z* (M3) and 399→196 *m/z* (M4). Chromatograms are representative of three individual experiments. It should be noted that the y-axes differ for each metabolite due to the observed intensity of the ions.

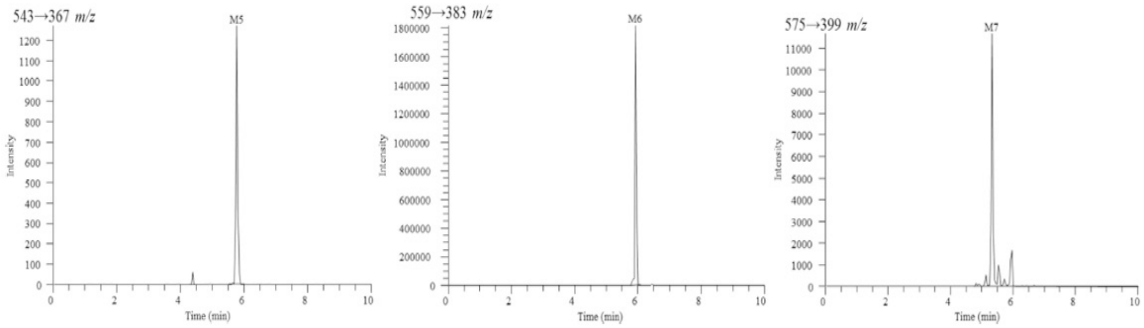

Figure 2. Extracted ion chromatograms for RPV glucuronidated metabolites, M5, M6 and M7. Peaks not indicated as metabolites in these chromatograms were also present in the minus-NADPH and UDPGA controls and resulted in intensities below a signal-to-noise ratio of five. Human liver microsomes (2 mg/ml) were incubated with 20 μM RPV for 60 min at 37°C in the presence of an NADPH-regenerating system and UDPGA. Metabolites were detected by UHPLC-MS/MS in SRM mode using the following transitions: 543→367 *m/z* (M5), 559→383 *m/z* (M6) and 575→399 *m/z* (M7). Chromatograms are representative of three individual experiments. It should be noted that the y-axes differ for each metabolite due to the observed intensity of the ions.

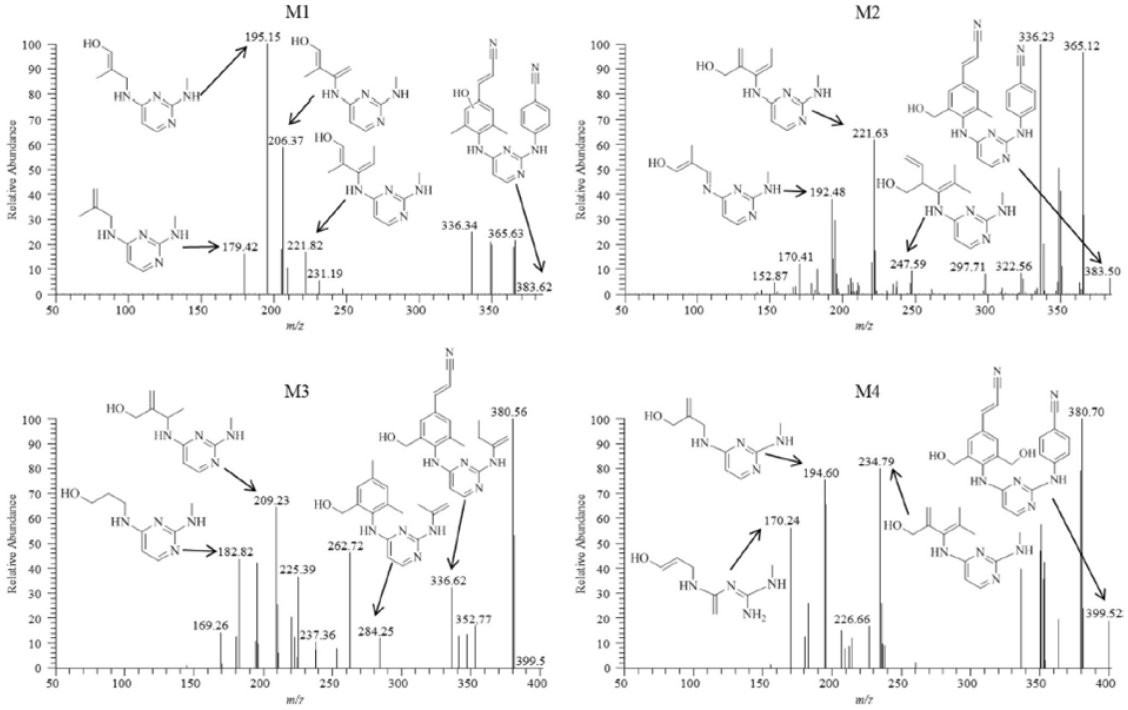

Figure 3. Fragmentation spectra of monohydryoxylated metabolites M1 and M2 (top) and dihydroxylated metabolites M3 and M4 (bottom). Proposed modes of fragmentation are indicated by the fragment ion corresponding to the appropriate mass-to-charge ratio. Human liver microsomes (2 mg/ml) were incubated with 20 μM RPV for 30 min at 37°C in the presence of an NADPH-regenerating system. Metabolites were detected in MS/MS mode using parent masses of 383 *m/z* for M1 and M2 and 399 *m/z* for M3 and M4. Spectra are representative of three individual experiments.

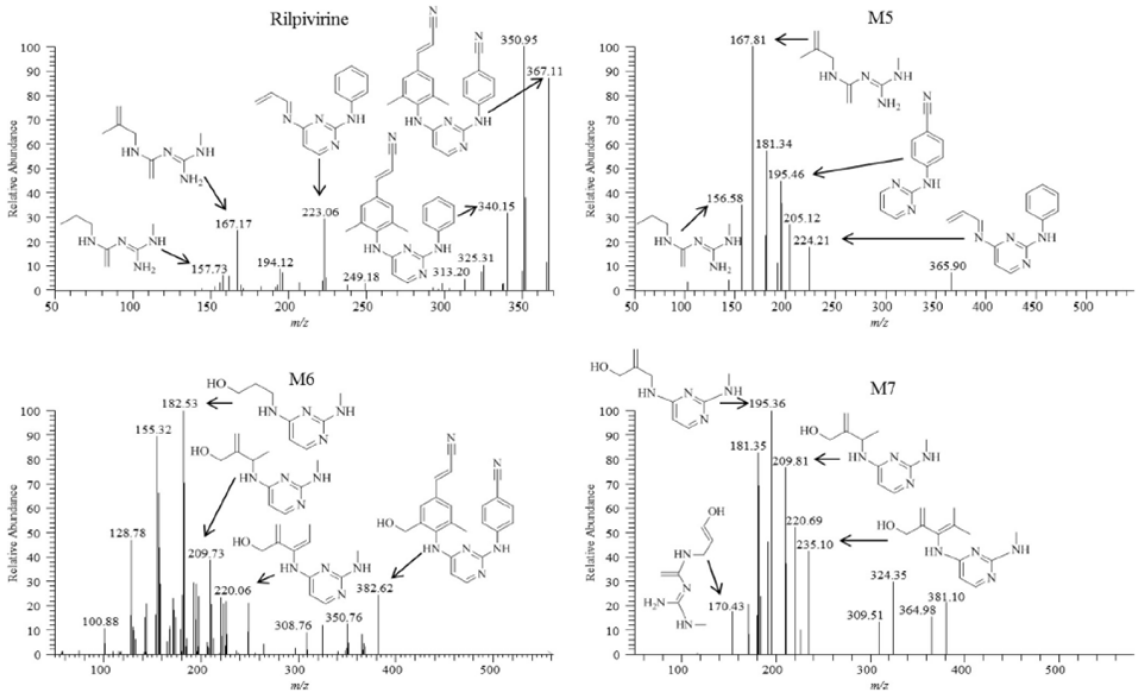

Figure 4. Fragmentation spectra of RPV (top) and glucuronidated metabolites M5 (top), M6 and M7 (bottom). Proposed modes of fragmentation are indicated by the fragment ion corresponding to the appropriate mass-to-charge ratio. Human liver microsomes (2 mg/ml) were incubated with 20 μM RPV for 60 min at 37°C in the presence of an NADPH-regenerating system and UDPGA. Metabolites were detected in MS/MS mode using parent masses of 367, 543, 559 ad 575 *m/z* for RPV, M5, M6 and M7, respectively. Spectra are representative of three individual experiments.

CYP3A4 and CYP3A5 are primarily responsible for the oxidative metabolism of RPV

Following identification of RPV metabolites, cDNA-expressed CYPs were employed in order to determine which CYP isozymes had the ability to catalyze the

formation of RPV metabolites. The cDNA-expressed CYPs used in these experiments were CYP1A2, -2B6, -2C8, -2C9, -2C19, -2D6, -3A4 and -3A5 and are representative of the principle drug metabolizing CYPs expressed in human liver (15). CYP3A5 was found to metabolize RPV to M1, M2, M3 and M4 metabolites at the greatest abundance, followed by CYP1A2 and CYP3A4 (Figure 5). CYP2C19 also displayed the ability to catalyze the formation of metabolite M3, while relatively minor formation of M3 by CYP2C9 was also observed.

Chemical inhibition experiments were performed in an effort to probe the role of each CYP in the biotransformation of RPV in a system in which all of the abovementioned isozymes were present. Human liver microsomes were pre-incubated for 5 min with DMSO vehicle or CYP inhibitor prior to the addition of RPV. Treatment of microsomes with 1 μM ketoconazole, which is an inhibitor of both CYP3A4 and CYP3A5 due to their high amino acid sequence similarities, resulted in the most significantly decreased formation of M1, M2, M3 and M4 metabolites relative to the DMSO control, with approximate decreases of 33.3 ± 6.3%, 30.5 ± 11.1%, 4.6 ± 2.3% and 8.1 ± 2.8%, respectively (n=3 ± SD). In addition, M1 formation was inhibited by 30 μM PPP (CYP2B6 inhibitor), 20 μM sulfaphenazole (CYP2C9 inhibitor) and 10 μM (+)-*N*-3-benzylnirvanol (CYP2C19 inhibitor) with decreases of 58.1 ± 17.2%, 64.8 ± 16.7% and 49.1 ± 17.4%, respectively, relative to DMSO control. (+)-*N*-3-benzylnirvanol additionally inhibited M2 formation with a decrease of 51.8 ± 17.2% as compared to control incubations. PPP and (+)-*N*-3-benzylnirvanol inhibited M3 formation as well with decreases of 59.5 ± 14.2% and 53.4 ± 14.3%, respectively, relative to the control

samples. Pre-treatment with furafylline (20 μM; CYP1A2 inhibitor) and 1 μM quinidine (CYP2D6 inhibitor) did not result in abrogation of oxidative metabolite formation.

Since RPV and the structurally similar antiretroviral drug etravirine were previously demonstrated to increase CYP3A4 mRNA expression (16-18), we tested whether RPV had the ability to autoinduce its own metabolism using primary human hepatocytes. Hepatocytes isolated from three donors were treated with either DMSO vehicle or 10 μM RPV for 6, 12 or 24 h. Hepatocyte medium was collected after each time point for UHPLC-MS/MS analysis (Figure 6). Hydroxylated metabolites, M1, M2, and M4 were detectable at all time points with the exclusion of M3, which was only observed at 6 h and 24 h. Glucuronides M5 and M6 were present at each time point examined following RPV treatment, however, glucuronide M7 was not detected in the medium of any of the three hepatocyte preparations. While metabolites M1 and M2 exhibited a trend towards an increase in abundance over 24 h of RPV treatment, these levels did not reach statistical significance; interestingly, an increase in the mRNA expression of CYP3A4 over time was indeed observed with fold changes of 7.4-fold (range, 2.3- to 17.4-fold), 8.8-fold (range, 3.05- to 13.6-fold) and 19.5-fold (range, 3.02- to 28.4-fold) relative to DMSO control for 6, 12 and 24 h, respectively.

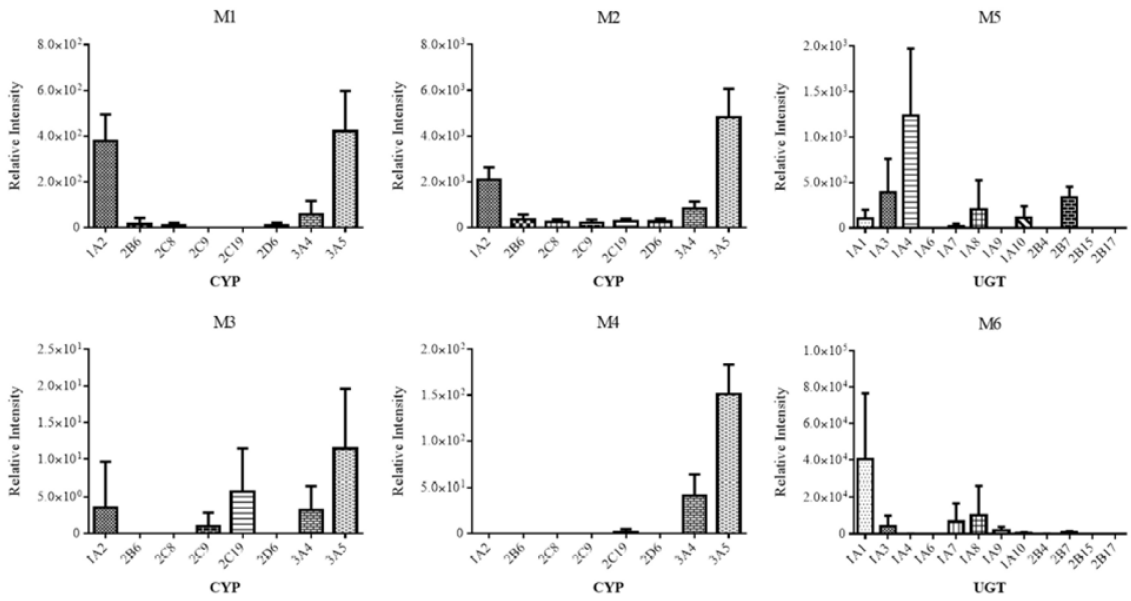

Figure 5. Relative contribution of individual drug metabolizing CYPs (left panel) and UGTs (right panel) to RPV metabolite formation. cDNA-expressed CYPs (10 pmol/ml) were incubated with 20 µM RPV for 30 min at 37°C in the presence of an NADPH-regenerating system. For UGT assays, cDNA-expressed CYP3A4 (10 pmol/ml) was pre-incubated with 20 µM RPV, an NADPH-regenerating system and UDPGA from 30 min at 37°C to which 0.2 mg/ml cDNA-expressed UGTs were added for an additional 60 min incubation. Metabolite formation was detected by UHPLC-MS/MS in SRM mode using the following transitions: 383→222 *m/z* (M1 and M2), 399→183 *m/z* (M3), 399→196 *m/z* (M4), 543→367 *m/z* (M5) and 559→383 *m/z* (M6). Glucuronide M7 was not detected under the UGT assay conditions. Data are representative of the mean relative peak intensities for n=3 ± SD.

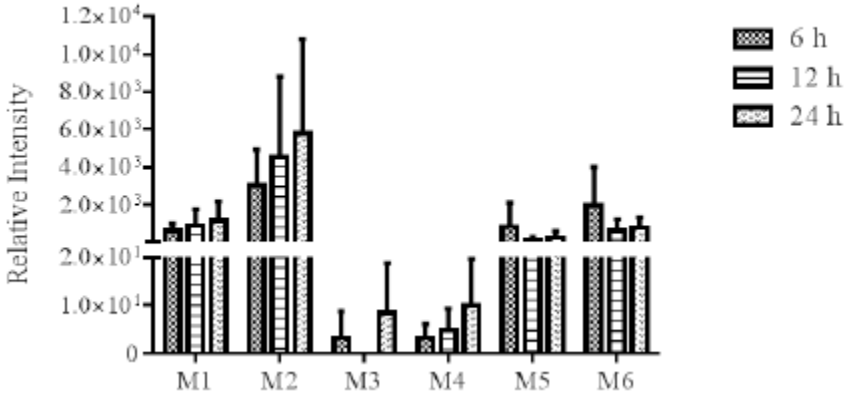

Figure 6. Metabolites detected in medium collected from RPV-treated primary human hepatocytes. Hepatocytes from three donors were treated with either DMSO or 10 μM RPV for 6, 12 and 24 h prior to medium collection for UHPLC-MS/MS analysis in SRM mode using the following transitions: 383→222 *m/z* (M1 and M2), 399→183 *m/z* (M3), 399→196 *m/z* (M4), 543→367 *m/z* (M5) and 559→383 *m/z* (M6). Glucuronide M7 formation was not detectable for any of the hepatocyte treatments. Data are representative of the mean relative intensities for three separate hepatocyte preparations n=3 ± 28 SD.

UGT1A1 and UGT1A4 contribute to glucuronidation of RPV and monooxygenated metabolite M2

In order to determine which individual UGT isozymes contribute to the formation of glucuronidated metabolites of RPV, denoted here as M5, M6 and M7, assays were performed using cDNA-expressed UGTs. Metabolite M5 was formed by direct *N*-linked glucuronidation of RPV on the pyrimidine ring in a non-NADPH-dependent manner as determined by incubation with human liver microsomes. The formation of glucuronides M6 and M7 were observed to be NADPH-dependent, suggesting initial oxygenation of

RPV prior to UGT-mediated conjugation with glucuronic acid. As such, CYP3A4 was used for co-incubations with individual cDNA-expressed UGT isozymes in the presence of RPV, a NADPH-regenerating system and UDPGA in order to ensure that the oxygenated metabolites were formed at levels that would allow for the facile detection of the subsequent glucuronide conjugated metabolites M6 and M7. The cDNA-expressed UGT isozymes used for these assays were UGT1A1, -1A3, -1A4, -1A6, -1A7, -1A8, -1A9, -1A10, -2B4, -2B7, -2B15 and -2B17, all of which are expressed in human liver (19). UGT1A4 was found to be primarily responsible for the formation of M5, and UGT1A1 was found to be primarily responsible for the formation of M6 (Figure 5). Glucuronide M7 was not formed under these experimental conditions using any of the UGTs tested.

In vivo detection of RPV metabolites in the plasma and urine of individuals receiving Complera™

In an effort to determine whether the metabolites that were identified through our *in vitro* studies were also formed *in vivo*, RPV metabolites were measured in plasma and urine collected from individuals receiving the RPV-containing drug Complera™, a co-formulation of RPV-tenofovir-emtricitabine The UHPLC-MS/MS SRM transitions developed for the analysis of *in vitro* metabolite formation by human liver microsomes and cDNA-expressed CYP and UGT isozymes were employed in detecting oxygenated and glucuronidated RPV metabolites in these clinical samples. While all of the metabolites that were identified *in vitro* were indeed detectable *in vivo*, variation in the abundance of metabolites was observed across the three subjects (Figure 7). Further,

although M7 was detectable in all of the urine samples that were analyzed, this metabolite was present in the plasma of only one subject. Monohydroxylated metabolites, M1 and M2, were more abundant in plasma than dihydroxylated metabolites, M3 and M4, while M4 was the most abundant oxygenated metabolite detected in urine. M5 was the most abundant glucuronide in plasma while M5 and M6 were observed to be similarly more abundant than glucuronide M7 in urine. Relative RPV plasma levels were determined to be approximately 70% of the combined non-metabolized drug and metabolite plasma levels in these subjects. Glucuronide M5 accounted for 24-34% of this total, followed by glucuronide M6 with 5-10% and monooxygenated M2 with 1-2%. M1, M3 and M4 metabolites accounted for <1% of the total. In contrast, RPV was found to be a relatively minor component of the urine collected as it only accounted for approximately <1% of the collective non-metabolized drug and metabolite levels in urine. The glucuronide urine levels for M5 and M6 were approximately 50% of total detectable drug and RPV metabolites, and M1, M2, M3, M4 and M7 accounted for <1%.

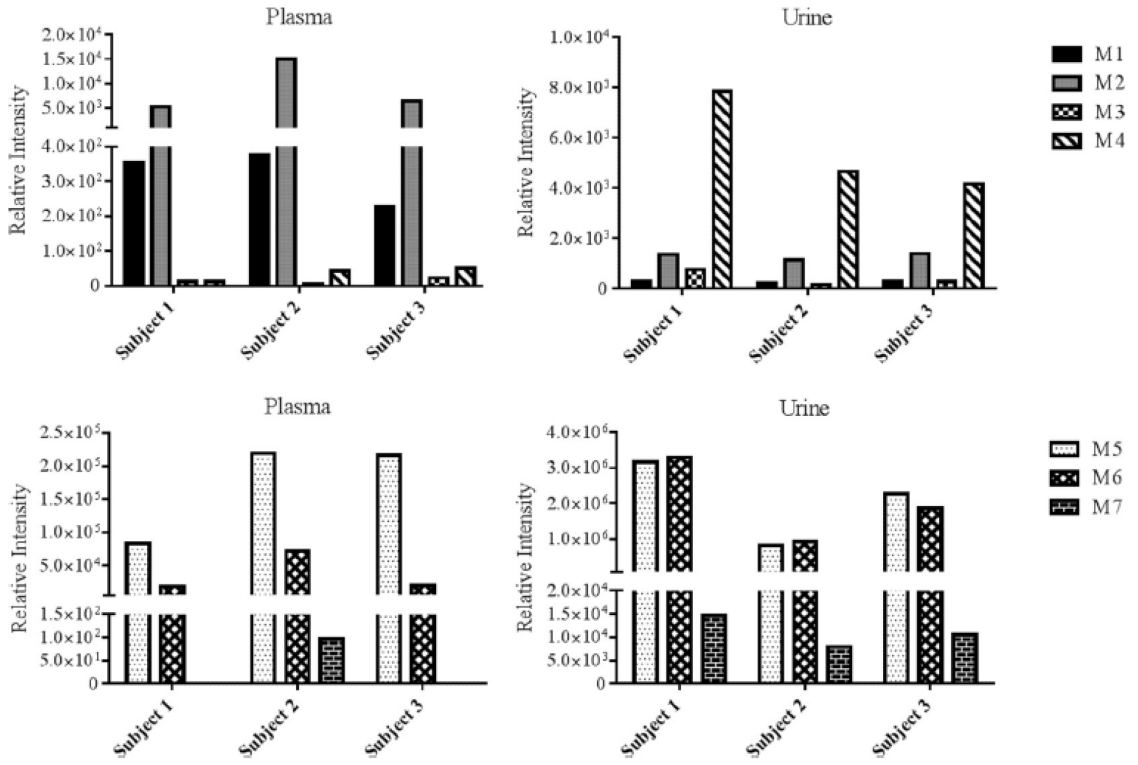

Figure 7. *In vivo* detection of RPV metabolites, M1 through M4 (top) and M5 through M7 (bottom) in human plasma and urine. Samples were collected from clinical subjects on a RPV-based antiretroviral regimen. Plasma and urine were extracted with acetonitrile in preparation for UHPLC-MS/MS analysis. Metabolites were detected in SRM mode using the following transitions: 383→222 *m/z* (M1 and M2), 399→183 *m/z* (M3), 399→196 *m/z* (M4), 543→367 *m/z* (M5), 559→383 *m/z* (M6) and 575→399 *m/z* (M7). Data shown are representative of three individual participants.

Comparison of Complera™ and Atripla™ endogenous metabolomic profiles using a UHPLC-MS/MS targeted screen

A novel UHPLC-MS/MS-based metabolomics screen was developed in an effort to characterize differences in the endogenous metabolomes of HIV-infected individuals receiving Complera™ (RPV-tenofovir-emtricitabine) or Atripla™ (efavirenz-tenofovir-emtricitabine). While the purpose of the analysis was to probe for variation in the levels of endogenous small molecules that participate in critical cellular processes in subjects being treated with each of these drugs, plasma and urine samples from HIV negative individuals that had not received Complera™ or Atripla™ were also measured. The latter samples were used to provide a context for understanding levels of these molecules in human subjects that have not previously been treated with either drug. In this screen, nineteen total metabolites, including essential and non-essential amino acids, nucleotides and key intermediates of the citric acid cycle, methionine-homocysteine cycle and urea cycle were targeted for detection by UHPLC-MS/MS (Tables 1 and 2) in the plasma and urine collected from both drug-treated groups as well as the non-infected, antiretroviral untreated group. Of the detectable endogenous metabolites, ten exhibited significant differences in relative abundance levels in the comparison of plasma and urine samples from the two treatment groups (Figure 8). Specifically, aspartate, glutamic acid, histidine, uridine, lysine and arginine were observed at lower levels in the plasma of those subjects treated with Atripla™. In contrast, levels of adenosine, homocysteine and tyrosine in plasma were higher in these subjects as compared to subjects receiving Complera™.

Finally, significantly lower levels of aspartate and succinic acid were also observed in the urine of the individuals on Atripla™ relative to those treated with Complera™.

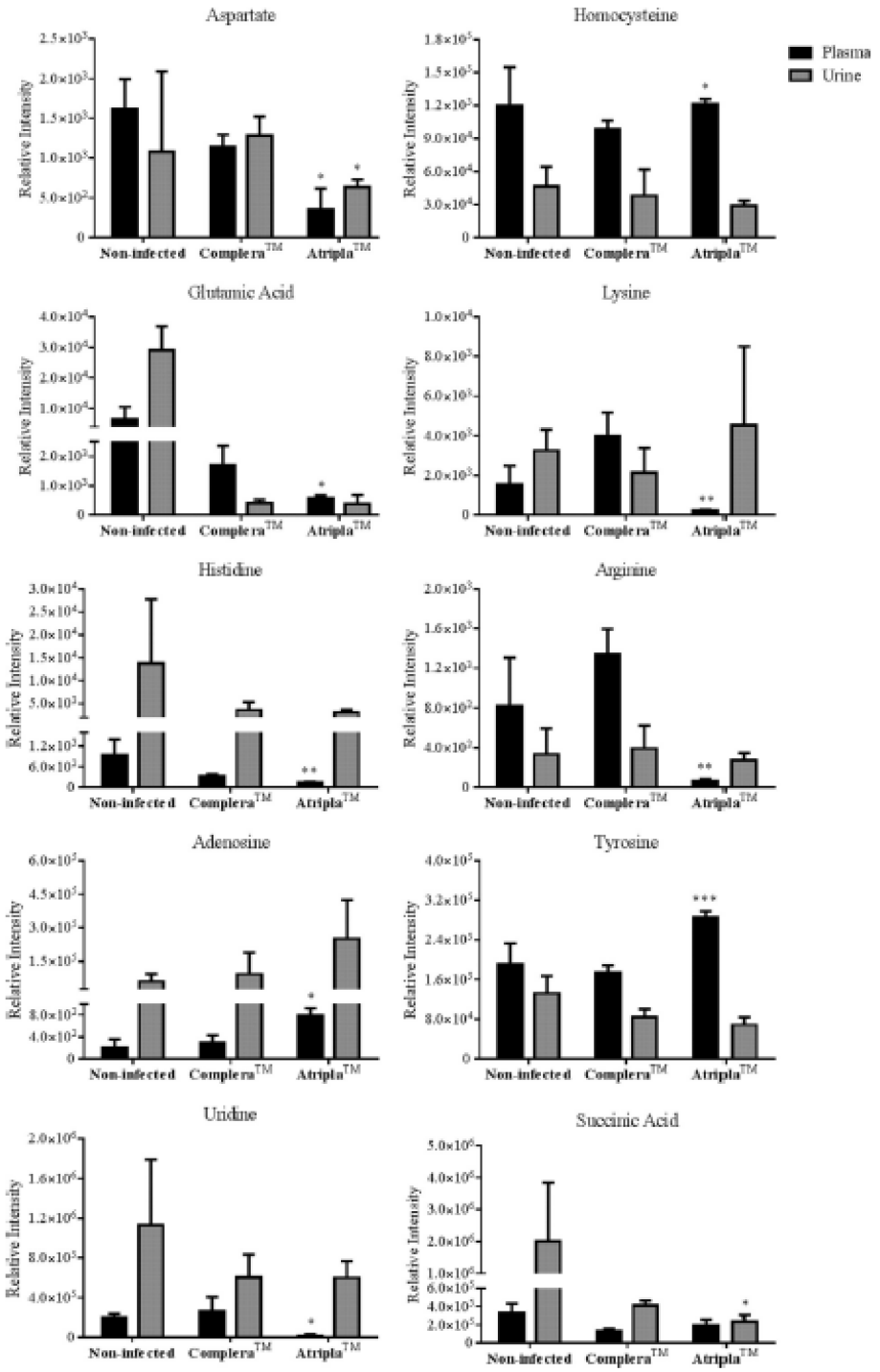

Figure 8. Metabolic profiles of plasma and urine collected from HIV-infected individuals receiving either Complera™ (RPV-tenofovir-emtricitabine) or

Atripla™ (efavirenz-tenofovir-emtricitabine). The observed relative abundances of each analyte are shown alongside those in plasma and urine collected from non-infected, antiretroviral untreated individuals. The data for the ten endogenous metabolites, of the nineteen monitored, that were determined to be significantly different in either the plasma, urine or both between the drug-treated groups are shown. Plasma and urine was extracted with acetonitrile in preparation for UHPLC-MS/MS analysis. The relative abundance of each metabolite was detected in SRM mode using either positive or negative ionization. The transitions that were used for each analyte are listed in Tables S1 and S2. Data are representative of the mean relative intensities for three subjects per treatment, n=3 ± SD. Statistical significance of Atripla™ treatment from Complera™ are indicated as: *, $p < 0.05$; **, $p < 0.01$; and ***, $p < 0.001$.

RPV oxidative and glucuronide metabolite formation across species

The metabolism of RPV by a range of species used in preclinical drug development was investigated in order to determine whether biotransformation of RPV by any of these animals paralleled what we observed in humans. Using liver microsomes, monohydroxylated metabolites, M1 and M2, as well as dihydroxylated metabolites, M3 and M4, were found to be formed at varying abundance by each species of the ten mammals that were investigated in these studies (Figure 9). Interestingly, the formation of M1, M2 and M3 by Golden Syrian hamster liver microsomes were an approximate 11.0-fold, 4.6-fold and 4.3-fold, respectively, greater than production by human liver microsomes. However, all of these species formed metabolite M4 at lower levels than was observed using human liver microsomes. RPV glucuronide formation was observed

to also be rather conserved across species (Figure 10). The abundance of glucuronide, M5, which we have previously identified in human plasma to be the predominant *in vivo* glucuronidated metabolite, was greatest in the beagle, Sinclair minipig, rhesus monkey and New Zealand rabbit liver microsomal incubations. The lowest levels of M5 production was observed when Golden Syrian hamster, BALB/c mouse and CD1 mouse liver microsomes were employed. In addition, the formation of the glucuronidated metabolite M7 was greater using Golden Syrian hamster liver microsomes than human liver microsomes.

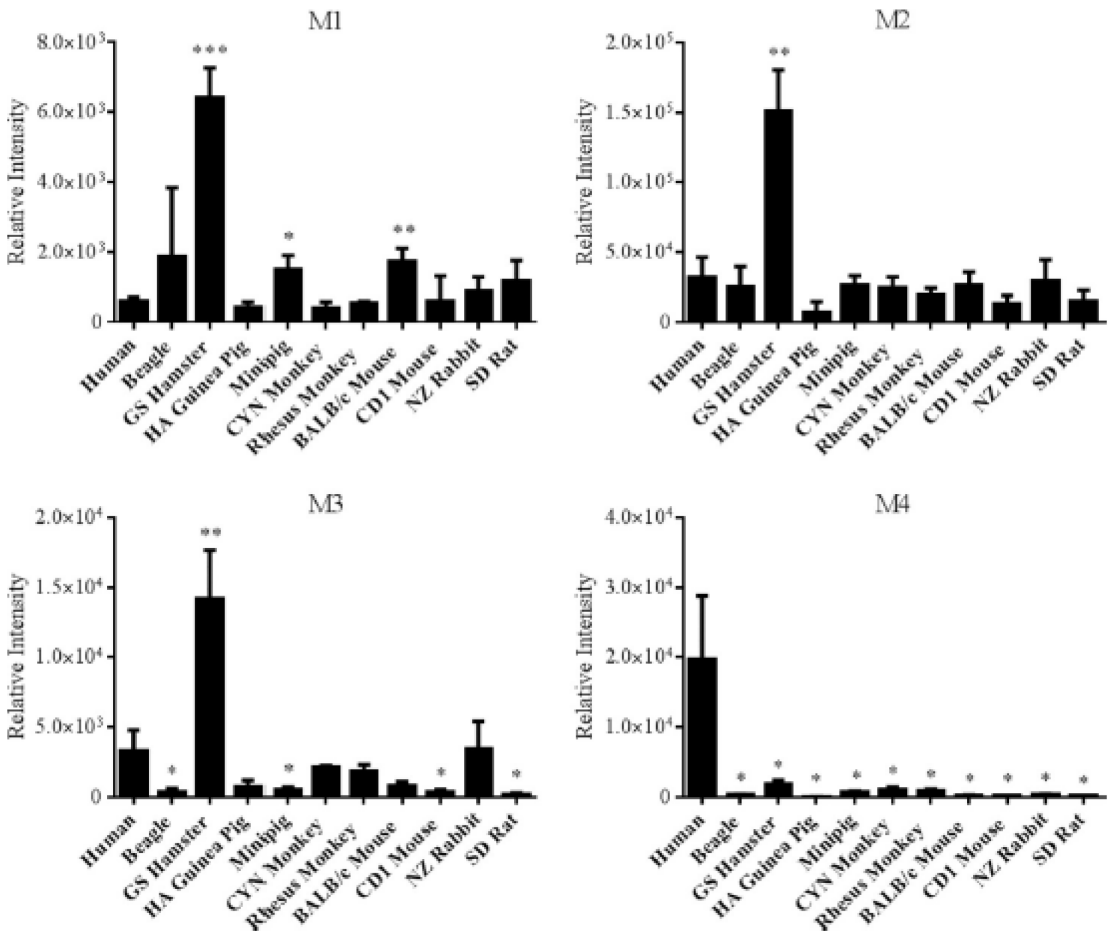

Figure 9. Comparison of RPV oxidative metabolism across species. Liver microsomes (2 mg/ml) from the following species: human, beagle, Golden Syrian (GS) hamster, Hartley Albino (HA) guinea pig, Sinclair minipig, cynomolgus (CYN) monkey, rhesus monkey, BALB/c mouse, CD1 mouse, New Zealand (NZ) rabbit and Sprague Dawley (SD) rat were incubated with 20 µM RPV for 30 min at 37°C in the presence of an NADPH-regenerating system. RPV metabolites were detected by UHPLC-MS/MS in SRM mode using the following transitions: 383→222 *m/z* (M1 and M2), 399→183 *m/z* (M3), 399→196 *m/z* (M4). Data are representative of the mean relative intensities for n=3

± SD. Statistical significances from human liver microsome metabolite formation are indicated as: *, $p < 0.05$; **, $p < 0.01$; and ***, $p < 0.001$.

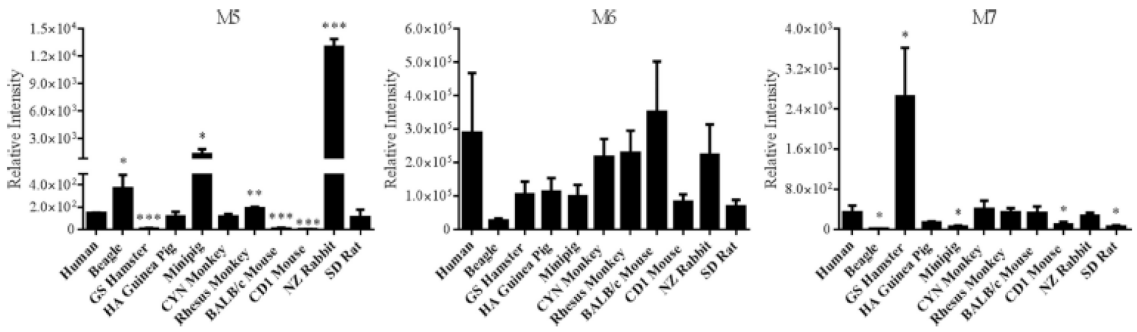

Figure 10. Comparison of RPV phase II metabolism across species. Liver microsomes (2 mg/ml) from the following species: human, beagle, Golden Syrian (GS) hamster, Hartley Albino (HA) guinea pig, Sinclair minipig, cynomolgus (CYN) monkey, rhesus monkey, BALB/c mouse, CD1 mouse, New Zealand (NZ) rabbit and Sprague Dawley (SD) rat were incubated with 20 μM RPV for 60 min at 37°C in the presence of an NADPH-regenerating system and UDPGA. Metabolites were detected by UHPLC-MS/MS in SRM mode using the following transitions: 543→367 *m/z* (M5), 559→383 *m/z* (M6) and 575→399 *m/z* (M7). Data are representative of the mean relative intensities for n=3 ± SD. Statistical significances from human liver microsome glucuronide formation are indicated as: *, $p < 0.05$; **, $p < 0.01$; and ***, $p < 0.001$.

Discussion

In this study, the routes of RPV metabolism were systematically investigated in order to identify the metabolites of RPV as well as the enzymes that contribute to the formation of these products (Figure 11). In total, seven RPV metabolites were characterized. Tandem mass spectral analysis revealed that the oxidative metabolites, denoted as M1 through M4, resulted from mono- or di-oxygenation of the 2,6-dimethylphenyl ring itself or either of the two methyl groups located on this phenyl ring. Even though we did indeed observe distinct fragments for M1 and M2, there were a number of similarities in the fragmentation spectra of these metabolites that made it difficult to definitively assign oxygen insertion onto the methyl group or the 2,6-dimethylphenyl ring for either of these metabolites; however, due to the fact that the methyl group of the 2,6-dimethylphenyl ring may be more readily accessible for oxygenation as compared to direct oxygen insertion on one of the carbon atoms within the phenyl ring, we propose that it is reasonable for M2 to result from methylhydroxylation of RPV since it was observed at an apparent greater abundance than M1. Glucuronide M5 resulted from direct *N*-linked glucuronidation of RPV, and glucuronides M6 and M7 were proposed to be produced via *O*-linked glucuronidation of mono- and di- hydroxymethyl metabolites M2 and M4, respectively. Fecal excretion has been previously demonstrated to be the primary route of RPV clearance (20). Although we did not analyze fecal samples in the present study, using plasma and urine from individuals receiving a RPV-containing regimen we were able to demonstrate that all of the metabolites that were identified here *in vitro* were indeed formed *in vivo*.

Complementary liver microsomal metabolism studies were performed in order to examine the conservation of RPV biotransformation across species. While the assay developed here to monitor metabolite formation were not quantitative, it facilitated the identification of RPV metabolites and perhaps lays the foundation for the development of a quantitative assay for the measurement of RPV metabolites. Synthetic standards are required in order to definitively determine the levels of these molecules since differences in ionization could contribute to the observed variability in relative abundances. As such, the results presented here can be used to guide the synthesis of RPV metabolite standards for this purpose. Interestingly, each of the species investigated in these studies were able to form all of the metabolites of RPV that were observed in humans, with Golden Syrian hamster liver microsomes being the only to produce several metabolites of RPV to greater abundance than human liver microsomes. Further, no additional metabolites beyond those that were identified through the human liver microsomal metabolism assays were produced in the incubations performed using liver microsomes isolated from the non-human animals. These data suggest that several of these animals may have utility as preclinical species for use in studies to gain an increased understanding of RPV exposure *in vivo*.

The present study is the first to report primary data detailing the routes of RPV metabolism. As demonstrated through the use of cDNA-expressed CYP isozymes, CYP1A2, -3A4 and -3A5 were able to catalyze the oxygenation of RPV to products M1 through M4. Subsequent chemical inhibition experiments revealed that CYP3A4 and CYP3A5 were predominantly responsible for mono- and di-oxygenation of RPV, as the

most significant reduction in metabolite formation was observed with the dual CYP3A4/5 inhibitor ketoconazole. Treatments with furafylline, a mechanism-based inactivator of CYP1A2 (21), did not block metabolite formation. This could be the result of compensation of the loss of CYP1A2 activity by another CYP isozyme, for instance CYP3A4 and/or CYP3A5, resulting in a lack of a significant decrease in RPV metabolism following chemical inhibition of CYP1A2. We observed statistically significant inhibition of M1 formation following incubation of liver microsomes with chemical inhibitors of CYP2B6 (PPP), CYP2C9 (sulfaphenazole) and CYP2C19 ((+)-*N*-3-benzylnirvanol); however, RPV was not metabolized to M1 by cDNA-expressed CYP2B6, CYP2C9 or CYP2C19. This variability in the catalytic activities of cDNA-expressed isozymes as compared to human liver microsomes could be the result of differences in the protein concentrations of each CYP in these two systems in addition to the fact that in human liver microsomes RPV was being concurrently metabolized to all of the oxygenated products. As such, the overall kinetics of formation differ in these two assays. Still, the studies using both cDNA-expressed isozymes and human liver microsomes were congruent and demonstrated a primary role for CYP3A4 and CYP3A5 in RPV oxidative metabolism.

A recent report demonstrated that RPV, similar to the non-nucleoside reverse transcriptase inhibitors etravirine and efavirenz, was able to activate the pregnane X receptor in primary human hepatocytes (17). The pregnane X receptor is a key regulator of drug metabolizing enzymes including CYP3A and UGT1A isozymes (22-24). In our study, although we were able to recapitulate the increase in CYP3A4 mRNA expression

following incubation of primary human hepatocytes with RPV, we did not observe an increase in the abundance of RPV metabolites via UHPLC-MS/MS analysis of the hepatocyte medium. Oxidative metabolism did not appear to be shunted to glucuronic acid conjugation as the glucuronides that were detectable in the hepatocyte medium, namely metabolites M5 and M6, also did not exhibit an increase in abundance over the 24 h incubation time. Although we have previously reported that autoinduction of etravirine metabolism is readily detectable following 24 h of incubation with primary human hepatocytes (17), longer treatment times may be required to observe this effect using RPV. For instance, CYP3A4 protein may not have yet been elevated over the time points that we measured. Further, the metabolites may not be stable in culture medium, thereby resulting in our inability to detect increases in metabolite levels over time. This would need to be tested using synthetic standards for each of these molecules.

Assays performed using cDNA-expressed UGT isozymes demonstrated that UGT1A1 and UGT1A4 were able to catalyze the conjugation of glucuronic acid to moonoxygenated metabolite M2 and RPV, respectively. These results correlated well with our proposed glucuronide metabolite structures as UGT1A1 is known to facilitate alkyl- and aryl-*O*-glucuronidation while UGT1A4 has been demonstrated to participate in the *N*-glucuronidation of tertiary amines (25). UGT1A1 and UGT1A4 are members of the *UGT1A* gene superfamily and are most abundantly expressed in the human liver. Of note, glucuronide M7 was not formed by any of the cDNA-expressed UGT isozymes tested under our experimental conditions, nor was this product detectable in hepatocyte medium following up to 24 h of incubation with RPV; however, metabolite M7 was detectable in

the urine of all three subjects receiving Complera™ that were analyzed in this study in addition to being present in the plasma of one of the subjects. As such, this metabolite that was initially identified through the use of human liver microsomes appears to indeed be formed *in vivo*. M7 may be produced by a UGT isozyme beyond those tested and the lack of formation in the primary human hepatocytes may be due to inter-individual variability (the human liver microsomes are isolated from a pool of 50 donors) and/or lower levels of drug metabolizing enzyme expression as a result of the isolation or culturing of the hepatocytes. Since this metabolite was observed to be the more minor of the glucuronides detected *in vivo*, its formation may be more sensitive to the aforementioned variables.

We sought to probe for potential differential physiological effects of a RPV-containing therapy versus an efavirenz-containing therapy through analysis of the plasma and urine endogenous metabolomes. Since analysis at the level of the metabolome can generate large volumes of data, we opted to prioritize the pathways that we investigated. To this end, we developed a targeted UHPLC-MS/MS-based method to detect thirty-two intracellular metabolites that have been demonstrated to play a role in maintaining cellular homeostasis. Further, while global metabolomics provides relative quantitation of intracellular small molecules, a targeted approach allows for markedly improved detection of less abundant chemical species. Tyrosine plasma levels were observed to be higher in Atripla™ subjects. In a reaction that predominantly occurs in the liver, the essential amino acid phenylalanine is converted to tyrosine via phenylalanine hydroxylase (26). Phenylalanine plasma levels, however, were comparable between

subject groups, suggesting a potential increase in phenylalanine hydroxylase activity with an efavirenz-containing treatment as compared to a RPV-based regimen, thus resulting in the increased synthesis of tyrosine byproduct. Homocysteine and adenosine plasma levels were also greater with Atripla™ drug therapy. The *S*-adenosylmethionine-dependent transmethylation pathway, which is extensively active in the liver, is responsible for the synthesis of homocysteine and adenosine through the hydrolysis of *S*-adenosylhomocysteine via *S*-adenosylhomocysteine hydrolase (27). Interestingly, methionine plasma levels were comparable between treatments. As part of the transmethylation cycle, the conversion of homocysteine to methionine is regulated by methionine synthase (34); therefore, we would anticipate observing greater methionine levels in the plasma Atripla™ samples. This, however, was not observed suggesting possible impairment of methionine synthase activity with Atripla™ treatment. Moreover, it is also plausible that methionine plasma levels remain unchanged as a result of immediate conversion to *S*-adenosylmethionine. The small molecules, *S*-adenosylhomocysteine and *S*-adenosylmethionine, were initially included in this metabolomics screen, yet neither was consistently detectable in these biological samples.

Aspartate and arginine are two examples of metabolites that were both observed to be in lower abundance in the plasma collected from the Atripla™ drug treatment group relative to those receiving Complera™. Interestingly, lower arginine plasma levels have been observed to parallel decreasing HIV RNA levels with an established antiretroviral drug regimen (28). Moreover, arginine and aspartate are key components of the urea cycle where argininosuccinate synthase catalyzes the conversion of aspartate to

argininosuccinate that is further hydrolyzed into arginine and fumarate via argininosuccinate lyase, ultimately producing urea (29). Lower arginine and aspartate levels would suggest an increase in the activity of both argininosuccinate synthase and argininosuccinate lyase enzymes. Separate from its role in the urea cycle, lower aspartate plasma levels can result from increased aspartate aminotransferase activity, which catalyzes the conversion of the amino acid and α-ketoglutarate to oxaloacetate and glutamate, and has served as a biomarker for diagnosing fibrosis and cirrhosis of the liver in individuals co-infected with HIV and the hepatitis C virus (30). This proposed mechanism is challenging to fully assess since α-ketoglutarate and oxaloacetate were not detectable in these samples by UHPLC-MS/MS analysis and glutamic acid plasma levels were also observed to be lower in those receiving Atripla™. Potential confounding factors for our analyses include the fact that the subjects involved in this study could have co-morbidities or be concomitantly taking medications that might also have an impact on their plasma and urine metabolomes. In addition, due to the small sample size we cannot rule out potential effects of the mean age difference between the subjects receiving Atripla™ or Complera™. However, the levels of the endogenous small molecules that we measured were consistent amongst individuals within each of the drug treatment groups so much so that the standard deviations were less than 5% indicating that there may indeed be distinct endogenous small molecule signatures that can be attributed to RPV- and efavirenz-containing regimens. Further, these data demonstrate for the first time that endogenous metabolites can be readily detected in plasma and urine of individuals receiving these drugs and we provide an assay that can be applied broadly in

measuring these molecules in biological matrices. Overall, these endogenous metabolomic studies need to be further extended to a larger population of individuals for both Complera™ and Atripla™ subject groups; however, the present findings suggest possible biochemical pathways that can be tested for modulation by Complera™ and Atripla™.

In summary, this study has defined the *in vitro* routes of phase I (primarily CYP3A4/5) and phase II (glucuronic acid conjugation) RPV metabolism. Additionally, RPV metabolism was observed to be conserved across a range of mammals and these data should inform the selection of preclinical animal models for subsequent investigation of RPV pharmacology and/or toxicology *in vivo*. Taken together, these data provide novel insight into the biotransformation of RPV.

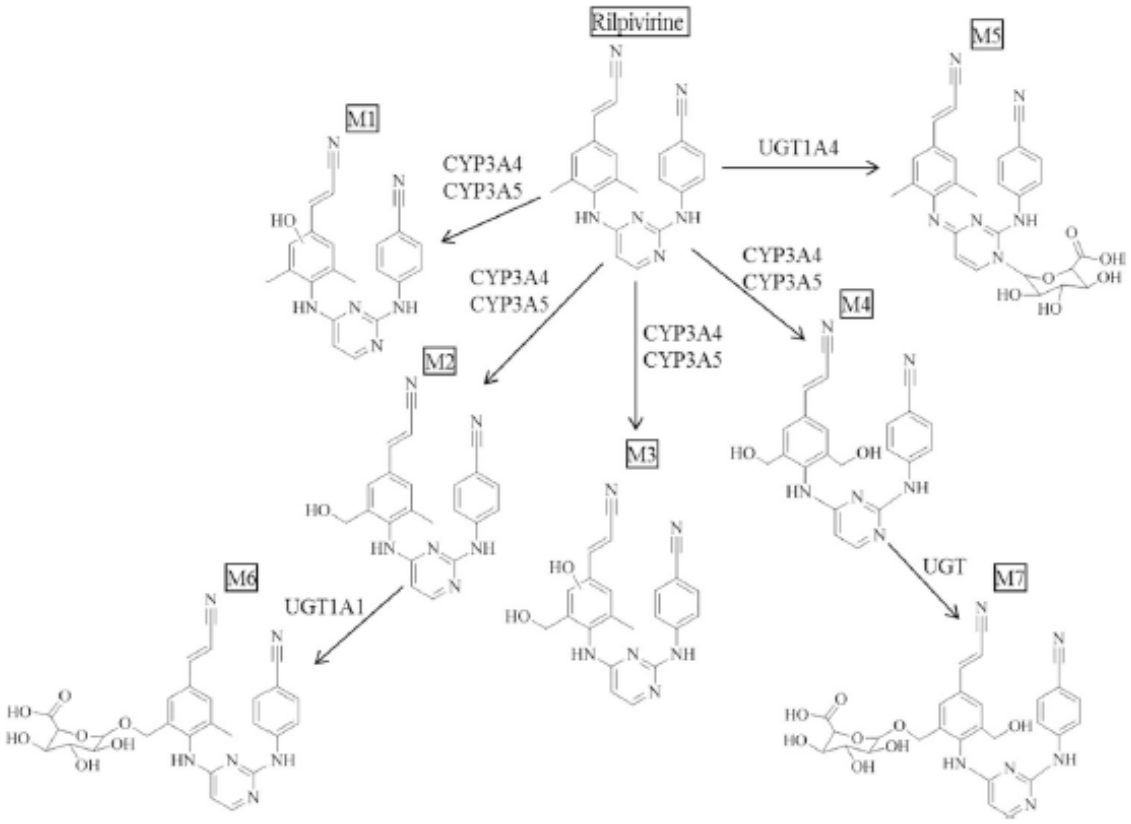

Figure 11. Schematic summarizing the phase I and phase II metabolism of RPV. Monohydroxylated metabolites, M1 and M2, and dihydroxylated metabolites, M3 and M4, result from oxygenation of RPV by CYP3A4 and CYP3A5. M5 results from direct glucuronic acid conjugation to RPV by UGT1A4. M6 results from glucuronidation of monooxygenated metabolite M1 by UGT1A1, and M7 results from glucuronidation of dioxygenated metabolite M4, however, the UGT responsible for this conjugation was unable to be determined from our studies.

References

1. Wainberg MA. Combination therapies, effectiveness, and adherence in patients with HIV infection: clinical utility of a single tablet of emtricitabine, rilpivirine, and tenofovir. HIV AIDS (Auckl). 2013;5:41-9. PMCID: 3570078.

2. Andries K, Azijn H, Thielemans T, Ludovici D, Kukla M, Heeres J, et al. TMC125, a novel next-generation nonnucleoside reverse transcriptase inhibitor active against nonnucleoside reverse transcriptase inhibitor-resistant human immunodeficiency virus type 1. Antimicrob Agents Chemother. 2004;48(12):4680-6. PMCID: 529207.

3. Janssen PA, Lewi PJ, Arnold E, Daeyaert F, de Jonge M, Heeres J, et al. In search of a novel anti-HIV drug: multidisciplinary coordination in the discovery of 4-[[4-[[4-[(1E)-2-cyanoethenyl]-2,6-dimethylphenyl]amino]-2- pyrimidinyl]amino]benzonitrile (R278474, rilpivirine). J Med Chem. 2005;48(6):1901-9.

4. Abraham BK, Gulick R. Next-generation oral preexposure prophylaxis: beyond tenofovir. Curr Opin HIV AIDS. 2012;7(6):600-6.

5. Baert L, van 't Klooster G, Dries W, Francois M, Wouters A, Basstanie E, et al. Development of a long-acting injectable formulation with nanoparticles of rilpivirine (TMC278) for HIV treatment. Eur J Pharm Biopharm. 2009;72(3):502-8.

6. Cohen CJ, Andrade-Villanueva J, Clotet B, Fourie J, Johnson MA, Ruxrungtham K, et al. Rilpivirine versus efavirenz with two background nucleoside or nucleotide reverse transcriptase inhibitors in treatment-naive adults infected with HIV-1 (THRIVE): a phase 3, randomised, non-inferiority trial. Lancet. 2011;378(9787):229-37.

7. Molina JM, Cahn P, Grinsztejn B, Lazzarin A, Mills A, Saag M, et al. Rilpivirine versus efavirenz with tenofovir and emtricitabine in treatment-naive adults infected with HIV-1 (ECHO): a phase 3 randomised double-blind active-controlled trial. Lancet. 2011;378(9787):238-46.

8. Bumpus NN. Efavirenz and 8-hydroxyefavirenz induce cell death via a JNK- and BimEL-dependent mechanism in primary human hepatocytes. Toxicol Appl Pharmacol. 2011;257(2):227-34.

9. Tovar-y-Romo LB, Bumpus NN, Pomerantz D, Avery LB, Sacktor N, McArthur JC, et al. Dendritic spine injury induced by the 8-hydroxy metabolite of efavirenz. J Pharmacol Exp Ther. 2012;343(3):696-703. PMCID: 3500535.

10. Pharmaceuticals T. Edurant™ (rilpivirine) tablets full prescribing information. County Cork, Ireland. 2011.

11. Gilead Sciences I. Complera™ highlights of prescribing information. Foster City, CA. 2011.

12. Suzuki H, Kneller MB, Haining RL, Trager WF, Rettie AE. (+)-N-3-Benzyl-nirvanol and (-)-N-3-benzyl-phenobarbital: new potent and selective in vitro inhibitors of CYP2C19. Drug Metab Dispos. 2002;30(3):235-9.

13. Walsky RL, Obach RS. A comparison of 2-phenyl-2-(1-piperidinyl)propane (ppp), 1,1',1"-phosphinothioylidynetrisaziridine (thioTEPA), clopidogrel, and ticlopidine as selective inactivators of human cytochrome P450 2B6. Drug Metab Dispos. 2007;35(11):2053-9.

14. Ward BA, Gorski JC, Jones DR, Hall SD, Flockhart DA, Desta Z. The cytochrome P450 2B6 (CYP2B6) is the main catalyst of efavirenz primary and secondary metabolism: implication for HIV/AIDS therapy and utility of efavirenz as a substrate marker of CYP2B6 catalytic activity. J Pharmacol Exp Ther. 2003;306(1):287-300.

15. Ingelman-Sundberg M, Sim SC. Pharmacogenetic biomarkers as tools for improved drug therapy; emphasis on the cytochrome P450 system. Biochem Biophys Res Commun. 2010;396(1):90-4.

16. Sharma D, Lau AJ, Sherman MA, Chang TK. Agonism of human pregnane X receptor by rilpivirine and etravirine: comparison with first generation non-nucleoside reverse transcriptase inhibitors. Biochem Pharmacol. 2013;85(11):1700-11.

17. Yanakakis LJ, Bumpus NN. Biotransformation of the antiretroviral drug etravirine: metabolite identification, reaction phenotyping, and characterization of autoinduction of cytochrome P450-dependent metabolism. Drug Metab Dispos. 2012;40(4):803-14. PMCID: 3310427.

18. Weiss J, Haefeli WE. Potential of the novel antiretroviral drug rilpivirine to modulate the expression and function of drug transporters and drug-metabolising enzymes in vitro. Int J Antimicrob Agents. 2013;41(5):484-7.

19. Ohno S, Nakajin S. Determination of mRNA expression of human UDP-glucuronosyltransferases and application for localization in various human tissues by real-time reverse transcriptase-polymerase chain reaction. Drug Metab Dispos. 2009;37(1):32-40.

20. Levin J. Absorption, metabolism and excretion of TMC278, an NNRTI, after a single oral dose of 150mg in healthy male volunteers 12th European AIDS Conference.

21. Fairman DA, Collins C, Chapple S. Progress curve analysis of CYP1A2 inhibition: a more informative approach to the assessment of mechanism-based inactivation? Drug Metab Dispos. 2007;35(12):2159-65.

22. Willson TM, Kliewer SA. PXR, CAR and drug metabolism. Nat Rev Drug Discov. 2002;1(4):259-66.

23. Moore LB, Maglich JM, McKee DD, Wisely B, Willson TM, Kliewer SA, et al. Pregnane X receptor (PXR), constitutive androstane receptor (CAR), and benzoate X receptor (BXR) define three pharmacologically distinct classes of nuclear receptors. Mol Endocrinol. 2002;16(5):977-86.

24. Gardner-Stephen D, Heydel JM, Goyal A, Lu Y, Xie W, Lindblom T, et al. Human PXR variants and their differential effects on the regulation of human UDP-glucuronosyltransferase gene expression. Drug Metab Dispos. 2004;32(3):340-7. PMCID: 2652677.

25. Tukey RH, Strassburg CP. Human UDP-glucuronosyltransferases: metabolism, expression, and disease. Annu Rev Pharmacol Toxicol. 2000;40:581-616.

26. Hufton SE, Jennings IG, Cotton RG. Structure and function of the aromatic amino acid hydroxylases. Biochem J. 1995;311 (Pt 2):353-66. PMCID: 1136008.

27. Williams KT, Schalinske KL. Homocysteine metabolism and its relation to health and disease. Biofactors. 2010;36(1):19-24.

28. Kurz K, Teerlink T, Sarcletti M, Weiss G, Zangerle R, Fuchs D. Asymmetric dimethylarginine concentrations decrease in patients with HIV infection under antiretroviral therapy. Antivir Ther. 2012;17(6):1021-7.

29. Haines RJ, Pendleton LC, Eichler DC. Argininosuccinate synthase: at the center of arginine metabolism. Int J Biochem Mol Biol. 2011;2(1):8-23. PMCID: 3074183.

30. Resino S, Sanchez-Conde M, Berenguer J. Coinfection by human immunodeficiency virus and hepatitis C virus: noninvasive assessment and staging of fibrosis. Curr Opin Infect Dis. 2012;25(5):564-9.

Chapter 3: Identification of Cytochrome P450 and Uridine Diphosphate Glucuronosyltransferase Genetic Variants in Participants of the HIV Prevention Trial Network Study HPTN 076

Abstract

Rilpivirine (RPV) is a second-generation non-nucleoside reverse transcriptase inhibitor FDA-approved in 2011 for administration to treatment-naïve HIV infected adults and is under current investigation as long-acting injectable formulation (RPV-LA) for use in HIV maintenance therapy as well as in pre-exposure prophylaxis (PrEP). The phase II clinical trial HPTN 076 investigated the safety and acceptability of a RPV-LA injectable for use in PrEP. We isolated genomic DNA from HIV-uninfected female participants (n=136) of the HPTN 076 study for next-generation sequence of the coding regions for *CYP3A4*, *CYP3A5*, *UGT1A1* and *UGT1A4* in order to investigate the presence of genetic polymorphisms that may impact RPV metabolism. A total of 12 previously reported *CYP3A4* genetic variants were detected in 56 (41%) participants, 20 previously reported *CYP3A5* genetic variants were detected in 129 (95%) participants, 8 previously reported *UGT1A1* genetic variants were detected in 134 (99%) participants, and 20 previously reported *UGT1A4* genetic variants were detected in 135 (100%) participants. In addition, RPV and its primary oxidative metabolite 2-hydroxymethyl RPV (M2) were quantitated in the plasma of HPTN 076 participants (n=83) taking 25 mg RPV once-daily for four weeks. Mean parent and M2 levels were determined to be 77.77 ng/mL ± 57.93 ng/mL and 3.04 ng/mL ± 1.60 ng/mL, respectively. Further, loss of function *CYP3A5* alleles detected in these HPTN 076 participants demonstrated a trend of decreased

metabolite M2 formation. In summary, genetic variants have been identified in the genes encoding the enzymes that contribute to RPV metabolism, which could compromise drug biotransformation adding to interindividual variability and potentially impact the occurrence of drug-associated toxicities.

Introduction

Rilpivirine (RPV) is a second-generation non-nucleoside reverse transcriptase inhibitor (NNRTI) that was one of a series of diarylpyrimidine (DAPY) small molecules designed using a novel multidisciplinary approach by Janssen Pharmaceuticals (1). This drug class has an inherent degree of flexibility and rotational freedom that enable DAPY molecules to bind in multiple modalities to the NNRTI binding pocket of the HIV reverse transcriptase enzyme thereby allowing for adaptation to potential resistance mutations (1). RPV was FDA-approved in 2011 for administration to treatment-naïve HIV infected adults and because it was found to be highly efficacious and well tolerated with chronic oral administration, it was concurrently developed into a long-acting injectable formulation (RPV-LA) (2). One can envision that less frequent dosing of an antiretroviral due to an extended drug half-life may improve compliance as this is a primary contributor to the development of viral resistance. In addition to use for HIV maintenance therapy, RPV-LA is presently under investigation for use in pre-exposure prophylaxis (PrEP).

PrEP is a preventative drug strategy for uninfected adults at risk of acquiring HIV by either sexual or blood-born transmission. As of 2015, WHO guidelines recommend PrEP should be offered to populations with an HIV infection rate of 3 in 100 people per year, which includes but is not limited to serodiscordant couples, men who have sex with

men, transgender women and people who inject drugs (3). The notion of dosing a healthy individual long-term with an antiretroviral first became most plausible with the 2001 approval of the nucleoside reverse transcriptase inhibitor tenofovir (TFV).

As TFV was proven to be an effective agent for use in treating HIV infection, it became a clear candidate for further exploration in PrEP under varying formulations and in differing target populations. For example, the CAPRISA 004 trial provided the first evidence that a 1% TFV microbicide gel applied vaginally before and after sex could reduce the risk of infection by 39%, 54% when corrected for adherence, in HIV-uninfected women (4). TFV, however, is only approved for oral administration as the prodrug TDF and is commonly coformulated with the nucleoside analog emtricitabine (FTC) as a backbone for NNRTIs, such as efavirenz and RPV, for HIV maintenance therapy. To that end, the Preexposure Prophylaxis Initiative (iPrEx) trial was the first study to report efficacy for oral dosing of TDF-FTC in seronegative men and transgender women, observing a 44% risk reduction in HIV transmission, an overall 92% reduction when adjusting for detectable levels of TFV in blood (5). Taking this work a step further in serodiscordant couples, our laboratory contributed to the Partners PrEP study showing once-daily TDF alone or TDF-FTC decreased the rate of HIV infection by 67% and 75%, respectively, with a greater than 85% relative risk reduction in participants who had detectable TFV concentrations in blood regardless of the formulation (6). Furthermore, the data acquired from pivotal clinical trials, such as iPrEx and Partners PrEP, clearly demonstrated that the coformulation of TDF-FTC is effective at reducing the risk of HIV

infection through sexual transmission giving way to Truvada as the first, and currently the only, approved drug for HIV PrEP in 2012 (7).

The HPTN 076 study was a phase II clinical trial conducted by the HIV Prevention Trials Network to investigate the safety and acceptability of a RPV-LA injectable (1200 mg dosed in eight week intervals) for use in PrEP as a potential alternative to Truvada (8). HIV-uninfected women (n=136) were recruited across four cities for this study: (1) Bronx, New York, (2) Newark, New Jersey, (3) Cape Town, South Africa and (4) Harare Zimbabwe. We obtained whole blood from each participant for genomic DNA isolation to investigate the presence of genetic polymorphisms in drug metabolism enzymes that may impact RPV biotransformation. We have previously published that RPV is extensively oxidatively metabolized by the cytochromes P450, mainly CYP3A4 and CYP3A5, and RPV as well as its metabolites are primarily conjugated by the uridine diphosphate glucuronosyltransferases UGT1A1 and UGT1A4 (9). Taking this work a step further, we sequenced the coding regions of *CYP3A4*, *CYP3A5*, *UGT1A1* and *UGT1A4* in HPTN 076 participants using next-generation sequencing. Deleterious and potentially damaging variants were identified in the exonic regions of all four genes, however, *CYP3A5* genetic variants exhibited the greatest frequency (93%) overall. Moreover, loss of function *CYP3A5* alleles demonstrated a distinct decrease in the formation of RPV's primarily oxidative metabolite 2-hydroxymethyl RPV (M2). Further, genetic variants have been identified that could mitigate RPV metabolism and impact the occurrence of drug-mediated toxicities.

Materials and Methods

Reagents

RPV was provided through the National Institutes of Health AIDS Reagents Program. Metabolite M2 (2-hydroxymethyl RPV) and rilpivirine-d_6 (RPV-d_6) were synthesized and purchased from Toronto Research Chemicals (Toronto, ON).

Clinical samples

Whole blood and plasma was obtained from HIV-uninfected females (n=136) enrolled in the HIV Prevention Trials Network Study HPTN 076 across four study sites: Bronx Prevention Center CRS, Bronx, NY, USA (n=19); New Jersey Medical School Clinical Research Center CRS, Newark, NJ, USA (n=17); Emavundleni CRS, Cape Town, South Africa (n=48); Spilhaus Clinical Research Site, Harare, Zimbabwe (n=52) (8). The current analysis was approved by the Johns Hopkins Medicine IRB.

Genomic DNA isolation

Genomic DNA was isolated from 200 µL of whole blood using the QIAamp 96 DNA Blood Kit (Qiagen, Valencia, CA). Purified DNA was eluted using 200 µL of elution buffer.

Sample preparation for Next-generation sequencing

Samples were prepared following the TSCA library preparation guide using 250 ng of template DNA per reaction. Agencourt AMPure XP beads (Beckman Coulter, Inc., Brea, CA) were used for PCR clean-up and library normalization was performed according to the TSCA protocol. The final pooled DNA library (6 µL) was diluted in 594 µL HT1 buffer and spiked with 1% PhiX. One technical control was included per sample

batch and runs were sequenced using an Illumina MiSeq sequencing platform generating 150 bp paired-end reads.

Next-generation sequencing targeted enrichment design

Sequencing was performed using the Illumina TruSeq custom amplicon v1.5 kit (San Diego, CA). Custom probes targeting the exonic regions of *CYP3A4*, *CYP3A5*, *UGT1A1*, and *UGT1A4* were generated in silico using Illumina DesignStudio software. The chromosomal coordinates used were as follows: *CYP3A4* 7:99354583 – 7:99381811; *CYP3A5* 7:99245813 – 7:99277621; *UGT1A1* 2:234668919 – 2:234681945; *UGT1A4* 2:234627438 – 2:234681945. The final design included 120 amplicons.

Next-generation sequencing data analysis

Secondary analysis of the base calls and Phred-like quality score (Qscore) generated by Real Time Analysis software was performed using on-instrument MiSeq Reporter software. Reads were mapped to the GRCh37 (hg19) reference assembly using a banded Smith-Waterman algorithm and variant calling was carried out using the Genome Analysis Toolkit. Variant call format files were annotated using Illumina VariantStudio software. Raw variant calls were filtered applying a read depth threshold > 1500 bases per variant, a minimum base call Qscore of 30 (error rate of 1 in 1000), and an alternate variant frequency > 45%, followed by visual inspection using the Integrative Genome Viewer. Variants were ultimately cross-referenced with the National Center for Biotechnology Information database of Single Nucleotide Polymorphisms and variant alleles were assigned using the Karolinska Institutet's Human Cytochrome P450 Allele Nomenclature Database and PharmGKB (10, 11). The phenotypic consequence of

missense variants was assigned using SIFT (sorts intolerant from tolerant substitutions; J. Craig Venter Institute online tool) and PolyPhen (polymorphism phenotyping; Harvard University online tool) in silico prediction tools where amino acid substitutions were scored. A SIFT score < 0.05 was suggestive of a damaging amino acid substitution and > 0.05 a tolerated substitution, whereas a PolyPhen score > 0.908 was suggestive of a probably damaging, 0.447-0.908 a possibly damaging, or < 0.447 a benign amino acid substitution (12, 13).

Measurement of plasma concentrations of RPV and oxidative metabolite M2

Plasma RPV and metabolite M2 concentrations were determined using an ultra-high performance liquid chromatography-tandem mass spectrometry assay as previously published (9). In preparation for mass spectral analysis, RPV and M2 standard stock solutions were prepared at 50 µg/mL in 50:50 acetonitrile (ACN):H_2O and the internal standard (IS) RPV-d_6 at 100 ng/mL in ACN. RPV and M2 were diluted to a working solution at 16,000 ng/mL in ACN:H_2O and a standard curve was generated for each analyte using two-fold serial dilutions ranging from 16,000 ng/mL to 7.81 ng/mL. Calibration stocks for RPV and M2 were then prepared by diluting each standard curve 1:10 in blank human plasma for a total volume of 100 µL. Calibrants were vortexed and incubated at room temperature (RT) for 30 min. Analytes and HPTN 076 participant plasma samples (100 µL) were extracted by adding 200 µL ice-cold IS to precipitate plasma proteins. Calibrants and samples were vortexed, incubated at RT for 10 min and centrifuged for 10 min at 10,000 x *g* at 4°C. Supernatant (200 µL) was collected per sample and dried under vacuum. Calibrants and unknown samples were reconstituted in

200 µL methanol, vortexed, incubated at RT for 10 min prior to centrifugation for 5 min at 10,000 x *g* at 4°C. Resulting supernatants (150 µL) were collected for mass spectral analyses, injecting 10 µL per calibrant and unknown sample. In selected reaction monitoring mode, fragment ions were detected by positive ionization using the following transitions (Q1→Q3): RPV (*m/z* 367.1→195.2), M2 (*m/z* 383.0→222.0) and RPV-d_6 (*m/z* 373.1→230.0). Calibration curves were prepared and analyzed in duplicate for each analyte and 12-point standard curves (1600 ng/mL to 0.781 ng/mL) were calculated by taking the ratio of analyte peak area over internal standard and fit using a weighted ($1/y^2$) linear regression.

Statistical Analysis

Statistical analyses were performed using GraphPad Prism (San Diego, CA). Two-tailed unpaired *t* tests were performed and significance was denoted as follows: *, $p \leq 0{\cdot}05$; **, $p \leq 0{\cdot}01$; ***, $p \leq 0{\cdot}001$.

Results

Next-generation sequencing of HPTN 076 clinical samples

The HIV Prevention Trials Network study HPTN 076 recruited 136 HIV-uninfected female participants from the Bronx Prevention Center CRS, Bronx, NY (n=19), New Jersey Medical School Clinical Research Center CRS, Newark, NJ (n=17), Emavundleni CRS, Cape Town, South Africa (n=48) and Spilhaus Clinical Research Site, Harare, Zimbabwe (n=52). For this study, we obtained whole blood samples from all 136 of these participants to investigate the presence of genetic polymorphisms that may impact RPV metabolism. In order to test for the existence of genetic variants, we

designed a targeted assay to sequence the exonic regions of *CYP3A4*, *CYP3A5*, *UGT1A1*, and *UGT1A4*. Using this assay, we successfully sequenced 135 of the 136 participants (Bronx n=19, New Jersey n=17, Emavundleni n=48, Spilhaus n=51). One individual exhibited poor sequencing coverage (≤ 1000 base calls per read) and, therefore, was not included in these analyses.

Targeted sequencing of *CYP3A4*

A total of 12 single nucleotide variants (SNVs) for the *CYP3A4* mRNA transcript were detected in 56 participants (Bronx n=10, New Jersey n=6, Emavundleni n=17, Spilhaus n=23) of which carried one or more genetic variant for this gene (Table 1). Of the detected *CYP3A4* variants, four missense variants rs72552799 (R130Q), rs4986907 (R162Q, *CYP3A4*15A*), rs57409622 (R162W) and rs113667357 (Q200H), were detected in one (Bronx n=1), five (Bronx n=1, New Jersey n=1, Emavundleni n=1, Spilhaus n=3), one (Spilhaus n=1) and two (Emavundleni n=2) participants, respectively. Further, using in silico tools, two of the four observed missense variants, rs72552799 and rs57409622, were predicted to have a deleterious and damaging impact on protein function and were observed in our analyses to occur at a frequency of 1.5% (2/135 individuals).

								Bronx (n=19)		New Jersey (n=17)		Emavundleni (n=48)		Spilhaus (n=51)	
Region of CYP3A4	Position on Chr 7	dbSNP	Variant	Consequence	Star Allele	Amino Acid Mutation	Effect	*f* (n/19)	n	*f* (n/17)	n	*f* (n/49)	n	*f (n/50)*	n
3' UTR	99354661	rs28988606	c.*1095C>G	SNV	-	-	-	0.05 (Het)	1 (Het)	0.12 (Het)	2 (Het)	0.06 (Het)	3 (Het)	0.04 (Het)	2 (Het)
3' UTR	99355166	rs28371762	c.*590T>C	SNV	-	-	-	0.05 (Het)	1 (Het)	0	0	0	0	0	0
3' UTR	99355185	rs28988603	c.*571T>G	SNV	-	-	-	0.05 (Het)	1 (Het)	0.12 (Het)	2 (Het)	0.06 (Het)	3 (Het)	0.04 (Het)	2 (Het)
3' UTR	99355278	rs12721626	c.*478C>T	SNV	-	-	-	0.05 (Het)	1 (Het)	0	0	0	0	0	0
3' UTR	99355612	rs12721621	c.*144T>C	SNV	-	-	-	0.05 (Het)	1 (Het)	0	0	0	0	0	0
Exon 5	99367788	rs72552799	c.389G>A	SNV	-	R130Q	Deleterious (Predicted)	0.05 (Het)	1 (Het)	0	0	0	0	0	0
Exon 6	99367427	rs4986907	c.485G>A	SNV	CYP3A4*15A	R162Q	Tolerated (Predicted)	0.05 (Het)	1 (Het)	0.06 (Het)	1 (Het)	0.02 (Het)	1 (Het)	0.06 (Het)	3 (Het)
Exon 6	99367428	rs57409622	c.484C>T	SNV	-	R162W	Deleterious (Predicted)	0	0	0	0	0	0	0.02 (Het)	1 (Het)
Exon 7	99366047	rs113667357	c.600A>T	SNV	-	Q200H	Tolerated (Predicted)	0	0	0	0	0.04 (Het)	2 (Het)		
Intron 4	99367867	rs12721618	c.319-9G>C	SNV	-	-	-	0	0	0	0	0	0	0.04 (Het)	2 (Het)
Intron 11	99358615	rs12721620	c.1254-11C>T	SNV	-	-	-	0.42 (Het) 0.05 (Hom)	8 (Het) 1 (Hom)	0.24 (Het) 0.06 (Hom)	4 (Het) 1 (Hom)	0.31 (Het) 0.02 (Hom)	15 (Het) 1 (Hom)	0.30 (Het) 0.08 (Hom)	15 (Het) 4 (Hom)
Intron 11	99358693	rs77669275	c.1254-89G>A	SNV	-	-	-	0.05 (Het)	1 (Het)	0	0	0	0	0	0

Table 1. *CYP3A4* genetic variants detected in HPTN 076 participants. A total of 12 previously reported *CYP3A4* variants were detected in 56 HPTN 076 participants (Bronx n=10, New Jersey n=6, Emavundleni n=17, Spilhaus n=23) which carried one or more genetic variant for the coding DNA reference sequence NM_017460.5. The functional consequence of resulting amino acid mutations denoted as deleterious or tolerated were predicted using SIFT and PolyPhen in silico tools.

Targeted sequencing of *CYP3A5*

A total of 20 SNVs that may impact the protein-coding potential of the *CYP3A5* mRNA transcript were detected in 129 participants (Bronx n=15, New Jersey n=15, Emavundleni n=48, Spilhaus n=51) of which carried one or more genetic variant for this gene (Table 2). Of the detected *CYP3A5* variants, one splice variant rs776746 (*CYP3A5*3*), two missense variants rs142823108 (I149T) and rs145774441 (I276T) and one frameshift variant rs41303343 (*CYP3A5*7*, T346Y) were detected in 126 (Bronx n=14, New Jersey n=13, Emavundleni n=48, Spilhaus n=51), 2 (Spilhaus n=2), 2 (Spilhaus n=2) and 33 (Bronx n=0, New Jersey n=2, Emavundleni n=16, Spilhaus n=15) participants, respectively. Taken together, all four of these described variants were either predicted or have been determined by in vitro assay to be deleterious and have a damaging impact on protein function (14). Further, we observed these deleterious variants occurred at a frequency of 93.0% (126/135 individuals).

								Bronx (n=19)		New Jersey (n=17)		Emavundleni (n=48)		Spilhaus (n=51)	
Region of CYP3A5	Position on Chr 7	dbSNP	Variant	Consequence	Star Allele	Amino Acid Mutation	Effect	*f* (n/19)	n	*f* (n/17)	n	*f* (n/49)	n	*f (n/50)*	n
5' UTR	99277534	rs28371765	c.-15A>C	SNV	-	-	-	0.05 (Het)	1 (Het)	0	0	0.08 (Het)	4 (Het)	0	0
Intron 1	99273942	rs115267978	c.72-111C>T	SNV	-	-	-	0.05 (Het)	1 (Het)	0	0	0	0	0	0
Intron 3	99245914	rs776746	c.219-237G>A	SNV	CYP3A5*3	-	Non-Functional	0.53 (Het) 0.26 (Hom)	10 (Het) 5 (Hom)	0.29 (Het) 0.47 (Het)	5 (Het) 8 (Hom)	0.18 (Het) 0.82 (Hom)	9 (Het) 40 (Hom)	0.26 (Het) 0.74 (Hom)	13 (Het) 37 (Hom)
Intron 3	99270343	rs8175346	c.219-41C>A	SNV	-	-	-	0	0	0.06(Het)	1 (Het)	0	0	0	0
Intron 3	99270318	rs8175345	c.219-16C>T	SNV	-	-	-	0	0	0.12 (Het)	2 (Het)	0.16 (Het)	8 (Het)	0.24 (Het) 0.02 (Hom)	12 (Het) 1 (Hom)
Intron 4	99270165	rs28365074	c.318+38T>C	SNV	-	-	-	0	0	0.06(Het)	1 (Het)	0	0	0.08 (Het)	4 (Het)
Intron 4	99269401	rs6957030	c.318+802T>G	SNV	-	-	-	0.05 (Het)	1 (Het)	0.06(Het)	1 (Het)	0.04 (Het)	2 (Het)	0.1 (Het)	5 (Het)
Intron 4	99269397	rs6977165	c.318+806A>G	SNV	-	-	-	0.32 (Het)	6 (Het)	0.24 (Het)	4 (Het)	0.41 (Het) 0.02 (Hom)	20 (Het) 1 (Hom)	0.34 (Het) 0.04 (Hom)	17 (Het) 2 (Hom)
Intron 5	99264391	rs28383471	c.433-79C>G	SNV	-	-	-	0	0	0	0	0.04 (Het)	2 (Het)	0.02 (Het)	1 (Het)
Exon 6	99264299	rs142823108	c.446T>C	SNV	-	I149T	Deleterious (Predicted)	0	0	0	0	0	0	0.04 (Het)	2 (Het)
Intron 7	99261737	rs28969393	c.671-19T>C	SNV	-	-	-	0.05 (Het)	1 (Het)	0	0	0	0	0	0
Intron 8	99261446	rs28383473	c.798+145A>C	SNV	-	-	-	0	0	0.06(Het)	1 (Het)	0	0	0	0
Intron 8	99261380	rs28383474	c.798+211C>T	SNV	-	-	-	0.05 (Het)	1 (Het)	0	0	0	0	0	0
Intron 8	99260919	rs10256106	c.799-414G>C	SNV	-	-	-	0.12 (Het) 0.11 (Hom)	3 (Het) 1 (Hom)	0.24 (Het)	4 (Het)	0.16 (Het)	8 (Het)	0.2 (Het) 0.04 (Hom)	10 (Het) 2 (Hom)
Intron 8	99260734	rs28365086	c.799-229G>A	SNV	-	-	-	0.05 (Het)	1 (Het)	0.06(Het)	1 (Het)	0.02 (Het)	1 (Het)	0.1 (Het)	5 (Het)
Intron 9	99260477	rs145774441	c.827T>C	SNV	-	I276T	Deleterious (Predicted)	0	0	0	0	0	0	0.04 (Het)	2 (Het)
Intron 9	99260362	rs4646453	c.865+77G>T	SNV	-	-	-	0	0	0	0	0	0	0.28 (Het) 0.02 (Hom)	14 (Het) 1 (Hom)
Intron 9	99258317	rs59414422	c.866-35C>T	SNV	-	-	-	0	0	0	0	0.06 (Het)	3 (Het)	0	0
Exon 11	99250393	rs41303343	c.1035dupT	Insertion	CYP3A5*7	T346Y Frameshift	Non-Functional	0	0	0.12 (Het)	2 (Het)	0.33 (Het)	16 (Het)	0.26 (Het) 0.04 (Hom)	13 (Het) 2 (Hom)
Intron 12	99246026	rs28365069	c.1414-3T>C	SNV	-	-	-	0.05 (Het)	1 (Het)	0.06(Het)	1 (Het)	0.04 (Het)	2 (Het)	0.02 (Het)	1 (Het)

Table 2. *CYP3A5* genetic variants detected in HPTN 076 participants. A total of 20 previously reported *CYP3A5* genetic variants were detected in 129 HPTN 076 participants (Bronx n=15, New Jersey n=15, Emavundleni n=48, Spilhaus n=51) which carried one or more genetic variant for the coding DNA reference sequence NM_000777.3. The functional consequence of resulting amino acid mutations denoted as deleterious or tolerated were predicted using SIFT and PolyPhen in silico tools.

Targeted sequencing of *UGT1A1*

A total of 8 SNVs that may impact the protein-coding potential of the *UGT1A1* mRNA transcript were detected in 134 participants (Bronx n=19, New Jersey n=17, Emavundleni n=48, Spilhaus n=50) which carried one or more genetic variant for this gene (Table 3). Of the detected *UGT1A1* variants, one missense variant rs144217005 (V109A) and one upstream promoter insert variant rs34983651 (*UGT1A1*28*) were detected in one (Spilhaus n=1) and 22 (Bronx n=0, New Jersey n=3, Emavundleni n=10, Spilhaus n=9) participants, respectively. Of these variants, rs34983651 (*UGT1A1*28*) is well-studied to impair the transcription of *UGT1A1* thereby having a damaging impact on protein function and was observed with an overall frequency of 16.0% (22/135 individuals) in our analyses (15).

								Bronx (n=19)		New Jersey (n=17)		Emavundleni (n=48)		Spilhaus (n=51)	
Region of UGT1A1	Position on Chr 2	dbSNP	Variant	Consequence	Star Allele	Amino Acid Mutation	Effect	*f* (n/19)	n	*f* (n/17)	n	*f* (n/49)	n	*f (n/50)*	n
Upstream	234668828	rs34547608	c.-106T>C	SNV	-	-	-	0.11 (Het)	2 (Het)	0.06 (Het)	1 (Het)	0.29 (Het)	14 (Het)	0.24 (Het) 0.02 (Hom)	12 (Het) 1 (Hom)
Upstream	234668879	rs34983651	$(TA)_7$	Insertion	UGT1A1*28	-	Low-Expression	0	0	0.12 (Het) 0.06 (Hom)	2 (Het) 1 (Hom)	0.14 (Het) 0.06 (Hom)	7 (Het) 3 (Hom)	0.16 (Het) 0.02 (Hom)	8 (Het) 1 (Hom)
Exon 1	234669259	rs144217005	c.326T>C	SNV	-	V109A	Tolerated (Predicted)	0	0	0	0	0	0	0.02 (Het)	1 (Het)
Intron 1	234675662	rs182710200	c.865-18T>A	SNV	-	-	-	0	0	0	0	0.02 (Het)	1 (Het)	0	0
Intron 2	234675829	rs34650714	c.996+18C>T	SNV	-	-	-	0.16 (Het)	3 (Het)	0.06 (Het)	1 (Het)	0.27 (Het) 0.02 (Hom)	13 (Het) 1 (Hom)	0.3 (Het) 0.04 (Hom)	15 (Het) 2 (Hom)
3' UTR	234681544	rs1042640	c.*339G>C	SNV	-	-	-	0.84 (Het) 0.05 (Hom)	16 (Het) 1 (Hom)	0.88 (Het) 0.06 (Hom)	15 (Het) 1 (Hom)	0.67 (Het) 0.29 (Hom)	33 (Het) 14 (Hom)	0.88 (Het) 0.12 (Hom)	44 (Het) 6 (Hom)
3' UTR	234681550	rs112908387	c.*345C>T	SNV	-	-	-	0	0	0	0	0.04 (Het)	2 (Het)	0	0
3' UTR	234681645	rs8330	c.*440G>C	SNV	-	-	-	0.32 (Het) 0.47 (Hom)	6 (Het) 9 (Hom)	0.35 (Het) 0.47 9Hom)	6 (Het) 8 (Hom)	0.43 (Het) 0.39 (Hom)	21 (Het) 19 (Hom)	0.56 (Het) 0.30 (Hom)	28 (Het) 15(Hom)

Table 3. *UGT1A1* genetic variants detected in HPTN 076 participants. A total of 8 previously reported *UGT1A1* variants were detected in 134 HPTN 076 participants (Bronx n=19, New Jersey n=17, Emavundleni n=48, Spilhaus n=50) which carried one or more genetic variant for the coding DNA reference sequence NM_000463.2. The functional consequence of resulting amino acid mutations denoted as deleterious or tolerated were predicted using SIFT and PolyPhen in silico tools.

Targeted sequencing of *UGT1A4*

A total of 20 SNVs that may impact the protein-coding potential of the *UGT1A4* mRNA transcript were detected in 135 participants (Bronx n=19, New Jersey n=17, Emavundleni n=48, Spilhaus n=51) which carried one or more genetic variant for this gene (Table 2). Of the detected *UGT1A4* variants, eight missense variants rs3892221 (*UGT1A4**4, R11W), rs6755571 (*UGT1A4**2, P24T), rs2011425 (*UGT1A4**3b, L48V), rs141408391 (A58V), rs201935850 (K73N) rs146073833 (G158R), rs45540231 (I176F) and rs138822211 (I223L) were detected in seven (Bronx n=0, New Jersey n=2, Emavundleni n=4, Spilhaus n=1), four (Bronx n=1, New Jersey n=1, Emavundleni n=1, Spilhaus n=1), 21 (Bronx n=5, New Jersey n=3, Emavundleni n=5, Spilhaus n=8), one (Spilhaus n=1), one (Spilhaus n=1), seven (Bronx n=1, New Jersey n=1, Emavundleni n=3, Spilhaus n=2), 13 (Bronx n=2, New Jersey n=0, Emavundleni n=13, Spilhaus n=12), and three (New Jersey n=1, Spilhaus n=2) participants, respectively. Of these detected missense variants, only one variant, rs146073833, was predicted be deleterious and have a damaging impact on protein function. This variant was observed in our analyses with a frequency of 5.0% (7/135 individuals)

								Bronx (n=19)		New Jersey (n=17)		Emavundleni (n=48)		Spilhaus (n=51)	
Region of UGT1A4	Position on Chr 2	dbSNP	Variant	Consequence	Star Allele	Amino Acid Mutation	Effect	f (n/19)	n	f (n/17)	n	f (n/49)	n	f (n/50)	n
Exon 1	234627497	rs3892221	c.31C>T	SNV	UGT1A4*4	R11W	Tolerated (Predicted)	0	0	0.12 (Het)	2 (Het)	0.08 (Het)	4 (Het)	0.02 (Het)	1 (Het)
Exon 1	234627536	rs6755571	c.70C>A	SNV	UGT1A4*2	P24T	Tolerated (Predicted)	0.05 (Het)	1 (Het)	0.06 (Het)	1 (Het)	0.02 (Het)	1 (Het)	0.02 (Het)	1 (Het)
Exon 1	234627608	rs2011425	c.142T>G	SNV	UGT1A4*3b	L48V	Tolerated (Predicted)	0.21 (Het)	4 (Het)	0.12 (Het)	2 (Het)	0.08 (Het)	4 (Het)	0.14 (Het)	7 (Het)
Exon 1	234627639	rs141408391	c.173C>T	SNV	-	A58V	Tolerated (Predicted)	0	0	0	0	0	0	0.02 (Het)	1 (Het)
Exon 1	234627685	rs201935850	c.219A>C	SNV	-	K73N	Tolerated (Predicted)	0	0	0	0	0	0	0.02 (Het)	1 (Het)
Exon 1	234627938	rs146073833	c.472G>A	SNV	-	G158R	Deleterious (Predicted)	0.05 (Het)	1 (Het)	0.06 (Het)	1 (Het)	0.06 (Het)	3 (Het)	0.04 (Het)	2 (Het)
Exon 1	234627992	rs45540231	c.526A>T	SNV	-	I176F	Tolerated (Predicted)	0.11 (Het)	2 (Het)	0	0	0.27 (Het)	13 (Het)	0.22 (Het) 0.02 (Hom)	11 (Het) 1 (Hom)
Exon 1	234628133	rs138822211	c.667A>C	SNV	-	I223L	Tolerated (Predicted)	0	0	0.06 (Het)	1 (Het)	0	0	0.04 (Het)	2 (Het)
Intron 1	234628376	rs2011219	c.867+43C>T	SNV	-	-	-	0.21 9Het)	4 (Het)	0.06 (Het)	1 (Het)	0.04 (Het)	2 (Het)	0.06 (Het)	3 (Het)
Intron 1	234637944	rs140541315	c.867+9611G>A	SNV	-	-	-	0	0	0	0	0	0	0.02 (Het)	1 (Het)
Intron 1	234656517	rs12466997	c.868-19163T>C	SNV	-	-	-	0	0	0	0	0.16 (Het) 0.06 (Hom)	8 (Het) 3 (Hom)	0.38 (Het) 0.08 (Hom)	19 (Het) 4 (Hom)
Intron 1	234668828	rs34547608	c.868-6852T>C	SNV	-	-	-	0.11 (Het)	2 (Het)	0.06 (Het)	1 (Het)	0.29 (Het)	14 (Het)	0.24 (Het) 0.02 (Hom)	12 (Het) 1 (Hom)
Intron 1	234668879	rs34983651	c.868-6801_868-6800insAT	Insertion	-	-	-	0	0	0.12 (Het) 0.06 (Hom)	2 (Het) 1 (Hom)	0.14 (Het) 0.06 (Hom)	7 (Het) 3 (Hom)	0.16 (Het) 0.02 (Hom)	8 (Het) 1 (Hom)
Intron 1	234669259	rs144217005	c.868-6421T>C	SNV	-	-	-	0	0	0	0	0	0	0.02 (Het)	1 (Het)
Intron 1	234669886	rs17868341	c.868-5794C>T	SNV	-	-	-	0.05 (Het)	1 (Het)	0	0	0	0	0	0
Intron 1	234675662	rs182710200	c.868-18T>A	SNV	-	-	-	0	0	0	0	0.02 (Het)	1 (Het)	0	0
Intron 2	234675829	rs34650714	c.999+18C>T	SNV	-	-	-	0.16 (Het)	3 (Het)	0.06 (Het)	1 (Het)	0.27 (Het) 0.02 (Hom)	13 (Het) 1 (Hom)	0.3 (Het) 0.04 (Hom)	15 (Het) 2 (Hom)
3' UTR	234681544	rs1042640	*339G>C	SNV	-	-	-	0.84 (Het) 0.05 (Hom)	16 (Het) 1 (Hom)	0.88 (Het) 0.06 (Hom)	15 (Het) 1 (Hom)	0.67 (Het) 0.29 (Hom)	33 (Het) 14 (Hom)	0.88 (Het) 0.12 (Hom)	44 (Het) 6 (Hom)
3' UTR	234681550	rs112908387	c.*345C>T	SNV	-	-	-	0	0	0	0	0.04 (Het)	2 (Het)	0	0
3' UTR	234681645	rs8330	c.*440G>C	SNV	-	-	-	0.32 (Het) 0.47 (Hom)	6 (Het) 9 (Hom)	0.35 (Het) 0.47 (Hom)	6 (Het) 8 (Hom)	0.43 (Het) 0.39 (Hom)	21 (Het) 19 (Hom)	0.56 (Het) 0.30 (Hom)	28 (Het) 15 (Hom)

Table 4. *UGT1A4* genetic variants detected in HPTN 076 participants. A total of 20 previously reported *UGT1A4* variants were detected in 135 HPTN 076 participants (Bronx n=19, New Jersey n=17, Emavundleni n=48, Spilhaus n=51) which carried one or more genetic variant for the coding DNA reference sequence NM_007120.2. The functional consequence of resulting amino acid mutations denoted as deleterious or tolerated were predicted using SIFT and PolyPhen in silico tools.

Quantitation of RPV and metabolite M2 in HPTN 076 participants

Although the primary aim of the HPTN 076 study was to investigate the safety and acceptability of a RPV-LA injectable, participants were dosed 25 mg RPV once-daily for four weeks to evaluate potential toxicities prior to initiating intramuscular dosing of the nanosuspension (8). We utilized ultra-high performance liquid chromatography-tandem mass spectrometry to quantitate RPV and its primary oxidative metabolite in 83 plasma samples of HPTN 076 participants (Bronx n=12, New Jersey n=11, Emavundleni n=25, Spilhaus n=35). Of the 83 samples analyzed, five participants had RPV plasma levels below the lower limit of quantitation (LLOQ) and, in addition, two separate participants had drug levels below the limit of detection (LLOD). That being said, for the remaining 76 participants, the mean RPV plasma level was 77.77 ng/mL ± 57.93 ng/mL and the distribution of RPV plasma levels across study sites is shown in Figure 1. The oxidative RPV metabolite M2 was detected in 58 of the 83 samples analyzed, with 17 participants having M2 levels below the LLOQ, and eight participants with M2 levels below the LLOD. The mean M2 plasma level was 3.04 ng/mL ± 1.60 ng/mL and the distribution of metabolite plasma levels across study sites is shown in Figure 2.

RPV is primarily metabolized by the cytochrome P450 isozymes CYP3A4 and CYP3A5. Our sequencing analyses of HPTN 076 participants demonstrated *CYP3A5* exhibited the greatest frequency of potentially deleterious genetic variants. Therefore, we wanted to test if CYP3A5 loss of function genetic variants correlated with decreased M2 formation. A statistically significant difference in RPV to metabolite M2 plasma ratios was not observed across *CYP3A5* alleles (0, homozygous dysfunctional allele; 1,

heterozygous dysfunctional; 2, homozygous wild type) (Figure 3). However, there was a distinct stepwise trend, with carriers of homozygous dysfunctional *CYP3A5* alleles having the highest ratio of RPV to M2 plasma levels (mean ratio = 35.47), followed by heterozygous dysfunctional *CYP3A5* alleles (mean ratio =30.31) and then homozygous wild type *CYPA5* alleles (mean ratio = 24.60).

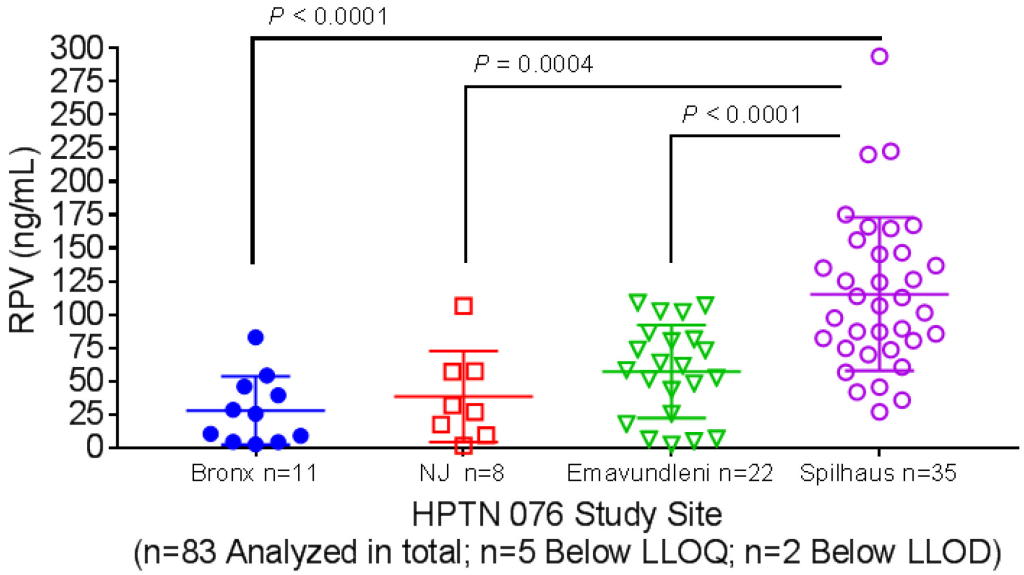

Figure 1. HPTN 076 participant RPV plasma concentrations dosed 25 mg once-daily for four weeks. RPV plasma concentrations were determined using an ultra-high performance liquid chromatography-tandem mass spectrometry assay as previously published (9). HPTN 076 participant plasma samples (100 µL) were extracted for drug by adding 200 µL ice-cold 100 ng/mL RPV-d_6. Supernatant (200 µL) was collected per sample and dried under vacuum. Dried samples were reconstituted in 200 µL methanol and 10 µL per sample was injected for analysis. Fragment ions were detected in selected reaction monitoring mode using the following transitions (Q1→Q3): RPV (*m/z* 367.1→195.2) and RPV-d_6 (*m/z* 373.1→230.0).

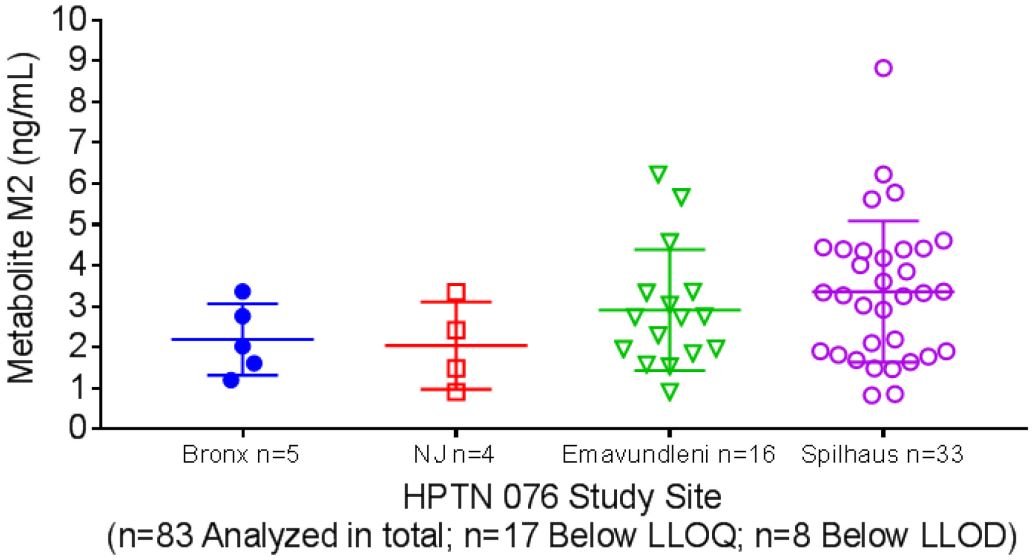

Figure 2. HPTN 076 participant metabolite M2 plasma concentrations dosed 25 mg RPV once-daily for four weeks. M2 plasma concentrations were determined using an ultra-high performance liquid chromatography-tandem mass spectrometry assay as previously published (9). HPTN 076 participant plasma samples (100 µL) were extracted for RPV metabolites by adding 200 µL ice-cold 100 ng/mL RPV-d_6. Supernatant (200 µL) was collected per sample and dried under vacuum. Dried samples were reconstituted in 200 µL methanol and 10 µL per sample was injected for analysis. Fragment ions were detected in selected reaction monitoring mode using the following transitions (Q1→Q3): M2 (*m/z* 383.0→222.0) and RPV-d_6 (*m/z* 373.1→230.0). No significance difference was observed across HPTN 076 study sites.

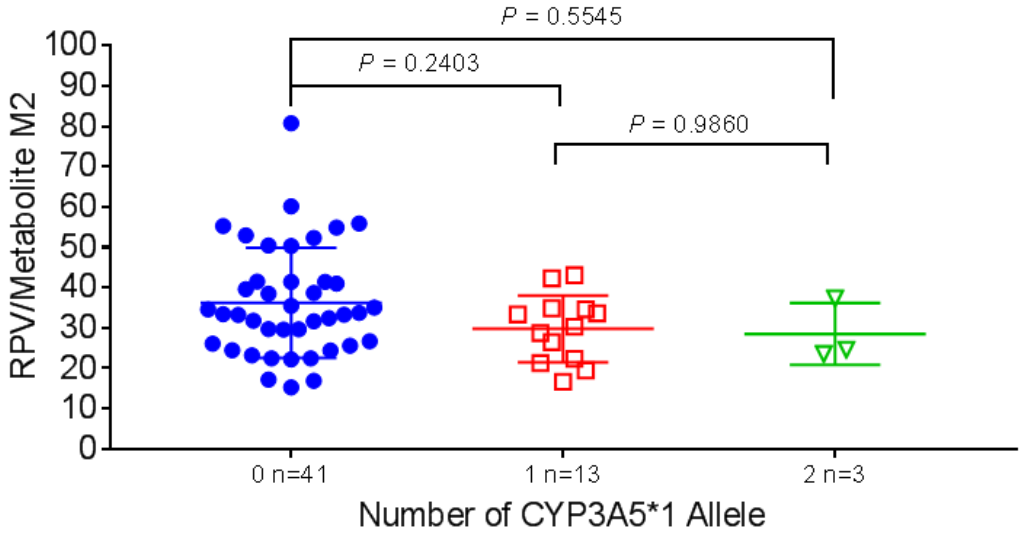

Figure 3. Correlation of RPV/metabolite M2 plasma levels to CYP3A5 genotype of HPTN 076 participants. HPTN 076 participants were grouped by *CYP3A5* genotype: 0, homozygous dysfunctional, 1 heterozygous dysfunctional, 2 homozygous wild type, where *CYP3A5**1 is the wild type allele. A ratio of RPV to metabolite M2 plasma levels were then plotted against genotype for each participant.

Discussion

Through previous work characterizing the human biotransformation of RPV, we identified *CYP3A4*, *CYP3A5*, *UGT1A1*, and *UGT1A4* as candidates for examination in this retrospective clinical study (9). In genomic DNA isolated from participants of the HPTN 076 phase II clinical trial, we detected 60 previously reported variants in the genes encoding these drug metabolizing enzymes. While we did not validate these variants in parallel using Sanger sequencing, the coverage threshold implemented in our analyses was in line with the American College of Medical Genetics and Genomics clinical laboratory standards for next-generation sequencing, increasing the confidence in the variants called (16).

We detected variants in all four drug metabolizing enzymes that could negatively impact function at the protein level, however, *CYP3A5* exhibited the greatest frequency of potentially damaging and/or deleterious genetic variants. Of the detected *CYP3A5* variants, the non-functional splice variant *CYP3A5**3 was observed at a frequency of 93.0 %. This variant results from a 6986A>G mutation, which alters the reading frame causing a premature termination codon and is the most commonly occurring non-functional allele of *CYP3A5* (14). In European American populations the *CYP3A5*3* allele frequency is estimated to be 82 to 95% in contrast to African American populations with an allele frequency of 33% (17-21). The ethnicities of all HPTN 076 participants were blinded for this study, so it is problematic to make conclusions about ethnic-specific allele frequencies. That being said, of all individuals sequenced, Zimbabwean participants from this study may exhibit the most homogenous population and we observed 72.5% were

homozygous for *CYP3A5*3*. This is in strong agreement with a recent publication estimating Zimbabweans exhibit a *CYP3A5*3* frequency of 77.6%, thereby bolstering our confidence in the sequencing analyses performed in this study (22).

In order to put these findings within the context of RPV metabolism, we quantitated drug and metabolite levels in plasma samples obtained from HPTN 076 participants taking a once-daily dose of RPV for a phase I clinical study. Adherence, however, is a confounding issue for HIV PrEP studies and this was apparent in our analyses as a large variability was observed in parent drug levels. Adherence aside, loss of function CYP3A5 alleles did appear to decrease RPV metabolism albeit not significantly compared to wild type allele. We previously observed that the primary oxidative metabolite of RPV, M2, can range from 1 to 2% of total metabolites formed (9). Further, the potential reactivity of this metabolite has not yet been characterized. Therefore, it is imperative that these analyses be extended to plasma samples obtained from HPTN 076 patients administered the 1200 mg RPV-LA injectable. This will enable a more powerful genotype-phenotype analysis as compliance will no longer be a limiting covariate.

In conclusion, we detected deleterious and potentially damaging genetic variants in the genes encoding the drug metabolizing enzymes that contribute to RPV metabolism. Further investigation, however, is required in order to determine if these variants indeed cause a genetic basis for inter-individual variation observed in RPV drug levels.

References

1. Janssen PA, Lewi PJ, Arnold E, Daeyaert F, de Jonge M, Heeres J, et al. In search of a novel anti-HIV drug: multidisciplinary coordination in the discovery of 4-[[4-[[4-[(1E)-2-cyanoethenyl]-2,6-dimethylphenyl]amino]-2- pyrimidinyl]amino]benzonitrile (R278474, rilpivirine). J Med Chem. 2005;48(6):1901-9.

2. Baert L, van 't Klooster G, Dries W, Francois M, Wouters A, Basstanie E, et al. Development of a long-acting injectable formulation with nanoparticles of rilpivirine (TMC278) for HIV treatment. Eur J Pharm Biopharm. 2009;72(3):502-8.

3. WHO Expands Recommendation on Oral Preexposure Prophylaxis of HIV Infection (PrEP) World Health Organization; [November 2015; cited]; Available from: http://apps.who.int/iris/bitstream/10665/197906/1/WHO_HIV_2015.48_eng.pdf?ua=1.

4. Abdool Karim Q, Abdool Karim SS, Frohlich JA, Grobler AC, Baxter C, Mansoor LE, et al. Effectiveness and safety of tenofovir gel, an antiretroviral microbicide, for the prevention of HIV infection in women. Science. 2010;329(5996):1168-74. PMCID: 3001187.

5. Grant RM, Lama JR, Anderson PL, McMahan V, Liu AY, Vargas L, et al. Preexposure chemoprophylaxis for HIV prevention in men who have sex with men. N Engl J Med. 2010;363(27):2587-99. PMCID: 3079639.

6. Baeten JM, Donnell D, Ndase P, Mugo NR, Campbell JD, Wangisi J, et al. Antiretroviral prophylaxis for HIV prevention in heterosexual men and women. N Engl J Med. 2012;367(5):399-410. PMCID: 3770474.

7. U. S. Food and Drug Administration Approves Gilead's Truvada for Reducing the Risk of Acquiring HIV. Foster, CA: Gilead Sciences, Inc.; [July 2012; cited]; Available from: http://www.gilead.com/news/press-releases/2012/7/us-food-and-drug-administration-approves-gileads-truvada-for-reducing-the-risk-of-acquiring-hiv.

8. HPTN 076 Phase II Safety and Acceptability of an Investigational Injectable Product, TMC278 LA, for Pre-Exposure Prophylaxis (PrEP). [April 4, 2016; cited]; Available from: https://www.hptn.org/sites/default/files/2016-05/HPTN%20076%20Protocol%20Final%20v3.0,%204Apr2016.pdf.

9. Lade JM, Avery LB, Bumpus NN. Human biotransformation of the nonnucleoside reverse transcriptase inhibitor rilpivirine and a cross-species metabolism comparison. Antimicrob Agents Chemother. 2013;57(10):5067-79. PMCID: 3811466.

10. Whirl-Carrillo M, McDonagh EM, Hebert JM, Gong L, Sangkuhl K, Thorn CF, et al. Pharmacogenomics knowledge for personalized medicine. Clin Pharmacol Ther. 2012;92(4):414-7. PMCID: 3660037.

11. ; [cited]; Available from: http://www.cypalleles.ki.se/.

12. Ng PC, Henikoff S. Predicting deleterious amino acid substitutions. Genome Res. 2001;11(5):863-74. PMCID: 311071.

13. Ramensky V, Bork P, Sunyaev S. Human non-synonymous SNPs: server and survey. Nucleic Acids Res. 2002;30(17):3894-900. PMCID: 137415.

14. Lamba J, Hebert JM, Schuetz EG, Klein TE, Altman RB. PharmGKB summary: very important pharmacogene information for CYP3A5. Pharmacogenet Genomics. 2012;22(7):555-8. PMCID: 3738061.

15. Rauchschwalbe SK, Zuhlsdorf MT, Schuhly U, Kuhlmann J. Predicting the risk of sporadic elevated bilirubin levels and diagnosing Gilbert's syndrome by genotyping UGT1A1*28 promoter polymorphism. Int J Clin Pharmacol Ther. 2002;40(6):233-40.

16. Rehm HL, Bale SJ, Bayrak-Toydemir P, Berg JS, Brown KK, Deignan JL, et al. ACMG clinical laboratory standards for next-generation sequencing. Genet Med. 2013;15(9):733-47. PMCID: 4098820.

17. Kuehl P, Zhang J, Lin Y, Lamba J, Assem M, Schuetz J, et al. Sequence diversity in CYP3A promoters and characterization of the genetic basis of polymorphic CYP3A5 expression. Nat Genet. 2001;27(4):383-91.

18. Lee SJ, Usmani KA, Chanas B, Ghanayem B, Xi T, Hodgson E, et al. Genetic findings and functional studies of human CYP3A5 single nucleotide polymorphisms in different ethnic groups. Pharmacogenetics. 2003;13(8):461-72.

19. Thompson EE, Kuttab-Boulos H, Witonsky D, Yang L, Roe BA, Di Rienzo A. CYP3A variation and the evolution of salt-sensitivity variants. Am J Hum Genet. 2004;75(6):1059-69. PMCID: 1182141.

20. Kurose K, Sugiyama E, Saito Y. Population differences in major functional polymorphisms of pharmacokinetics/pharmacodynamics-related genes in Eastern Asians and Europeans: implications in the clinical trials for novel drug development. Drug Metab Pharmacokinet. 2012;27(1):9-54.

21. Blanco JG, Edick MJ, Hancock ML, Winick NJ, Dervieux T, Amylon MD, et al. Genetic polymorphisms in CYP3A5, CYP3A4 and NQO1 in children who developed therapy-related myeloid malignancies. Pharmacogenetics. 2002;12(8):605-11.

22. Roy JN, Lajoie J, Zijenah LS, Barama A, Poirier C, Ward BJ, et al. CYP3A5 genetic polymorphisms in different ethnic populations. Drug Metab Dispos. 2005;33(7):884-7.

Chapter 4: Structure-Activity Relationship of Efavirenz-Mediated Activation of the Pregnane X Receptor

Abstract

Efavirenz (EFV) is a non-nucleoside reverse transcriptase inhibitor FDA-approved for HIV maintenance therapy in 1998 and to date remains to be the most widely prescribed antiretroviral. EFV is extensively metabolized by the cytochromes P450s and has been observed to autoinduce its own metabolism with chronic administration. Previous reports have demonstrated EFV autoinduction is mediated chiefly through the ligand-activated nuclear receptor pregnane X receptor (NR1I2; PXR). In this study, we investigated the structure-activity relationship of the anti-HIV drug EFV and PXR in an effort to identify potential structural moieties that confer PXR activation. We utilized a panel of sixteen EFV analogs ranging 223 Da to 423 Da in size in addition to its primary oxidative metabolite of EFV, 8-hydroxy efavirenz (8-OHEFV), to test for PXR activation through target gene mRNA modulation in primary mouse hepatocytes, luciferase reporter assays in transiently transfected HepG2 cells and a cell-free competitive binding assay. We observed that analog 10 the smallest compound 223 Da in size tested and 8-OHEFV were unable to activate PXR. However, unlike analog 10, 8-OHEFV was able to competitively bind to the PXR-ligand-binding domain (PXR-LBD). Further, through molecular docking simulations we observed the polar hydroxyl functional group of 8-OHEFV causes a potentially destabilizing interaction in a hydrophobic pocket of the PXR-LBD formed by residues Phe288, Trp299 and Tyr306. From these studies, we observed that ligand size and polarity are key determinants in conferring PXR agonism.

Introduction

Efavirenz (EFV; Figure 1) is a first-generation non-nucleoside reverse transcriptase inhibitor FDA-approved for HIV maintenance therapy in 1998 and to date remains to be the most widely prescribed antiretroviral. This is in part due to the World Health Organization guidelines that recommend EFV be dosed as a third agent to treatment-naïve HIV-infected adults in combination with two nucleoside/nucleotide reverse transcriptase inhibitors tenofovir disoproxil fumarate and emtricitabine (1). EFV undergoes first-pass metabolism and is well-established to be extensively metabolized by heme-containing monooxygenases the cytochromes P450, mainly CYP2B6 and CYP3A4 (2). Further, EFV has been observed to autoinduce its own metabolism with chronic administration and thereby exhibits a high incidence rate of drug-drug interactions upon co-administration with other cytochrome P450 substrates (3). In line with this, substantial evidence has mounted demonstrating EFV autoinduction is mediated chiefly through the ligand-activated nuclear receptor pregnane X receptor (NR1I2; PXR) (4-6).

PXR is part of an extensive superfamily of transcription factors that contribute to the regulation of cellular growth, development and homeostasis through either gene activation or repression (7). Nuclear receptors in general exhibit a modular structure organized into five to six domains and, of these domains, the most conserved regions are the DNA-binding domain containing two zinc fingers and the ligand-binding domain which serves as the docking site for a ligand (8). Moreover, the coordinated actions of these domains culminate into the modulation of target gene expression. Under basal conditions, PXR is sequestered in the cytosol by the chaperones cytoplasmic CAR

retention protein and heat shock protein 90 (9, 10). Upon ligand binding, PXR dissociates from the chaperone protein complex and translocates to the nucleus where it then heterodimerizes with 9-cis retinoic acid receptor (RXR) and binds to response elements in the promoter regions of target genes to facilitate transcription (11). Although not an exhaustive list, PXR/RXR binding sites have been detected in the promoter regions of drug metabolizing enzymes mainly the cytochrome P450 subfamilies *CYP1A*, *CYP2A*, *CYP2B*, *CYP2C*, *CYP3A*, *CYP4F12*, carboxyesterases *CES1* and *CES2*, and the uridine diphosphate glucuronosyltransferase isozymes *UGT1A1*, *UGT1A3*, *UGT1A6*, as well as the drug transporter multidrug resistance gene *MDR1* (12-17).

Transcriptional activation, however, is spurred by ligand binding and to that end PXR requires broad substrate specificity in order to function as a "xenobiotic sensor." PXR's ligand-binding pocket is large, approximately 1150 $Å^3$ in size, relatively hydrophobic in nature and highly flexible and thus can accommodate an array of xenobiotics (18). In this study, we aimed to investigate the structure-activity relationship of the anti-HIV drug EFV and PXR in an effort to identify potential pharmacophores that regulate PXR activation. We utilized a panel of sixteen EFV analogs ranging 223 Da to 423 Da in size in addition to the primary oxidative metabolite of EFV, 8-hydroxy efavirenz (8-OHEFV), to test for PXR activation through target gene mRNA modulation in primary mouse hepatocytes, luciferase reporter assays in transiently transfected HepG2 cells and a cell-free competitive binding assay. Supplementary to these *in vitro* studies, we also performed molecular docking simulations to investigate the interactions of all of the compounds in our study with the PXR ligand-binding domain to aid in visualizing

potential ligand-receptor interactions. From these studies, we observed that ligand size and polarity are key determinants in conferring PXR agonism.

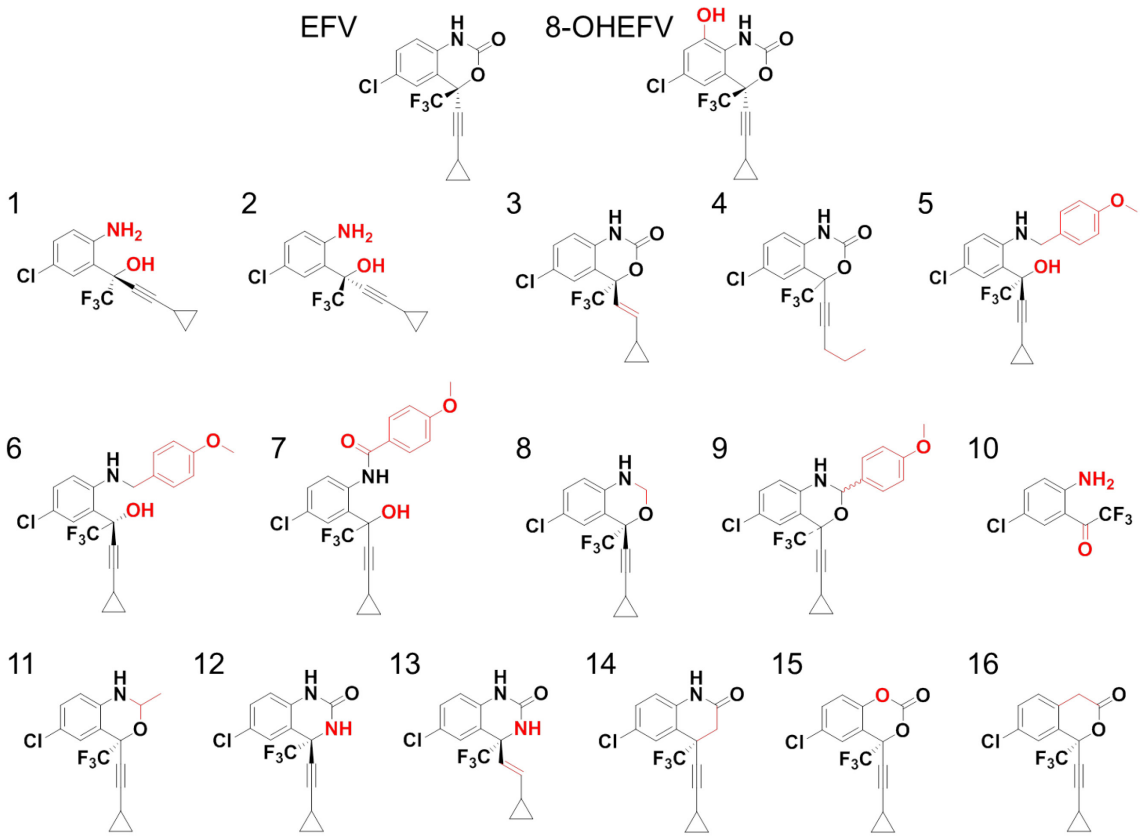

Figure 1. Structural comparison of EFV, 8-OHEFV and sixteen EFV analogs. EFV is a first generation non-nucleoside reverse transcriptase inhibitor that has been previously demonstrated to activate mouse and human PXR. In this work, we aimed to test the activity of mouse and human PXR towards EFV's primary oxidative metabolite 8-OHEFV and sixteen EFV analogs spanning from 223 to 423 Da in size. Atoms that diverge from the chemical structure of EFV are highlighted in red.

Materials and Methods

Reagents

Pregnenolone 16α-carbonitrile (PCN), rifampicin (RIF) and SR12813 were purchased from Sigma-Aldrich (St. Louis, MO). EFV, 8-OHEFV and all EFV analogs were synthesized by and purchased from Toronto Research Chemicals (Toronto, ON).

Isolation of primary mouse hepatocytes and drug treatments

Hepatocytes were isolated from 9-13 week-old male C57BL/6J (wild type, WT) mice from Jackson Laboratories (Bar Harbor, ME) as well as from 9-13 week-old male humanized pregnane X receptor (hPXR) and pregnane X receptor knockout ($PXR^{-/-}$) mice bred on a C57BL/6J background were purchased from Taconic Biosciences (Hudson, NY). Primary mouse hepatocytes were isolated using retrograde liver perfusion with 25 mL 0.5 mM EGTA (Amresco LLC, Solon, OH) prepared in 1X PBS (Thermo Fisher Scientific, Waltham, MA) at 5 mL/min, followed by 25 mL 1X PBS at 5 mL/min, and lastly 20 mL of liver digest medium (Thermo Fisher Scientific) supplemented with 0.15 mg/mL collagenase (Sigma-Aldrich) at 2 mL/min. Following perfusion, livers were removed and cells were gently dissociated in 15 mL of ice-cold hepatocyte wash medium (Thermo Fisher Scientific) using a cell scraper and filtered through a 70 μm nylon mesh cell strainer. Hepatocytes were then pelleted at 50 x *g* for 5 min at 4°C and washed twice with 10 mL hepatocyte wash medium. Cells were resuspended in 25 mL Williams E medium (Thermo Fisher Scientific) with 20 mL percoll (Sigma-Aldrich; 1 part 10X HBSS and 9 parts percoll) and inverted six times prior to pelleting at 300 x *g* for 10 min at 4°C. Hepatocytes were washed with 10 mL Williams E medium, pelleted at 50 x *g* for

5 min at 4°C, and resuspended in 10 mL Williams E medium supplemented with 10% fetal bovine serum (Thermo Fisher Scientific), 1% L-glutamine (Thermo Fisher Scientific), and 1% penicillin-streptomycin (Sigma-Aldrich). Hepatocytes were plated in six-well collagen-coated plates (Corning, Tewksbury, MA) at a density of 2.4 x 10^5 cells per well. Cells were incubated overnight at 37°C and 5% CO_2 prior to replacing the cell culture medium with fresh Williams E medium containing 10% fetal bovine serum, 1% L-glutamine, and 1% penicillin-streptomycin for drug treatments. Hepatocytes were treated with either DMSO (0.1%) vehicle or 10 μM drug for RNA isolation over a range of time points. For 48 h and 72 h drug treatments, cell culture medium was replaced every 24 h and hepatocytes were retreated with DMSO or drug. A total of four independent experiments were performed for hepatocytes isolated from WT, hPXR and $PXR^{-/-}$ mice.

RNA isolation and quantitative real-time PCR (qPCR)

RNA was prepared from primary mouse hepatocytes using TRIzol (Thermo Fisher Scientific) following the manufacturer's instructions for cells grown in a monolayer. Total RNA (1 μg) was reverse transcribed using Maxima First Strand cDNA Synthesis Kit (Thermo Fisher Scientific). The following primers were used for qPCR: Cyp3a11 forward 5'-ATAGAGCTTTGCTGTCCCCC-3' and reverse 5'-CGGCTTTCCTTCATTCTGTC-3'; Gapdh forward 5'-GAAGGCCGGGGCCCACTTGA-3' and reverse 5'-TCTCCAGGCGGCACGTCAGA-3'. A Gapdh PCR product was generated from mouse hepatocyte RNA using conventional PCR and ligated into CloneJET PCR cloning kit for subcloning (Thermo

Fisher Scientific). Serial dilutions of the resulting Gapdh plasmid were used to generate a standard curve for the quantitation of mRNA levels using Maxima SYBR Green qPCR Master Mix (Thermo Fisher Scientific). Gapdh served as the housekeeping gene for mRNA level normalization. The following qPCR cycling reactions were performed: denaturation of dsDNA for 10 min at 95°C proceeded by 40 cycles of denaturation for 15 sec at 95°C, annealing for 30 sec at 60°C, and extension for 30 sec at 72°C. Resulting Cyp3a11 copy numbers were normalized by Gapdh for each treatment and data was reported as fold change from DMSO control for each time point.

Transient transfection and dual-luciferase reporter gene assay

HepG2 human hepatocellular carcinoma cells (American Type Culture Collection, Manassas, VA) were cultured in T-75 flasks in high glucose Dulbecco's Modified Eagle Medium (DMEM; American Type Culture Collection) supplemented with 10% fetal bovine serum and 1% penicillin and streptomycin. Cells were maintained at 37°C and 5% CO_2 prior to sub-culturing for transfection. At approximately 80-90% confluency, HepG2 T-75 flasks were trypsinized and plated at 2 x 10^6 cells/mL into a new flask. After 24 h, culture medium was replaced with Opti-MEM I reduced serum medium (Thermo Fisher Scientific) and T-75 flasks were transfected with a master mix containing FuGENE 6 transfection reagent (3 µL/µg plasmid DNA per flask; Promega, Madison, WI), Opti-MEM I reduced serum medium (500µL per flask), pGL4.74 [*hRluc*/TK] internal control vector (500 ng per flask; Promega), pGL3-basic-CYP3A4-362(7836/7208ins)-luc reporter construct (2 µg per flask; Blue Heron Biotech, Bothell, WA), a receptor construct (6 µg pCMV6-entry-mPXR or 2 µg pCMV6-XL4-hPXR per

flask; OriGene Technologies, Rockville, MD) or an empty vector (6 µg pCMV6-entry or 2 µg pCMV6-XL4 per flask; OriGene Technologies). Cells were transfected for 24 h and then trypsinized, counted and plated into fresh DMEM at 1 x 10^5 cells/well into a 96-well white plate (Costar). Following 24 h plating (48 h post-transfection), cells were treated in triplicate with either 0.1% DMSO control or 10 µM drug prepared in DMEM for a total of 24 h. After treatment, cells were lysed and the firefly luciferase and *R. reniformis* luciferase activities were quantified using a Dual-Glo Luciferase Reporter Assay (Promega). Luminescence was measured directly in the 96-well plate using a Synergy HT plate reader (BioTek, Winooski, VT). Firefly luciferase activity was normalized by taking the ratio of firefly luminescence to that of *R. reniformis* and results were expressed as fold change from DMSO control. A total of four independent experiments were performed.

Competitive ligand binding assay

A LanthaScreen hPXR competitive binding assay was employed to compare compound interactions with the receptor's ligand-binding domain. For these studies, purified human PXR ligand-binding domain (amino acids 111 to 434) containing an N-terminal glutathione S-transferase (GST) tag (10 nM hPXR-LBD-GST; Thermo Fisher Scientific) was incubated with a range of concentrations of the positive control SR 12813 (Sigma-Aldrich), EFV, 8-OHEFV and EFV analogs in the presence of a Fluormone PXR ligand (40 nM; Thermo Fisher Scientific) and a terbium labeled anti-GST antibody (10 nM; Thermo Fisher Scientific) using a 384-well low-volume black plate (Costar). Reactions were incubated at room temperature for 1 h covered prior to reading

fluorescence. Using a monochromator-based plate reader, specifically a Tecan Safire 2 (Tecan Group Ltd., Männedorf, Switzerland), the terbium fluorophore was excited at 332 nm, yielding an emission peak at 485 nm. Under the same excitation conditions, the Fluormone acceptor emission was observed at 515 nm due to energy transfer from the terbium donor known as fluorescence resonance energy transfer or FRET. Data was expressed as a ratio of Fluormone (515 nm) over terbium (485 nm) emission and fit to a log(inhibitor) versus response curve with variable slope to determine IC_{50} values for each compound.

Molecular docking simulations

To date, there are 21 high-resolution crystal structures of hPXR-LBD published in the RCSB Protein Data Bank and 14 of these structures are of the hPXR-LBD in complex with ligand. To select a hPXR-LBD-ligand complex suitable for molecular docking, structures were ranked by resolution ≤ 2.5 Å, $R_{value} \leq$ resolution/10 and the difference of R_{value} and $R_{free} \leq 0.05$, which are criteria previously employed in computational studies investigating this nuclear receptor (19). R_{value} is a measure of the quality of the atomic model obtained from the observed X-ray diffraction data compared to simulated data in order to make refinements to the final structure. Alternatively, the R_{free} value is calculated by how well the simulated model predicts a portion of observed diffraction data that was not subjected to the refinement process. Further, the difference between R_{value} and R_{free} reflects the extent to which a structure may have been overfit to the model (20). There were two hPXR-LBD crystal structures that met these criteria 1M13 (co-crystalized with hyperforin, resolution of 2.15 Å, $R_{value} = 0.212$, $R_{free} = 0.246$) and 4X1G (co-crystallized

with estrogen, resolution of 2.00 Å, $R_{value} = 0.182$, $R_{free} = 0.210$) and are overlayed in Figure 2A. The macromolecule 4X1G, however, is missing residues Thr311, Ala312, Gly313, Gly314 and Phe315 of the characteristic PXR flexible loop which extends from Glu309 to Glu321. Because of this, 1M13 was selected to move forward with for molecular docking and this structure was previously vetted and confirmed for use in computational studies (19, 21).

Molecular docking was simulated using the open-source software PyRx which utilizes the automated tool AutoDock (1, 22). Structure data files were generated for each ligand using ChemBioDraw, imported into PyRx for energy minimization and converted into PDBQT files for docking. The 1M13 receptor file was imported into PyRx from the RCS Protein Data Bank and prepared by removing the bound ligand in addition to non-polar hydrogens and water molecules. The active site was defined using the 28 residues known to line the hPXR ligand-binding pocket: Leu240, Met243, Ala244, Met246, Ser247, Phe251, Phe281, Cys284, Gln285, Phe288, Trp299, Tyr306, Thr311, Gly314, Phe315, Leu319, Met323, His407, Leu411, Ile414, Gln415, Ile417, His418, Phe420, Ala421, Met425, Gln426 and Phe429 (23). All ligands were docked into the 1M13 structure using the AutoDock v. 4.2 tool and a 25 x 25 x 25 point grid with 1 Å spacing in order to encompass the ligand-binding pocket as depicted in Figure 2B. The Lamarckian algorithm was used to search for low energy binding modes and in doing so the parameters were set to a total of ten runs with a maximum of 2.5×10^6 energy evaluations per docked ligand. The resulting poses were ranked in order of binding energy and nearly all of the docking simulations were within 1.0 kcal/mol of the lowest energy pose;

therefore, the most populated pose was used for subsequent analyses. The Pymol molecular graphics system v. 1.8 was used for the analysis of PyRx docking simulation results and employed for the generation of structural models. Further, the amino acid residues within a radius of 4 Å of compound were used to define the ligand binding site.

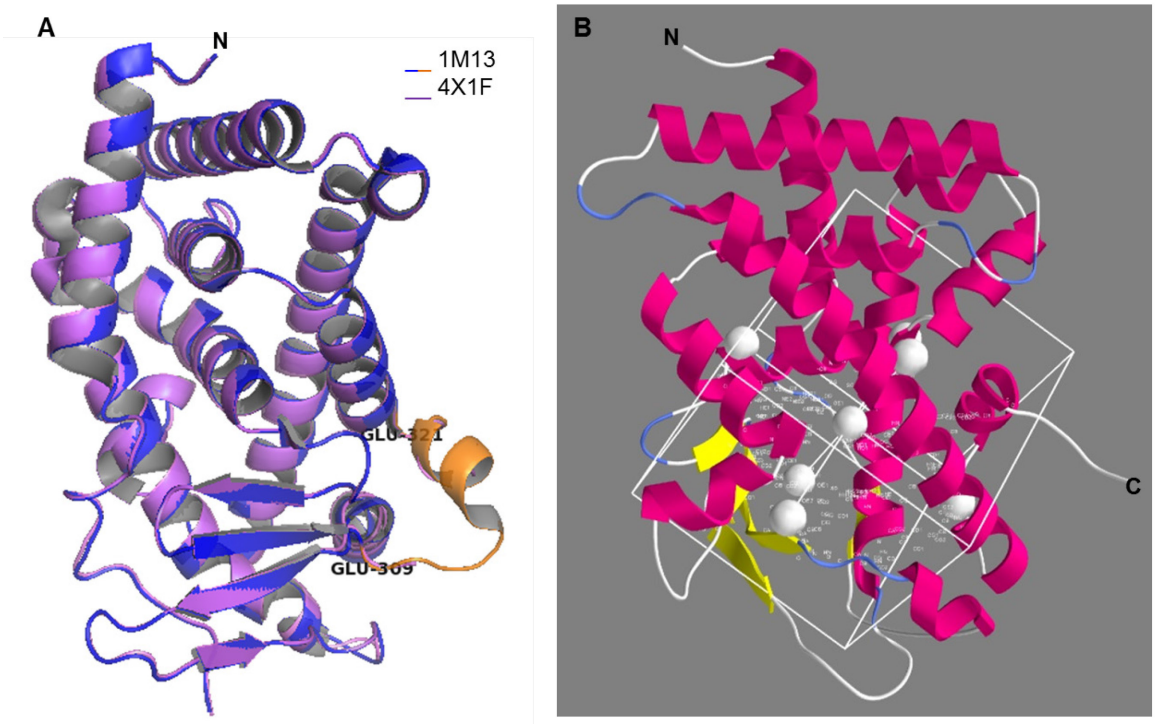

Figure 2. Selection and preparation of 1M13 hPXR-ligand-binding domain crystal structure for molecular docking. (A) The high resolution crystal structures 1M13 (2.15 Å, blue) and 4X1F (2.00 Å, purple) co-crystallized with hyperforin and estrogen, respectively, were overlayed to demonstrate 4X1F is not suitable for molecular docking as it is missing the flexible loop region of PXR from residues Glu309 to Glu321 as highlighted in 1M13 (orange). (B) 1M13 was prepared for ligand docking in PyRx using

a 25 x 25 x 25 point grid with 1 Å spacing encompassing the 28 residues of the ligand-binding pocket as seen labeled in white.

Determination of ligand-binding pocket interactions

The open-source software LigPlot^{+} was utilized to compare the PyRx docking results for each compound (24). Receptor-ligand PDB format files were generated in Pymol prior to importing into LigPlot^{+} for analysis of ligand-protein interactions. LigPlot^{+} was then used to produce a two-dimensional diagram of ligand-protein interactions, identifying both polar and hydrophobic contacts.

Statistical Analysis of Data

Results are expressed as means ± standard deviation. Comparisons between experimental conditions were performed using an unpaired one-tailed Student's t-test (GraphPad Prism 6 software). Statistical significances are denoted as: *, $p \leq 0.05$; **, $p \leq 0.01$; ***, $p \leq 0.001$.

Results

Effect of EFV, 8-OHEFV and EFV analogs on Cyp3a11 mRNA expression in primary hepatocytes isolated from WT and transgenic mice

EFV was previously demonstrated to activate both human and mouse PXR using a luciferase reporter assay and was observed to modulate CYP3A4 mRNA expression in primary human hepatocytes (6). We first sought to recapitulate the modulation of PXR target gene expression by EFV using hepatocytes isolated from WT male mice. EFV (10 μM) increased the murine PXR target gene Cyp3a11 in a time-dependent manner similar to the positive control PCN (Figure 3A). Further at 72 h, EFV increased Cyp3a11

mRNA to almost 80-fold compared to 46-fold for PCN. In addition, all EFV analogs significantly increased Cyp3a11 mRNA ranging from 2- to 41-fold following 72 h of treatment with the exclusion of the smallest analog 10 (223 Da) and analog 16 which lacks an amine compared to EFV. Unexpectedly, the primary oxidative metabolite of EFV, 8-OHEFV, which differs in mass from the parent drug by a single hydroxyl group, exhibited no modulation of Cyp3a11 mRNA across all time points tested.

In order to investigate potential species-specific differences, these same drug treatments were performed using hepatocytes isolated from humanized mice expressing hPXR. These mice express hPXR, but not mPXR, in the liver and intestines at both the mRNA and protein level (25). Moreover, the humanized hPXR mouse line was deemed functional as modulation of Cyp3a11 mRNA expression was observed with dosing of the prototypic hPXR agonist RIF (25). EFV and RIF treatment of hepatocytes isolated from humanized hPXR mice increased Cyp3a11 mRNA to 28- and 24-fold, respectively, at 72 h (Figure 3B). Interestingly, the second largest EFV analog 6 (409 Da), which lacks an intact oxazinone ring compared to EFV, increased Cyp3a11 mRNA levels to the greatest extent by 84-fold following 72 h treatment. In contrast, the smallest increase of Cyp3a11 mRNA abundance observed was 2.5-fold mediated by analog 13, which is roughly the same size as EFV, but contains a trans alkene and is quinazolinone derivative. Of note, analogs 10, 16 and 8-OHEFV did not significantly impact Cyp3a11 mRNA similar to WT drug treatments. In addition, analogs 1, 11, 14 and 15 failed to increase target gene expression relative to DMSO control.

Taking this work a step further, hepatocytes isolated from male mice genetically deficient of PXR ($PXR^{-/-}$) were treated in order to test for PXR-dependent modulation of Cyp3a11 mRNA as a downstream readout for receptor activation. In addition to PXR, the constitutive androstane receptor (CAR) has also been demonstrated to exhibit transactivation of CYP3a genes and EFV is a known agonist of CAR (5, 26). EFV-mediated modulation of Cyp3a11 mRNA was almost fully abrogated in hepatocytes isolated from $PXR^{-/-}$ mice compared to WT and hPXR treatment groups following 72 h of treatment (Figure 3C). Yet, analogs 7, 10, 15, 16 and 8-OHEFV drug treatments were not significantly decreased for $PXR^{-/-}$ treatments compared to WT at 72 h. Further, when comparing $PXR^{-/-}$ to hPXR hepatocyte treatments, analogs 1, 4, 9, 10, 11, 13, 14, 15, 16 and 8-OHEFV exhibited no significant difference between groups following 72 h of treatment.

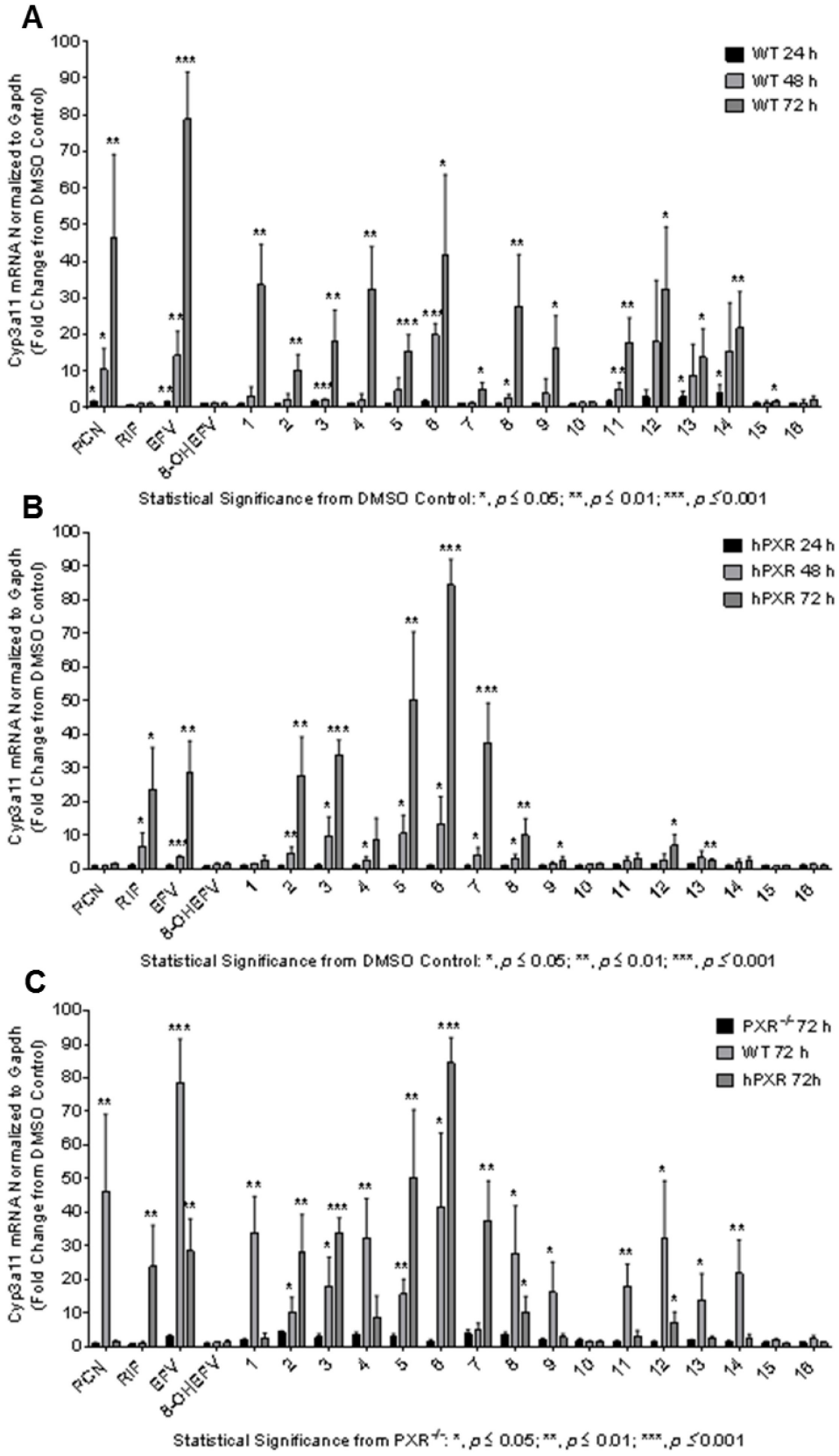
A
CypSa11 mRNA Normalized to Gapdh
(Fold Change from DMSO Control)
WT 24 h
WT 48 h
WT 72 h
PCN
RIF
EFV
8-OHEFV
1
2
3
4
5
6
7
8
9
10
11
12
13
14
15
16
Statistical Significance from DMSO Control: *, p ≤ 0.05; **, p ≤ 0.01; ***, p ≤ 0.001
B
CypSa11 mRNA Normalized to Gapdh
(Fold Change from DMSO Control)
hPXR 24 h
hPXR 48 h
hPXR 72 h
PCN
RIF
EFV
8-OHEFV
Statistical Significance from DMSO Control: *, p ≤ 0.05; **, p ≤ 0.01; ***, p ≤ 0.001
C
CypSa11 mRNA Normalized to Gapdh
(Fold Change from DMSO Control)
PXR-/- 72 h
WT 72 h
hPXR 72h
PCN
RIF
EFV
8-OHEFV
Statistical Significance from PXR-/-: *, p ≤ 0.05; **, p ≤ 0.01; ***, p ≤ 0.001

Figure 3. Comparative effects of EFV, 8-OHEFV and EFV analogs on the modulation of the PXR target gene Cyp3a11 mRNA expression in primary mouse hepatocytes. Hepatocytes were isolated from (A) WT and (B) humanized male mice expressing hPXR and treated for 24, 48 and 72 h with either 0.1% DMSO as vehicle control or 10 μM drug. PCN and RIF, 10 μM each, served as positive controls for WT and hPXR treatment groups, respectively. Following drug treatment, RNA was isolated from hepatocytes using TRIzol. RNA (1 μg) was then reverse transcribed to cDNA for use in qPCR to measure Cyp3a11 and Gapdh mRNA levels. To demonstrate target gene expression was modulated in a PXR-dependent manner, (C) WT and hPXR 72h drug treatments were compared to corresponding Cyp3a11 mRNA levels in hepatocytes isolated from male mice genetically deficient of PXR ($PXR^{-/-}$). Data are shown as mean fold change from DMSO control ± S.D. for four independent experiments. Statistical significance from control (A, B) or $PXR^{-/-}$ drug treatment (C) is shown as *, $p \leq 0.05$, **, $p \leq 0.01$ and ***, $p \leq 0.001$.

Comparison of EFV, 8-OHEFV and EFV analogs on mPXR and hPXR activation using transiently transfected HepG2 cells

We demonstrated EFV and select EFV analogs modulated Cyp3a11 mRNA expression in a PXR-dependent manner. Moving forward, we utilized a luciferase reporter assay in order to test for direct activation of PXR by these compounds. Two regulatory regions of *CYP3A4* have been previously identified to contain PXR response elements critical for facilitating transcriptional activation by xenobiotics, specifically a proximal promoter region from bases -362 to +53 and a more distal region spanning

bases -7836 to 7208 upstream of the transcription start site (27). Knowing this, human hepatocellular carcinoma HepG2 cells were transfected with the plasmid pGL3-basic-CYP3A4-362(7836/7208ins)-luc, containing a firefly luciferase gene under the control of the PXR-activated regulatory elements, as a critical component for assaying transcriptional activity in addition to overexpressing full-length PXR (28). In agreement with previously published data, EFV (10 μM) activated both mouse and human PXR (Figures 4A and 4B) (6). PCN, the positive control for mPXR activation, yielded the most robust increase in firefly luciferase activity of 3-fold relative to empty vector drug treatment indicating mPXR activation followed by EFV and analogs 14 and 3 with increases of 2.5-, 2.2- and 2.0- fold, respectively (Figure 4A). As anticipated, RIF had no effect on mPXR activation. There were several drug treatments, however, that did not exhibit firefly luciferase activity significantly greater than the empty vector control, and hence failed to activate mPXR, those being 8-OHEFV and analogs 1, 2, 5, 10, 12, 13, 15 and 16. RIF, the positive control for hPXR activation, yielded the greatest increase in firefly luciferase activity of 9.5-fold relative to empty vector drug treatment indicative of strong hPXR activation (Figure 4B). In contrast, PCN had no effect on hPXR activation as expected. Second to RIF treatment, two of the largest EFV analogs 6 (409 Da) and 7 (423 Da) increased firefly activity by 6.7- and 6.9-fold, respectively. Interestingly, analog 5, with the chiral center in the *R* configuration relative to the *S* configuration of stereoisomer analog 6, increased firefly luciferase activity to a much lesser extent by a difference of 3-fold. In addition to EFV, all drug treatments increased firefly luciferase activity, thereby demonstrated hPXR activation, significantly greater than their

corresponding empty vector control with the exclusion of 8-OHEFV and the smallest analog 10.

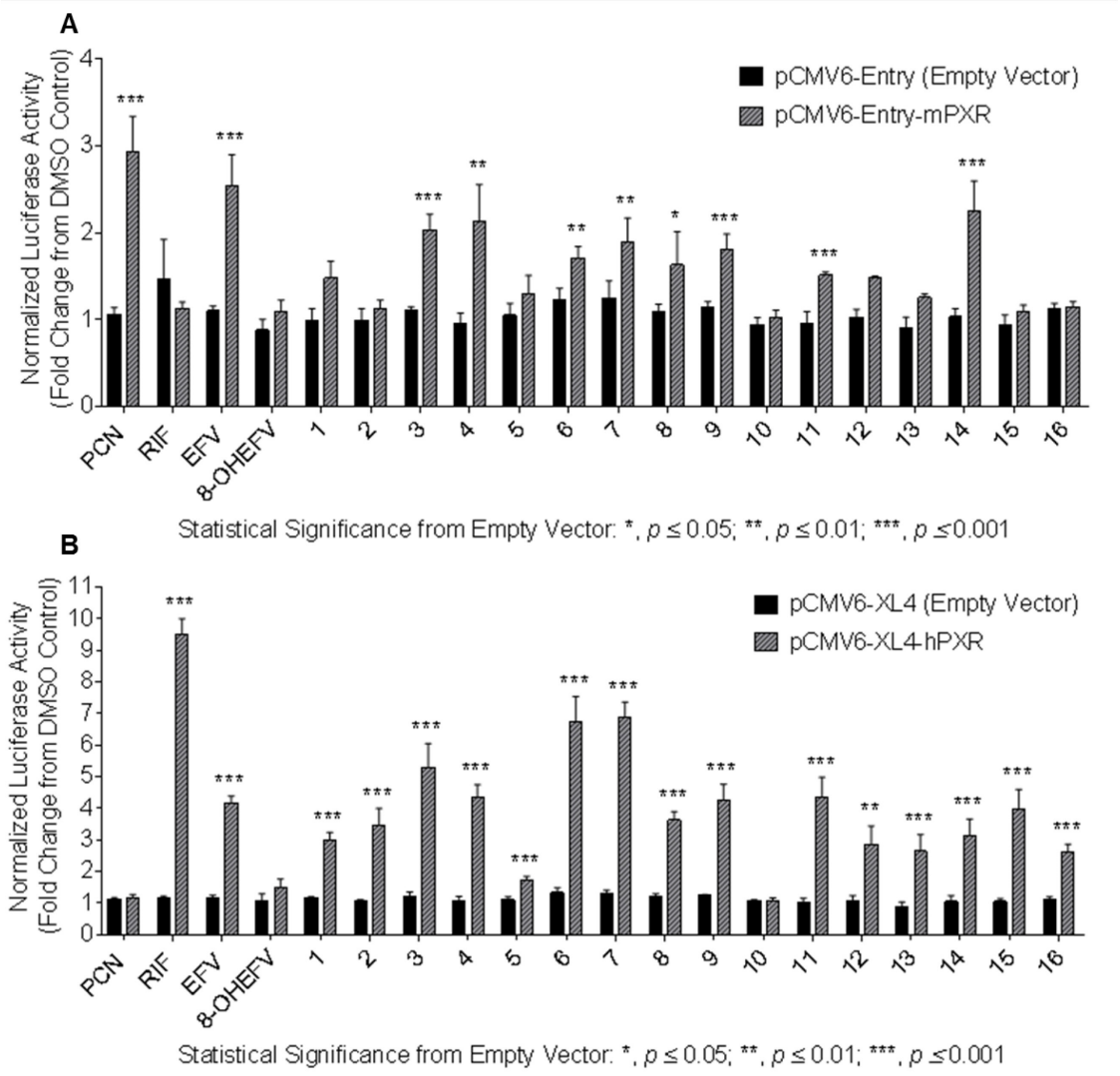

Figure 4. Comparative effects of EFV, 8-OHEFV and EFV analogs on the activation of mouse and human PXR in transiently transfected HepG2 cells. HepG2 cells were transfected with a pGL4.74 [*hRluc*/TK] internal control vector, a pGL3-basic-CYP3A4-362(7836/7208ins)-luc reporter construct, a receptor construct (A) pCMV6-entry-mPXR, (B) pCMV6-XL4-hPXR or a corresponding empty vector. Following 48 h post-

transfection, cells were treated in triplicate with either 0.1% DMSO control or 10 μM drug for 24 h. PCN and RIF, 10 μM each, served as positive controls for mPXR and hPXR activation, respectively. After treatment, firefly luciferase and *R. reniformis* luciferase activities were quantified using a dual-glo luciferase reporter assay. Firefly luciferase activity was normalized by taking the ratio of firefly luminescence to that of *R. reniformis*. Data are shown as mean fold change from DMSO control ± S.D. for four independent experiments. Statistical significance from empty vector drug treatment is shown as *, $p \leq 0.05$, **, $p \leq 0.01$ and ***, $p \leq 0.001$.

Competitive ligand binding of EFV, 8-OHEFV and select EFV analogs to the hPXR ligand-binding domain

Building upon the observations that EFV and select EFV analogs could stimulate a biological effect mediated through PXR activation, specifically modulation of Cyp3a11 mRNA expression in primary mouse hepatocytes and transactivation of CYP3A4 by reporter assay in HepG2 cells, we next wanted to compare strengths of ligand-receptor interactions using a competitive binding assay. In this assay, PXR ligands were characterized through their ability to compete with and displace a fluorescent PXR ligand Fluormone green, thereby resulting in a corresponding decrease in fluorescence. RIF has been well-demonstrated to interfere with the emission of both the terbium and Fluormone fluorophores implemented in this assay, therefore, the hPXR ligand SR12813 was used as the positive control (29). SR12813 (0.062 nM to 100 μM) demonstrated a dose-dependent decrease in 515 nm/485 nm TR-FRET ratio with a half-maximal inhibitory concentration (IC_{50}) value of 0.14 μM, which is in agreement with previously published

studies (Figure 5) (30). It is important to note that compound solubility limited the maximal concentration, either 300 μM or 900 μM, tested for compounds in subsequent studies. EFV (0.062 nM to 300 μM) resulted in an IC_{50} of 18.74 μM. PXR is a high-capacity, low-affinity nuclear receptor and the observed IC_{50} for EFV falls in line with previously characterized "moderate binders" ranging from half-maximal excitatory values of 1 μM to 100 μM (31). Analog 10 (0.062 nM to 900 μM), which in our former studies exhibited no biological effect mediated through PXR activation, was unable to displace the Fluormone ligand even at the highest compound concentration tested at 900 μM. That being said, 8-OHEFV (0.062 nM to 900 μM), which also had no impact on Cyp3a11 mRNA expression or CYP3A4 transactivation, was able to displace the competitive ligand with an IC_{50} of 12.14 μM comparable to that of EFV. Analog 6, the second to largest analog tested of 409 Da and the most potent agonist of hPXR by our studies, inhibited ligand binding with an IC_{50} of 4.46 μM, four times lower than that of EFV. Interestingly, analog 5, the stereoisomer of analog 6, exhibited a slightly more potent IC_{50} of 1.93 μM. Three additional analogs 14, 15 and 16 were investigated for ligand-receptor binding interactions by this assay as these compounds differed structurally from EFV by a single atom. Moreover, for analog 14, the heterocyclic oxygen of EFV is substituted with a carbon atom, whereas analogs 15 and 16 lack the heterocyclic amine of EFV, which is substituted with an oxygen or carbon atom, respectively. These substitutions within the heterocyclic ring of EFV may disrupt and/or enhance polar interactions within PXR's ligand-binding pocket. All three analogs

exhibited IC_{50} values two to seven times lower than EFV of 8.38 µM, 5.55 µM and 2.52 µM for analogs 14, 15 and 16, respectively.

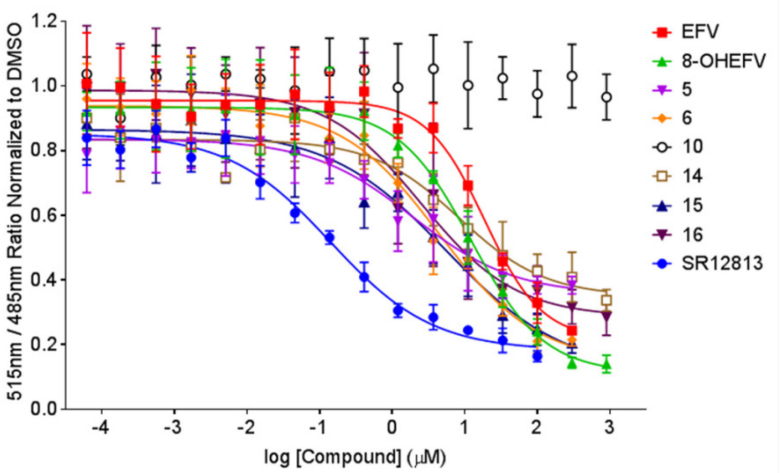

Compound	IC_{50} (µM)
EFV	18.74
8-OHEFV	12.14
5	1.93
6	4.46
10	N.D.
14	8.38
15	5.55
16	2.52
SR12813	0.14

Figure 5. Competitive ligand binding of EFV, 8-OHEFV and select EFV analogs to the hPXR ligand-binding domain. hPXR-LBD (10 nM) with an N-terminal GST tag was incubated individually with a range of concentrations of the positive control SR12813, EFV, 8-OHEFV and EFV analogs 5, 6, 10, 14, 15 and 16 in the presence of a Fluormone PXR ligand (40 nM) and a terbium labeled anti-GST antibody (10 nM). DMSO (1%) was a vehicle control for all reactions. Excitation of the terbium fluorophore at 332 nm, yielded an emission peak at 485 nm. Under the same excitation conditions, the Fluormone acceptor emission was observed at 515 nm due to FRET. Data are expressed as a ratio of Fluormone (515 nm) over terbium (485 nm) emission and normalized to DMSO treatment as the maximally observed time-resolved FRET ratio. Normalized data from four independent experiments were then fit to a log(inhibitor) versus response curve with variable slope to determine IC_{50} values for each compound as summarized in the table above.

Molecular docking of EFV, 8-OHEFV and EFV analogs in the ligand-binding domain of hPXR

With the aim of understanding ligand-receptor interactions that may confer PXR activation, we performed a molecular modeling study in which EFV, 8-OHEFV and sixteen EFV analogs were docked into the ligand-binding pocket of hPXR (1M13; Figure 6). Our docking results showed all investigational compounds occupied an area in the ligand-binding pocket primarily sandwiched between helices 3 and 6. The ligand-binding pocket is largely hydrophobic and, consistent with previous molecular docking studies, majority of the ligand contacts observed were with non-polar residues as analyzed using two-dimensional renderings of energetically favorable ligand poses (Figure 7) (32). Overall, docked ligands were predicted to form contacts with ten hydrophobic residues M243, M246, M250, F251, F281, F288, W299, M323, L411 and F429 and six polar residues S247, C284, Q285, Y306, H327 and H407 as summarized in Table 1. Molecular docking was also performed with the prototypic hPXR agonists hyperforin (HYP), SR12813 and RIF in addition to the negative control PCN and all hydrophobic and/or polar contacts observed in these simulations were in line with previous published reports (18, 33, 34). Further, docked ligands made polar contacts with the side-chain Ser247 to the greatest extent (12 ligands out of 18), followed by Q285 (6 ligands out of 18), Cys284 (2 ligands out of 18) and Met243 (1 ligand out of 18). More specifically, EFV made simultaneous polar contacts with Ser247 and Q285 with the amine of the oxazinone ring and a fluorine of the trifluoromethyl group, respectively (Figure 7). In addition, the Cl-phenyl group of EFV was observed to fit stably into the hydrophobic pocket formed by

the side-chains Phe288 (helix 6), Trp299 (beta strand 1) and Tyr306 (beta strand 2) (Figure 8). The Cl-phenyl group of EFV appears to make a favorable "edge-on" Cl-π interaction with Phe288 and this electrostatic interaction was conserved for the docking conformations of analogs 11 and 12 (35). In contrast, 8-OHEFV, which is the only compound investigated in our study to contain any modification to the Cl-phenyl ring of EFV, formed unfavorable and potentially destablizing interactions with the highly hydrophobic area defined by Phe288, Trp299 and Tyr306 mediated by the ligand's hydroxyl group meta to the Cl atom in addition to the oxazinone amine and carbonyl oxygen (Figure 8). Interestingly, analog 10, which failed to activate hPXR and competitively bind to the receptor's ligand-binding domain, was able to make side-chain polar contacts to S247 and C284 and a main-chain contact to Met243 within the active site (Figure 7). That being said, analog 10 is the smallest ligand investigated of 223 Da with a molecular surface area of 192 $Å^2$ and as such made the fewest number of hydrophobic contacts within the hPXR active site.

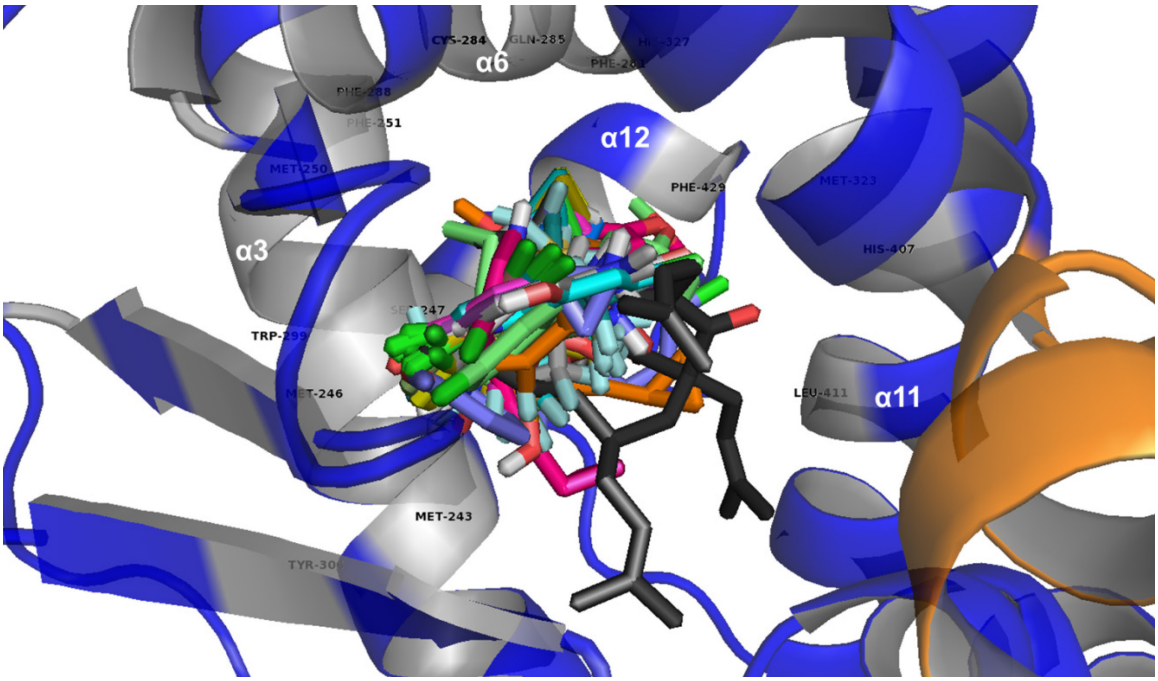

Figure 6. Molecular docking of EFV, 8-OHEFV and sixteen EFV analogs into the ligand-binding pocket of hPXR (1M13). Molecular docking was simulated using PyRx. All ligands were docked into the 1M13 structure using AutoDock and a 25 x 25 x 25 point grid with 1 Å spacing in order to encompass the ligand-binding pocket. The most populated pose for each ligand is shown docked into the PXR-LBD simultaneously with the co-crystallized ligand hyperforin (black). The amino acid residues within a radius of 4 Å of EFV, 8-OHEFV and EFV analogs were M243, M246, S247,M250, F251, F281, C284, Q285, F288, W299, Y306, M323, H327, H407, L411 and F429 and are labeled above.

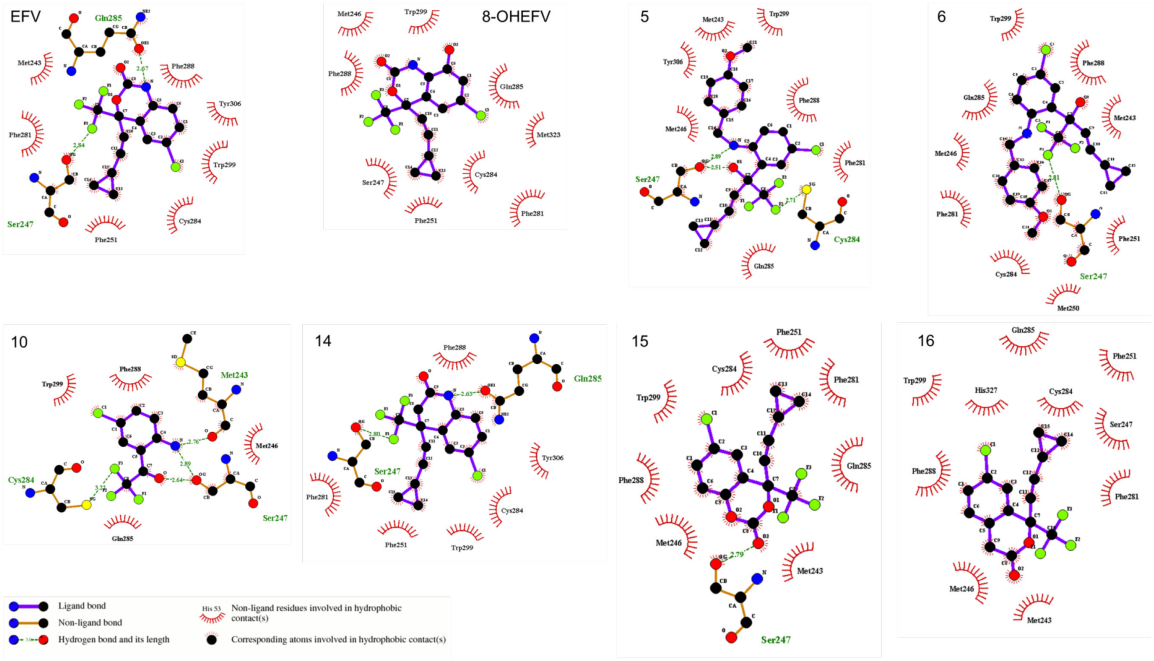

Figure 7. Two-dimensional representation of binding modes for EFV, 8-OHEFV and select EFV analogs in the ligand-binding pocket of hPXR (1M13). The open-source software LigPlot^{+} was used to generate two-dimensional diagrams of ligand-protein interactions in order to compare PyRx docking results across compounds. This analysis was performed for all eighteen investigational ligands, however, representative schematics are shown only for EFV, 8-OHEFV, and EFV analogs 5, 6, 10, 14, 15 and 16.

	M243	*M246*	**S247**	M250	*F251*	*F281*	**C284**	**Q285**	*F288*	*W299*	**Y306**	*M323*	**H327**	**H407**	*L411*	*F429*
EFV	◊	-	●	-	◊	◊	◊	●	◊	◊	◊	-	-	-	-	-
8-OHEFV	-	◊	◊	-	◊	◊	◊	◊	◊	◊	-	◊	-	-	-	-
1	-	-	●	-	◊	◊	◊	●	◊	◊	◊	-	-	-	-	-
2	○	◊	●	-	◊	◊	◊	●	◊	◊	-	-	-	-	-	-
3	◊	◊	●	-	◊	◊	◊	◊	◊	◊	-	-	-	-	-	-
4	◊	◊	●	-	◊	◊	◊	◊	◊	◊	-	-	-	-	-	-
5	◊	◊	●	-	-	◊	●	◊	◊	◊	◊	-	-	-	-	-
6	◊	◊	●	◊	◊	◊	◊	◊	◊	◊	-	-	-	-	-	-
7	●	◊	◊	◊	◊	◊	◊	◊	◊	◊	◊	-	-	-	-	◊
8	◊	◊	◊	-	◊	◊	◊	●	◊	◊	-	-	-	-	-	-
9	◊	◊	●	-	◊	◊	◊	●	◊	◊	-	-	-	-	◊	◊
10	○	◊	●	-	-	-	●	◊	◊	◊	-	-	-	-	-	-
11	-	-	◊	-	◊	◊	◊	◊	◊	◊	◊	-	-	◊	-	-
12	-	-	◊	-	◊	◊	◊	◊	◊	◊	◊	◊	-	-	-	-
13	◊	◊	●	-	◊	◊	◊	◊	◊	◊	-	-	◊	-	-	-
14	-	-	●	-	◊	◊	◊	●	◊	◊	◊	-	-	-	-	-
15	◊	◊	●	-	◊	◊	◊	◊	◊	◊	-	-	-	-	-	-
16	◊	◊	◊	-	◊	◊	◊	◊	◊	◊	-	-	◊	-	-	-
HYP	◊	◊	●	◊	◊	◊	◊	●	◊	◊	◊	◊	-	◊	-	-
SR12813	●	◊	●	◊	◊	◊	◊	◊	◊	◊	◊	-	◊	◊	-	-
RIF*	◊	●	●	●	●	◊	●	◊	●	◊	-	-	◊	●	◊	●
PCN	◊	-	◊	-	◊	◊	-	◊	◊	◊	◊	-	◊	-	-	◊

◊ Hydrophobic Contact; ● Polar Contact (Sidechain); ○ Polar Contact (Mainchain); - No Interaction

*RIF made additional hydrophobic contacts with F166, T248, Y249, A280, V291, C301, T408 and M425

Table 1. Tabular representation of predicted active site ligand-hPXR interactions.

Summary of molecular docking simulations generated in PyRx and analyzed using LigPlot^{+}. The polar and hydrophobic contacts formed for eighteen investigational ligands are shown in comparison to the potent and prototypic hPXR agonists hyperforin (HYP), SR12813 and RIF in addition to the negative control PCN. Hydrophobic residues are italicized and polar residues are shown in bold. M250 is not highlighted as this residue does not line the ligand-binding pocket, but was observed to interact with docked ligands.

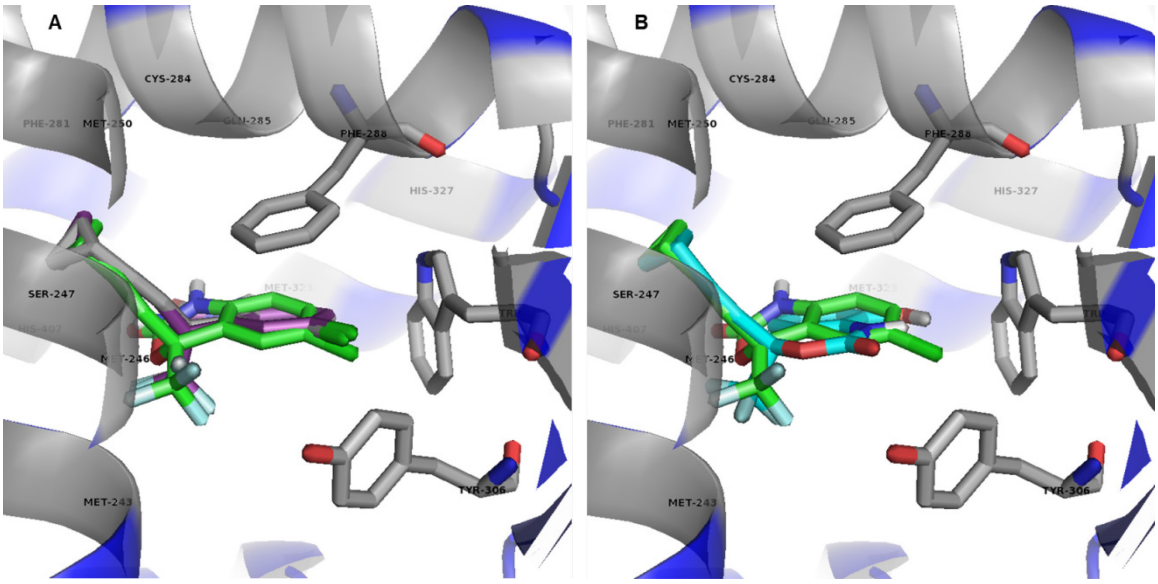

Figure 8. Docking comparison of EFV, 8-OHEFV and EFV analogs 11 and 12 into the ligand-binding pocket of hPXR (1M13). (A) The energetically favorable docking modes of EFV (green) and EFV analogs 11 (purple) and 12 (gray) in the hPXR active site. The Cl-phenyl group across all three compounds fits stably into the hydrophobic pocket formed by the side-chains Phe288, Trp 299 and Tyr306. In contrast, (B) the more polar compound 8-OHEFV (in cyan overlayed with EFV in green) forms unfavorable and potentially destablizing interactions with the highly hydrophobic area mediated by the ligand's hydroxyl group meta to the Cl atom in addition to the oxazinone amine and carbonyl oxygen.

Discussion

PXR is a ligand-activated transcription factor that is involved in the regulation of biologically important genes that contribute to cellular homeostasis within the liver and intestines (36). In addition to its endogenous function(s), PXR exhibits broad substrate

specificity and can accommodate binding of structurally diverse activators enabling the receptor to act as a xenobiotic sensor. Further, a consequence of agonist binding to PXR stimulates the induction of target genes encoding drug metabolizing enzymes that can thereby enhance global drug metabolism and yield potential drug-drug interactions. Enzyme induction mediated by PXR activation, primarily of the cytochromes P450 which metabolize approximately 75% of pharmaceuticals, is a constant obstacle for drug discovery and development (37). Therefore, characterization of compounds that activate PXR will inform the structure-activity relationship of a series of ligands and the receptor and may enable the prediction of xenobiotics that bind PXR and modulate drug biotransformation and clearance.

In this study, we investigated the structure-activity relationship of the anti-HIV drug EFV and PXR. In doing so, we utilized a panel of sixteen EFV analogs ranging from 223 to 423 Da in size that contained either subtle or dramatic modifications to the oxazinone ring of EFV (analogs 1, 2, 5, 6, 7, 8, 9, 10, 11, 12, 13, 14, 15 and 16) in addition to modification of the alkyne bond of EFV to a trans alkene (analogs 3 and 13) and ring opening of the cyclopropyl group (analog 4). We also included the primary oxidative metabolite of EFV, 8-OHEFV, in these studies as the only investigational compound to contain a modification to the Cl-phenyl group of EFV. Further, using these compounds of a similar scaffold, we observed that ligand size and polarity were key determinants in conferring agonism of PXR.

A previous report by Xio et al. suggested that molecular weight may serve as a useful marker for the identification of PXR binders (31). Moreover, this group proposed

ligands ≤ 300 Da in size are unable to form meaningful interactions within PXR's ligand-binding pocket. Prior to our work, EFV, which is 316 Da in size thereby approaching the proposed 300 Da molecular weight cut-off, was demonstrated to be a strong agonist of PXR by *in vitro* assay (28). In addition to recapitulating this observation, several EFV analogs were tested in our study that are less than 300 Da, analogs 1 (289Da), 2 (289 Da) and 10 (223 Da). Analogs 1 and 2 are *R* and *S* stereoisomers, respectively, that lack an intact oxazinone ring, but despite their molecular weights were able to activate both mouse and human PXR as demonstrated by time-dependent modulation of Cyp3a11 mRNA in hepatocytes isolated from both WT mice and humanized mice expressing hPXR in addition to facilitating transactivation of CYP3A4 by reporter assay in HepG2 cells. That being said, we did observe that the smallest compound tested, analog 10 (223 Da), was unable to neither competitively bind to PXR's ligand-binding domain nor confer PXR activation. Using molecular docking simulations, we further observed that analog 10 was surprisingly able to make polar contacts within the ligand-binding pocket of PXR, however, failed to form extensive potentially stabilizing hydrophobic contacts. On average, the ligands investigated in our docking simulations formed contacts with eight hydrophobic residues, whereas analog 10 interacted with just four non-polar residues, Met246, Gln285, Phe288 and Trp299, which may be attributed to the ligand's small molecular surface area of 192 $Å^2$. Moreover, building upon these former studies, our work suggests a more narrow range of < 223 Da to > 289 Da for a molecular weight cutoff that may confer PXR activation in a species-independent manner.

In addition to confirming ligand size is indeed a limitation for promoting PXR activation, we observed that a compound's polarity may also have a substantial impact on stimulating a biological effect. EFV is extensively metabolized by the cytochromes P450 to form the major oxygenated metabolite 8-OHEFV (2). Further, EFV autoinduces its own metabolism through PXR activation thereby causing the circulating levels of 8-OHEFV to surpass that of parent drug with chronic administration (3). In line with this, our laboratory has previously demonstrated that 8-OHEFV is a reactive metabolite that may contribute to EFV-mediated hepatotoxicity (38). Therefore, we were interested in testing if this metabolite could also activate PXR and further contribute to the disruption of cellular homeostasis within the liver. We observed that chronic treatment of hepatocytes isolated from WT mice of humanized mice expressing hPXR with 8-OHEFV caused no significant modulation of Cyp3a11 mRNA expression. Of note, 8-OHEFV has been observed in human liver microsomes to be subsequently metabolized to the dioxygenated metabolite 8,14-OHEFV and can also undergo *O*-linked glucuronidation in human and rodent liver microsomes, so it is plausible the metabolite exhibited poor hepatocyte stability despite retreatment with drug every 24 h (2, 39). However, bolstering our previous observation, 8-OHEFV failed to activate PXR by a CYP3A4 luciferase reporter assay using transfected HepG2 cells, which characteristically express drug metabolizing enzymes at significantly lower basal levels compared to primary hepatocytes (40). It is also worth noting that hepatocyte and HepG2 cellular permeability of 8-OHEFV was not directly tested in these studies, yet the logP value of this metabolite is estimated to be 3.2 compared to 3.7 of EFV and, therefore, should be sufficiently

lipophilic to passively diffuse across the plasma membrane. Based upon the performed cellular assays, it was unanticipated to observe that 8-OHEFV could competitively bind to PXR-LBD and at a similar inhibitory potency to EFV. Subsequent molecular docking simulations, however, aided in the interpretation of these results. Unlike EFV which is predicted to form a favorable electrostatic Cl-π interaction of its Cl-phenyl group within a hydrophobic pocket formed by side-chain residues Phe288, Trp299 and Tyr306, the hydroxyl group of 8-OHEFV in addition to the oxazinone amine and carbonyl oxygen form a potentially destablizing interaction within this pocket. Structural studies of PXR have identified these three hydrophobic residues as the most important hot spot for ligand binding within the active site (41). Adding to this, a former study by Gao et al. have reported PXR activation may be attenuated with the addition of a single polar functional group, such as –OH or $–NH_2$, to a known agonist (42). Further, in support of our experimental observations, these authors demonstrated that phenyl groups, and specifically Cl-phenyl groups, are particularly optimal for fitting into this hydrophobic pocket of PXR (42).

In summary, we investigated the structure-activity relationship of the anti-HIV drug EFV and PXR and found through using compounds of a similar scaffold, ligand size and polarity were key determinants in conferring agonism of PXR. These findings can directly inform next-generation antiretroviral drug development in an effort to identify pharmacological agents that maintain antiviral potency with minimal drug-drug interactions due to the attenuation of PXR activation.

References

1. Dallakyan S, Olson AJ. Small-molecule library screening by docking with PyRx. Methods Mol Biol. 2015;1263:243-50.

2. Ward BA, Gorski JC, Jones DR, Hall SD, Flockhart DA, Desta Z. The cytochrome P450 2B6 (CYP2B6) is the main catalyst of efavirenz primary and secondary metabolism: implication for HIV/AIDS therapy and utility of efavirenz as a substrate marker of CYP2B6 catalytic activity. J Pharmacol Exp Ther. 2003;306(1):287-300.

3. Ngaimisi E, Mugusi S, Minzi OM, Sasi P, Riedel KD, Suda A, et al. Long-term efavirenz autoinduction and its effect on plasma exposure in HIV patients. Clin Pharmacol Ther. 2010;88(5):676-84.

4. Hariparsad N, Nallani SC, Sane RS, Buckley DJ, Buckley AR, Desai PB. Induction of CYP3A4 by efavirenz in primary human hepatocytes: comparison with rifampin and phenobarbital. J Clin Pharmacol. 2004;44(11):1273-81.

5. Faucette SR, Zhang TC, Moore R, Sueyoshi T, Omiecinski CJ, LeCluyse EL, et al. Relative activation of human pregnane X receptor versus constitutive androstane receptor defines distinct classes of CYP2B6 and CYP3A4 inducers. J Pharmacol Exp Ther. 2007;320(1):72-80. PMCID: 4091905.

6. Sharma D, Lau AJ, Sherman MA, Chang TK. Agonism of human pregnane X receptor by rilpivirine and etravirine: comparison with first generation non-nucleoside reverse transcriptase inhibitors. Biochem Pharmacol. 2013;85(11):1700-11.

7. Aranda A, Pascual A. Nuclear hormone receptors and gene expression. Physiol Rev. 2001;81(3):1269-304.

8. Germain P, Staels B, Dacquet C, Spedding M, Laudet V. Overview of nomenclature of nuclear receptors. Pharmacol Rev. 2006;58(4):685-704.

9. Squires EJ, Sueyoshi T, Negishi M. Cytoplasmic localization of pregnane X receptor and ligand-dependent nuclear translocation in mouse liver. J Biol Chem. 2004;279(47):49307-14.

10. Kawana K, Ikuta T, Kobayashi Y, Gotoh O, Takeda K, Kawajiri K. Molecular mechanism of nuclear translocation of an orphan nuclear receptor, SXR. Mol Pharmacol. 2003;63(3):524-31.

11. Timsit YE, Negishi M. CAR and PXR: the xenobiotic-sensing receptors. Steroids. 2007;72(3):231-46. PMCID: 1950246.

12. Moore LB, Maglich JM, McKee DD, Wisely B, Willson TM, Kliewer SA, et al. Pregnane X receptor (PXR), constitutive androstane receptor (CAR), and benzoate X receptor (BXR) define three pharmacologically distinct classes of nuclear receptors. Mol Endocrinol. 2002;16(5):977-86.

13. Hariparsad N, Chu X, Yabut J, Labhart P, Hartley DP, Dai X, et al. Identification of pregnane-X receptor target genes and coactivator and corepressor binding to promoter elements in human hepatocytes. Nucleic Acids Res. 2009;37(4):1160-73. PMCID: 2651806.

14. Kojima K, Nagata K, Matsubara T, Yamazoe Y. Broad but distinct role of pregnane x receptor on the expression of individual cytochrome p450s in human hepatocytes. Drug Metab Pharmacokinet. 2007;22(4):276-86.

15. Xu C, Wang X, Staudinger JL. Regulation of tissue-specific carboxylesterase expression by pregnane x receptor and constitutive androstane receptor. Drug Metab Dispos. 2009;37(7):1539-47. PMCID: 2698945.

16. Shang W, Liu J, Chen R, Ning R, Xiong J, Liu W, et al. Fluoxetine reduces CES1, CES2, and CYP3A4 expression through decreasing PXR and increasing DEC1 in HepG2 cells. Xenobiotica. 2016;46(5):393-405.

17. Vyhlidal CA, Rogan PK, Leeder JS. Development and refinement of pregnane X receptor (PXR) DNA binding site model using information theory: insights into PXR-mediated gene regulation. J Biol Chem. 2004;279(45):46779-86.

18. Watkins RE, Wisely GB, Moore LB, Collins JL, Lambert MH, Williams SP, et al. The human nuclear xenobiotic receptor PXR: structural determinants of directed promiscuity. Science. 2001;292(5525):2329-33.

19. Lau AJ, Yang G, Yap CW, Chang TK. Selective agonism of human pregnane X receptor by individual ginkgolides. Drug Metab Dispos. 2012;40(6):1113-21.

20. Kleywegt GJ, Jones TA. Model building and refinement practice. Methods Enzymol. 1997;277:208-30.

21. Ekins S, Kortagere S, Iyer M, Reschly EJ, Lill MA, Redinbo MR, et al. Challenges predicting ligand-receptor interactions of promiscuous proteins: the nuclear receptor PXR. PLoS Comput Biol. 2009;5(12):e1000594. PMCID: 2781111.

22. Morris GM, Huey R, Lindstrom W, Sanner MF, Belew RK, Goodsell DS, et al. AutoDock4 and AutoDockTools4: Automated docking with selective receptor flexibility. J Comput Chem. 2009;30(16):2785-91. PMCID: 2760638.

23. Ostberg T, Bertilsson G, Jendeberg L, Berkenstam A, Uppenberg J. Identification of residues in the PXR ligand binding domain critical for species specific and constitutive activation. Eur J Biochem. 2002;269(19):4896-904.

24. Laskowski RA, Swindells MB. LigPlot+: multiple ligand-protein interaction diagrams for drug discovery. J Chem Inf Model. 2011;51(10):2778-86.

25. Scheer N, Ross J, Rode A, Zevnik B, Niehaves S, Faust N, et al. A novel panel of mouse models to evaluate the role of human pregnane X receptor and constitutive androstane receptor in drug response. J Clin Invest. 2008;118(9):3228-39. PMCID: 2493444.

26. Wei P, Zhang J, Dowhan DH, Han Y, Moore DD. Specific and overlapping functions of the nuclear hormone receptors CAR and PXR in xenobiotic response. Pharmacogenomics J. 2002;2(2):117-26.

27. Goodwin B, Hodgson E, Liddle C. The orphan human pregnane X receptor mediates the transcriptional activation of CYP3A4 by rifampicin through a distal enhancer module. Mol Pharmacol. 1999;56(6):1329-39.

28. Chang TK, Waxman DJ. Pregnane X receptor-mediated transcription. Methods Enzymol. 2005;400:588-98.

29. Shukla SJ, Nguyen DT, Macarthur R, Simeonov A, Frazee WJ, Hallis TM, et al. Identification of pregnane X receptor ligands using time-resolved fluorescence resonance energy transfer and quantitative high-throughput screening. Assay Drug Dev Technol. 2009;7(2):143-69. PMCID: 3116688.

30. Chen Y, Tang Y, Robbins GT, Nie D. Camptothecin attenuates cytochrome P450 3A4 induction by blocking the activation of human pregnane X receptor. J Pharmacol Exp Ther. 2010;334(3):999-1008. PMCID: 2939670.

31. Xiao L, Nickbarg E, Wang W, Thomas A, Ziebell M, Prosise WW, et al. Evaluation of in vitro PXR-based assays and in silico modeling approaches for understanding the binding of a structurally diverse set of drugs to PXR. Biochem Pharmacol. 2011;81(5):669-79.

32. Banerjee M, Chen T. Differential regulation of CYP3A4 promoter activity by a new class of natural product derivatives binding to pregnane X receptor. Biochem Pharmacol. 2013;86(6):824-35. PMCID: 3777815.

33. Watkins RE, Maglich JM, Moore LB, Wisely GB, Noble SM, Davis-Searles PR, et al. 2.1 A crystal structure of human PXR in complex with the St. John's wort compound hyperforin. Biochemistry. 2003;42(6):1430-8.

34. Chrencik JE, Orans J, Moore LB, Xue Y, Peng L, Collins JL, et al. Structural disorder in the complex of human pregnane X receptor and the macrolide antibiotic rifampicin. Mol Endocrinol. 2005;19(5):1125-34.

35. Imai YN, Inoue Y, Nakanishi I, Kitaura K. Cl-pi interactions in protein-ligand complexes. Protein Sci. 2008;17(7):1129-37. PMCID: 2442010.

36. Gao J, Xie W. Targeting xenobiotic receptors PXR and CAR for metabolic diseases. Trends Pharmacol Sci. 2012;33(10):552-8. PMCID: 3461088.

37. Evans WE, Relling MV. Pharmacogenomics: translating functional genomics into rational therapeutics. Science. 1999;286(5439):487-91.

38. Bumpus NN. Efavirenz and 8-hydroxyefavirenz induce cell death via a JNK- and BimEL-dependent mechanism in primary human hepatocytes. Toxicol Appl Pharmacol. 2011;257(2):227-34.

39. Mutlib AE, Chen H, Nemeth GA, Markwalder JA, Seitz SP, Gan LS, et al. Identification and characterization of efavirenz metabolites by liquid chromatography/mass spectrometry and high field NMR: species differences in the metabolism of efavirenz. Drug Metab Dispos. 1999;27(11):1319-33.

40. Rodriguez-Antona C, Donato MT, Boobis A, Edwards RJ, Watts PS, Castell JV, et al. Cytochrome P450 expression in human hepatocytes and hepatoma cell lines: molecular mechanisms that determine lower expression in cultured cells. Xenobiotica. 2002;32(6):505-20.

41. Ngan CH, Beglov D, Rudnitskaya AN, Kozakov D, Waxman DJ, Vajda S. The structural basis of pregnane X receptor binding promiscuity. Biochemistry. 2009;48(48):11572-81. PMCID: 2789303.

42. Gao YD, Olson SH, Balkovec JM, Zhu Y, Royo I, Yabut J, et al. Attenuating pregnane X receptor (PXR) activation: a molecular modelling approach. Xenobiotica. 2007;37(2):124-38.

Chapter 5: Mechanisms of Dyslipidemia in Response to the Anti-HIV Drug Efavirenz

Abstract

Efavirenz (EFV) and rilpivirine (RPV) are nonnucleoside reverse transcriptase inhibitors used for the treatment of HIV infection. EFV-based regimens have been observed to increase high-density lipoprotein, low-density lipoprotein and total cholesterol levels, whereas RPV-based regimens exhibit less of an impact on lipid profiles. Dyslipidemia is a risk factor for atherosclerosis and cardiovascular disease and studies investigating the molecular mechanism(s) by which EFV, but not RPV, causes dyslipidemia are lacking. In this work, we have started to probe the mechanism(s) by which EFV, but not RPV, impacts hepatic cholesterol homeostasis using primary mouse hepatocytes.

Introduction

Efavirenz (EFV) is a first generation nonnucleoside reverse transcriptase inhibitor (NNRTI) and is the most widely prescribed antiretroviral for the treatment of HIV infection (Figure 1). Rilpivirine (RPV) is a more recently FDA approved second generation NNRTI that has a flexible diarylpyrimidine structure enabling a greater genetic barrier to viral resistance relative to EFV (Figure 1) (1). Interestingly, EFV-based regimens have been observed to increase high-density lipoprotein, low-density lipoprotein and total cholesterol levels, whereas RPV-based regimens exhibit less of an impact on lipid profiles (2). Dyslipidemia is characterized by the elevation of lipoprotein and total cholesterol levels and is a primary risk factor for developing atherosclerosis and

cardiovascular disease. Studies probing the molecular mechanism(s) by which EFV stimulates the onset of dyslipidemia have yet to be reported.

In preliminary studies, we observed that EFV, but not RPV, increased small heterodimer partner (SHP; NR0B2) mRNA expression in primary mouse hepatocytes. SHP is an orphan nuclear receptor that is basally expressed at low levels in the liver and can be transiently up-regulated through the direct binding of endogenous bile acids to its primary transcriptional regulator FXR (3). Further, SHP has been functionally implicated in a complex FXR-dependent autoregulating signaling cascade for maintaining bile acid and cholesterol homeostasis (3, 4). Activation of this FXR signaling pathway results in the transcriptional repression of CYP7A1, mediated through SHP inhibition of liver receptor homolog-1, a positive regulator of CYP7A1 gene expression (4). CYP7A1 is a member of the cytochromes P450 (P450) family of monooxygenases and is the rate-limiting enzyme in the conversion of cholesterol to bile acids. Interestingly, the overexpression of CYP7A1 in transgenic mice prevented the development of diet-induced hypercholesterolemia and atherosclerosis (5, 6). Additionally, a separate murine model demonstrated that hepatocyte-specific deletion of SHP expression was protective against the development of diet-induced dyslipidemia (7). Taken together, these data suggest that repression of CYP7A1 decreases the rate of cholesterol metabolism and exhibits deleterious effects by promoting the onset of atherosclerosis and dyslipidemia.

In addition to these observations, our laboratory and others have determined EFV to also be extensively metabolized by xenobiotic P450 monooxygenases (8-10). Oxidative metabolism of EFV can result in hydroxylation at the 7, 8 and 14 positions

and, correspondingly, oxidative metabolism of RPV can result in methyl hydroxylation at the 2 and 6 positions (Figure 1). Our laboratory has also demonstrated that the synthetic primary metabolite, 8-hydroxy EFV (8-OHEFV), stimulates hepatotoxicity to a greater extent than EFV through activation of the c-Jun N-terminal kinase signaling pathway (11). This is a key finding in understanding EFV-induced hepatotoxicities as clinical studies have demonstrated 8-OHEFV plasma concentrations exceed that of the parent drug with chronic administration due to autoinduction (12). With these data in mind, a potential role for P450-dependent metabolite activation of the FXR signaling pathway should be taken into consideration as an alternative mechanism through which EFV may disrupt cholesterol and bile acid homeostasis.

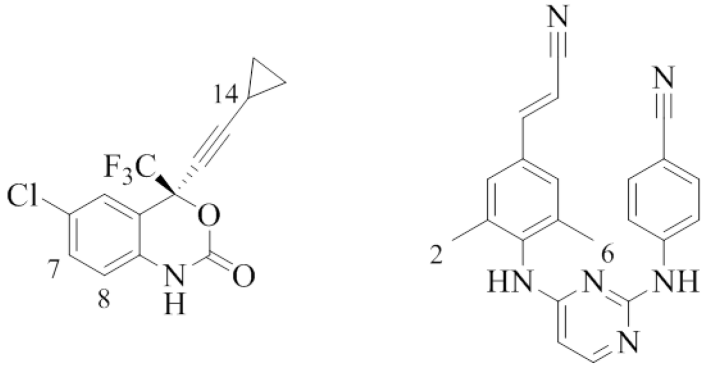

Efavirenz Rilpivirine

Figure 1. Structural comparison of NNRTIs efavirenz and rilpivirine. EFV is a first-generation NNRTI and is the most widely-prescribed antiretroviral to date. RPV is a second-generation NNRTI that has an increased genetic barrier to resistance relative to EFV as well as an improved safety profile. Numbered carbon atoms indicate sites of cytochrome P450-dependent metabolism.

Materials and Methods

EFV and RPV were obtained through the National Institutes of Health AIDS Reagents Program. The c-Jun N-terminal kinase chemical inhibitor SP600125 was purchased from Tocris Bioscience (Avonmouth, Bristol, United Kingdom).

Isolation of primary mouse hepatocytes and drug treatments

Hepatocytes were isolated from 9-13 week-old male C57BL/6J (wild type, WT) mice as well as from 9-13 week-old male farnesoid X receptor knockout ($FXR^{-/-}$) mice bred on a C57BL/6J background and purchased from Jackson Laboratories (Bar Harbor, ME). Hepatocytes were also isolated from mice 9-13 week-old male pregnane X receptor knockout ($PXR^{-/-}$) mice bred on a C57BL/6J background and purchased from Taconic Biosciences (Hudson, NY). Primary mouse hepatocytes were isolated using retrograde liver perfusion with 25 mL 0.5 mM EGTA (Amresco LLC, Solon, OH) prepared in 1X PBS (Thermo Fisher Scientific, Waltham, MA) at 5 mL/min, followed by 25 mL 1X PBS at 5 mL/min, and lastly 20 mL of liver digest medium (Thermo Fisher Scientific) supplemented with 0.15 mg/mL collagenase (Sigma-Aldrich) at 2 mL/min. Following perfusion, livers were removed and cells were gently dissociated in 15 mL of ice-cold hepatocyte wash medium (Thermo Fisher Scientific) using a cell scraper and filtered through a 70 µm nylon mesh cell strainer. Hepatocytes were then pelleted at 50 x *g* for 5 min at 4°C and washed twice with 10 mL hepatocyte wash medium. Cells were resuspended in 25 mL Williams E medium (Thermo Fisher Scientific) with 20 mL percoll (Sigma-Aldrich; 1 part 10X HBSS and 9 parts percoll) and inverted six times prior to pelleting at 300 x *g* for 10 min at 4°C. Hepatocytes were washed with 10 mL

Williams E medium, pelleted at 50 x *g* for 5 min at 4°C, and resuspended in 10 mL Williams E medium supplemented with 10% fetal bovine serum (Thermo Fisher Scientific), 1% L-glutamine (Thermo Fisher Scientific), and 1% penicillin-streptomycin (Sigma-Aldrich). Hepatocytes were plated in six-well collagen-coated plates (Corning, Tewksbury, MA) at a density of 2.4 x 10^5 cells per well for RNA isolation. For assaying lipid droplet formation, hepatocytes were plated in 12-well collagen-coated plated (Corning) at a density of 1.0 x 10^5 cells per well. Cells were incubated overnight at 37°C and 5% CO_2 prior to replacing the cell culture medium with fresh Williams E medium containing 10% fetal bovine serum, 1% L-glutamine, and 1% penicillin-streptomycin for drug treatments. Hepatocytes were treated with either DMSO (0.1%) vehicle or drug over a range of time points. For 48 h and 72 h drug treatments, cell culture medium was replaced every 24 h and hepatocytes were retreated with DMSO or drug. A total of four independent experiments were performed for hepatocytes isolated from WT and $FXR^{-/-}$ mice.

RNA isolation and quantitative real-time PCR (qPCR)

RNA was prepared from primary mouse hepatocytes using TRIzol (Thermo Fisher Scientific) following the manufacturer's instructions for cells grown in a monolayer. Total RNA (1 μg) was reverse transcribed using Maxima First Strand cDNA Synthesis Kit (Thermo Fisher Scientific). The following primers were used for qPCR: Shp forward 5'- TGGGTCCCAAGGAGTATGC-3' and reverse 5'-GCTCCAAGACTTCACACAGTG-3'; Gapdh forward 5'-GAAGGCCGGGGCCCACTTGA-3' and reverse 5'-TCTCCAGGCGGCACGTCAGA-

3'. A Gapdh PCR product was generated from mouse hepatocyte RNA using conventional PCR and ligated into CloneJET PCR cloning kit for subcloning (Thermo Fisher Scientific). Serial dilutions of the resulting Gapdh plasmid were used to generate a standard curve for the quantitation of mRNA levels using Maxima SYBR Green qPCR Master Mix (Thermo Fisher Scientific). Gapdh served as the housekeeping gene for mRNA level normalization. The following qPCR cycling reactions were performed: denaturation of dsDNA for 10 min at 95°C proceeded by 40 cycles of denaturation for 15 sec at 95°C, annealing for 30 sec at 60°C, and extension for 30 sec at 72°C. Resulting Shp copy numbers were normalized by Gapdh for each treatment and data was reported as fold change from DMSO control for each time point.

Oil Red O staining of primary mouse hepatocytes

Intracellular lipid droplet formation was assayed using a steatosis colorimetric assay kit (Cayman Chemical, Ann Arbor, MI). The vendor's protocol was followed for a 12-well format. Following drug treatment, cell medium was aspirated and cells were fixed prior to staining with a 60% Oil Red O solution. After staining, wells were rinsed thoroughly with distilled water. Lipid accumulation was then quantified by incubating cells with the provided lipid droplet assay dye extraction solution. The extracted dye was then transferred to a 96-well plate and the absorbance was read at 490 nm. For qualitative assessment of intracellular distribution of lipid droplets, nuclei were stained with hematoxylin and imaged using a phase contrast microscope.

Statistical Analysis of Data

Results are expressed as means ± standard deviation. Comparisons between experimental conditions were performed using an unpaired one-tailed Student's t-test (GraphPad Prism 6 software). Statistical significances are denoted as: *, $p \leq 0.05$; **, $p \leq 0.01$; ***, $p \leq 0.001$.

Results

EFV, but not RPV, increased Shp mRNA expression in primary mouse hepatocytes

Treatment of primary hepatocytes isolated from WT male mice demonstrated EFV, but not RPV, increased SHP mRNA expression in a time-dependent manner (Figure 2). A 2-fold increase of Shp mRNA expression was observed with 3 h of 10 μM EFV treatment. Increased Shp mRNA levels were sustained with chronic drug treatment resulting in a maximal 3-fold increase relative to DMSO control at 72 h. To test if this mRNA increase was FXR-dependent, hepatocytes were isolated from male mice genetically deficient of the nuclear receptor and treated with 10 μM EFV over a range of time (Figure 3). The 3 h transient increase of Shp mRNA expression previously observed in hepatocytes isolated from WT mice was significantly decreased in EFV treated hepatocytes isolated from $FXR^{-/-}$ mice. With chronic treatment of hepatocytes isolated from $FXR^{-/-}$ mice, however, EFV increased Shp mRNA levels to 2-fold at 72 h.

The c-Jun N-terminal kinase (JNK) stress-activated signaling pathway can transcriptionally modulate Shp in an FXR-independent manner. To test if JNK activation could contribute to the EFV-mediated Shp mRNA expression observed in primary mouse hepatocytes, cells were pre-treated with the JNK-specific chemical inhibitor SP600125

prior to exposing to EFV and assaying for mRNA modulation (Figure 4). Interestingly, SP600125 fully abrogated the increase of Shp mRNA following 3 h of co-treatment with EFV. Although cells were retreated with inhibitor and EFV every 24 h, SP600125 failed to block an increase of Shp mRNA expression following 24, 48 and 72 h of co-treatment.

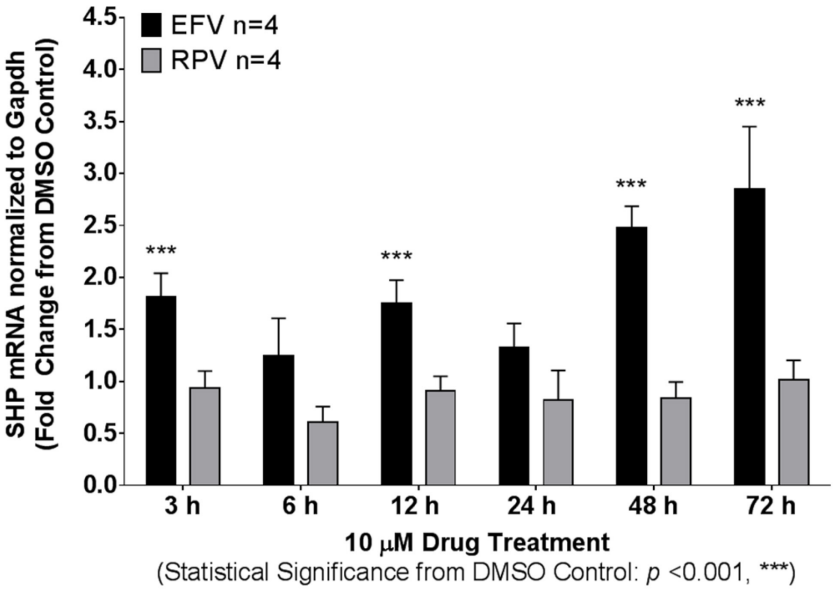

Figure 2. Comparative effects of EFV and RPV on the modulation of Shp mRNA expression in primary mouse hepatocytes. Hepatocytes were isolated from WT male mice and treated for 3, 6, 12, 24, 48 and 72 h with either 0.1% DMSO as vehicle control or 10 μM drug. Following drug treatment, RNA was isolated from hepatocytes using TRIzol. RNA (1 μg) was then reverse transcribed to cDNA for use in qPCR to measure Shp and Gapdh mRNA levels. Data are shown as mean fold change from DMSO control ± S.D. for four independent experiments. Statistical significance from control is shown as ***, $p \leq 0.001$.

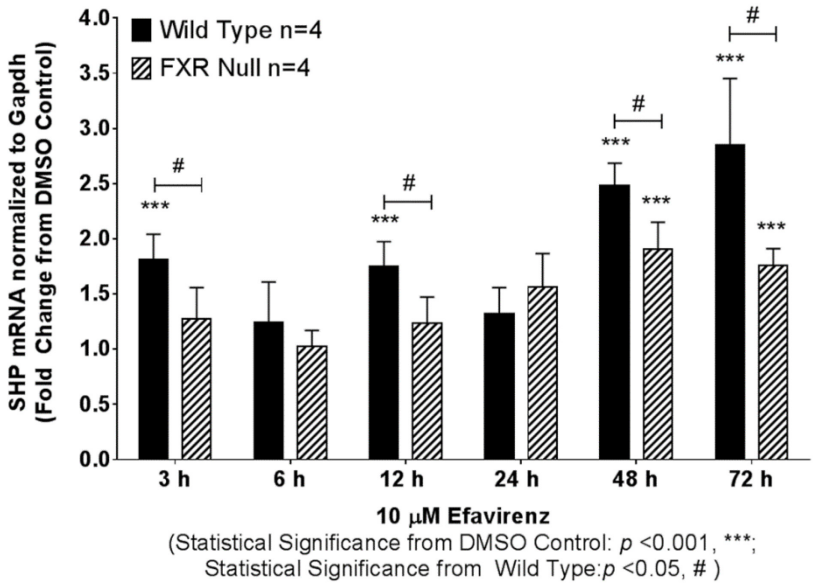

Figure 3. Treatment of hepatocytes isolated from FXR null mice does not fully abrogate EFV-mediated Shp mRNA increase. Hepatocytes were isolated from WT and FXR null male mice and treated for 3, 6, 12, 24, 48 and 72 h with either 0.1% DMSO as vehicle control or 10 μM EFV. Following drug treatment, RNA was isolated from hepatocytes using TRIzol. RNA (1 μg) was then reverse transcribed to cDNA for use in qPCR to measure Shp and Gapdh mRNA levels. Data are shown as mean fold change from DMSO control ± S.D. for four independent experiments. Statistical significance from DMSO control is shown as ***, $p \leq 0.001$ and from WT drug treatment as #, $p \leq 0.05$.

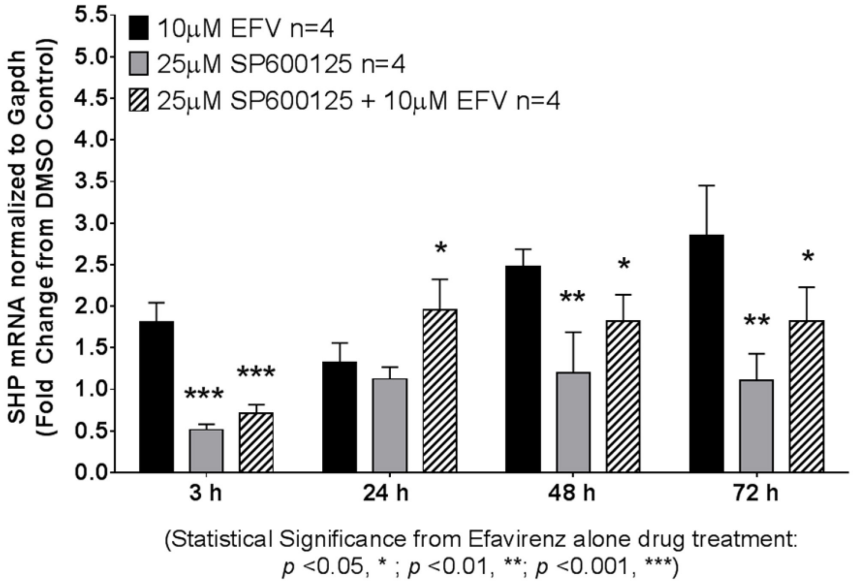

Figure 4. Chemical inhibition of c-Jun N-terminal kinase transiently abolished EFV-mediated Shp mRNA increase. Hepatocytes were isolated from WT male mice and pretreated with the c-Jun N-terminal kinase chemical inhibitor SP600125 (25 μM) for 30 min. Following pre-treatment with inhibitor, cells were then treated with either 0.1% DMSO as vehicle control or 10 μM EFV for 3, 24, 48 and 72 h. Following drug treatment, RNA was isolated from hepatocytes using TRIzol. RNA (1 μg) was then reverse transcribed to cDNA for use in qPCR to measure Shp and Gapdh mRNA levels. Data are shown as mean fold change from DMSO control ± S.D. for four independent experiments. Statistical significance from EFV drug treatment is shown as *, $p \leq 0.05$, **, $p \leq 0.01$ and ***, $p \leq 0.001$.

EFV, but not RPV, promotes lipid droplet formation in primary mouse hepatocytes

In an effort to establish EFV indeed disrupts lipid homeostasis, primary mouse hepatocytes were assayed for lipid droplet formation. EFV (50 μM) caused a significant

increase of lipid droplet formation from control of 2- and almost 3-fold following 48 h and 72 h treatment, respectively (Figure 5A and 5B). A more physiologically relevant concentration of EFV (10 μM) qualitatively increased lipid droplet formation (data not shown), however, this difference was not captured quantitatively due to assay sensitivity limitations. RPV at neither 10 μM nor 50 μM concentrations stimulated lipid droplet formation. Further, chronic treatment of hepatocytes with RPV at 50 μM appeared cause cell death and, at this same concentration, RPV caused an approximate 40% decrease in cell viability relative to control with 72 h treatment (data not shown).

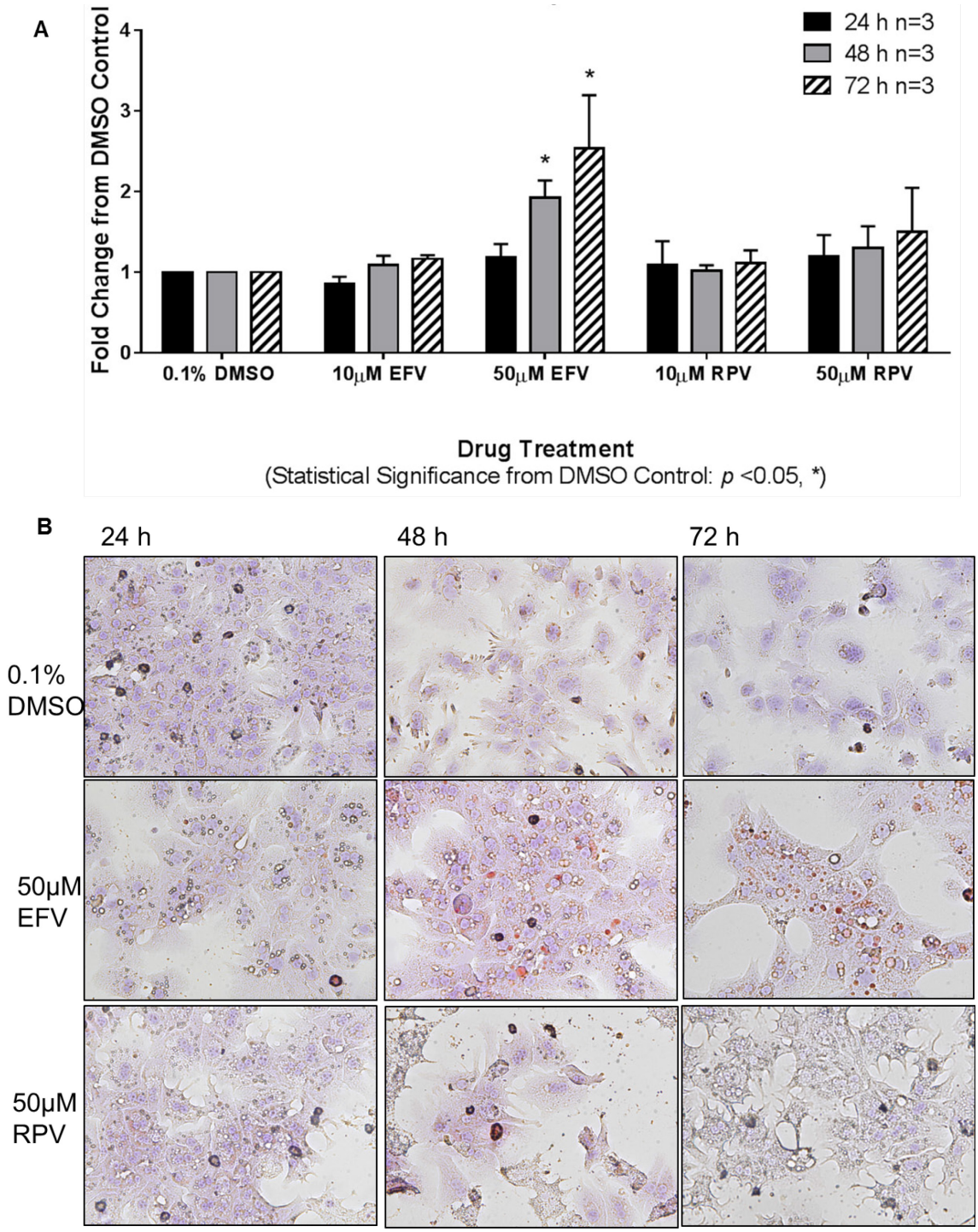

Figure 5. EFV, but not RPV, promotes lipid droplet formation in primary mouse hepatocytes. Intracellular lipid droplet formation was assayed using a steatosis

colorimetric assay kit and lipid droplets were stained using a 60% Oil Red O solution. (A) Lipid accumulation was quantified by extracting Oil Red O and reading the absorbance at 490 nm. (B) For qualitative assessment of intracellular distribution of lipid droplets, nuclei were stained with hematoxylin and imaged using a phase contrast microscope. Data are shown as mean fold change from DMSO control ± S.D. for three independent experiments. Statistical significance from control is shown as *, $p \leq 0.05$.

Future Directions

There are several questions that remain unanswered with this work. Thus far, our data suggests EFV is not a direct activator of FXR. Further, in an effort to take an unbiased approach toward investigating the mechanism by which EFV modulates hepatic cholesterol homeostasis, we tested for lipid droplet formation in hepatocytes isolated from WT male mice. In these experiments, we were excited to see that EFV treatment, but not RPV, resulted in a distinct phenotype of hepatic lipid droplet formation in a time-dependent manner. Although lipid droplets were observed qualitatively in 10 μM EFV treatments, which is approximately equal to steady-state plasma levels with once-daily dosing in humans, the most dramatic phenotype was observed with 72 h treatment of 50 μM EFV. In an attempt to recapitulate this observation in primary human hepatocytes, we performed these treatments in isolates from three individual human donors, yet lipid droplet formation was not observed with EFV treatment suggesting a potential species-specific difference.

That being said, we have begun to probe for potential signaling pathways that could be activated by EFV in mouse hepatocytes resulting in hepatic lipid droplet

formation. For example, chronic pregnane X receptor (PXR) activation has been demonstrated in mice to lead to the disruption of lipid and cholesterol homeostasis. EFV is a strong activator of PXR as we and others have previously demonstrated, however, lipid droplet formation was not abrogated upon chronic treatment of hepatocytes isolated from mice deficient of PXR (Figure 6). Moving forward, it is imperative to test the impact of Shp siRNA knockdown on EFV-mediated lipid droplet formation in primary mouse hepatocytes. If Shp is indeed found to play a causal role in the establishment of this phenotype, then there are several hepatic signaling pathways regulated by Shp that can be further investigated, such as the mevalonate metabolic pathway that produces cholesterol via HMG-CoA reductase, in order to gain mechanistic insight.

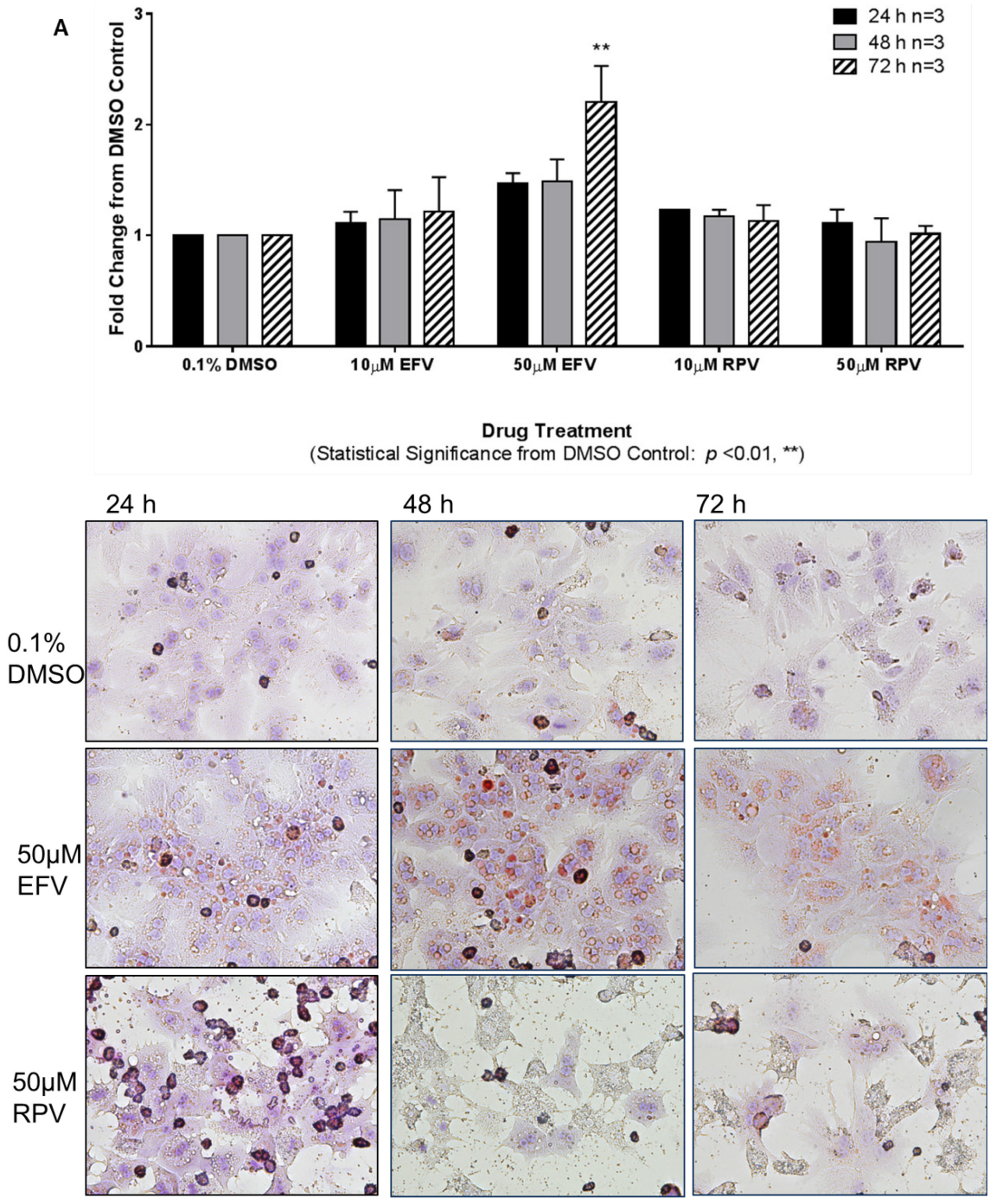

Figure 6. Genetic deficiency of the PXR does not abrogate lipid droplet formation in EFV-treated primary mouse hepatocytes. Intracellular lipid droplet formation was

assayed using a steatosis colorimetric assay kit and lipid droplets were stained using a 60% Oil Red O solution. (A) Lipid accumulation was quantified by extracting Oil Red O and reading the absorbance at 490 nm. (B) For qualitative assessment of intracellular distribution of lipid droplets, nuclei were stained with hematoxylin and imaged using a phase contrast microscope. Data are shown as mean fold change from DMSO control ± S.D. for three independent experiments. Statistical significance from control is shown as *, $p \leq 0.05$.

References

1. Das K, Clark AD, Jr., Lewi PJ, Heeres J, De Jonge MR, Koymans LM, et al. Roles of conformational and positional adaptability in structure-based design of TMC125-R165335 (etravirine) and related non-nucleoside reverse transcriptase inhibitors that are highly potent and effective against wild-type and drug-resistant HIV-1 variants. J Med Chem. 2004;47(10):2550-60.

2. Tebas P, Sension M, Arribas J, Duiculescu D, Florence E, Hung CC, et al. Lipid Levels and Changes in Body Fat Distribution in Treatment-Naive, HIV-1-Infected Adults Treated With Rilpivirine or Efavirenz for 96 Weeks in the ECHO and THRIVE Trials. Clin Infect Dis. 2014;59(3):425-34.

3. Lu TT, Makishima M, Repa JJ, Schoonjans K, Kerr TA, Auwerx J, et al. Molecular basis for feedback regulation of bile acid synthesis by nuclear receptors. Mol Cell. 2000;6(3):507-15.

4. Goodwin B, Jones SA, Price RR, Watson MA, McKee DD, Moore LB, et al. A regulatory cascade of the nuclear receptors FXR, SHP-1, and LRH-1 represses bile acid biosynthesis. Mol Cell. 2000;6(3):517-26.

5. Ratliff EP, Gutierrez A, Davis RA. Transgenic expression of CYP7A1 in LDL receptor-deficient mice blocks diet-induced hypercholesterolemia. J Lipid Res. 2006;47(7):1513-20.

6. Miyake JH, Duong-Polk XT, Taylor JM, Du EZ, Castellani LW, Lusis AJ, et al. Transgenic expression of cholesterol-7-alpha-hydroxylase prevents atherosclerosis in C57BL/6J mice. Arterioscler Thromb Vasc Biol. 2002;22(1):121-6.

7. Hartman HB, Lai K, Evans MJ. Loss of small heterodimer partner expression in the liver protects against dyslipidemia. J Lipid Res. 2009;50(2):193-203.

8. Ogburn ET, Jones DR, Masters AR, Xu C, Guo Y, Desta Z. Efavirenz primary and secondary metabolism in vitro and in vivo: identification of novel metabolic pathways and cytochrome P450 2A6 as the principal catalyst of efavirenz 7-hydroxylation. Drug Metab Dispos. 2010;38(7):1218-29. PMCID: 2908985.

9. Avery LB, VanAusdall JL, Hendrix CW, Bumpus NN. Compartmentalization and antiviral effect of efavirenz metabolites in blood plasma, seminal plasma, and cerebrospinal fluid. Drug Metab Dispos. 2013;41(2):422-9. PMCID: 3558859.

10. Bumpus NN, Kent UM, Hollenberg PF. Metabolism of efavirenz and 8-hydroxyefavirenz by P450 2B6 leads to inactivation by two distinct mechanisms. J Pharmacol Exp Ther. 2006;318(1):345-51.

11. Bumpus NN. Efavirenz and 8-hydroxyefavirenz induce cell death via a JNK- and BimEL-dependent mechanism in primary human hepatocytes. Toxicol Appl Pharmacol. 2011;257(2):227-34.

12. Ngaimisi E, Mugusi S, Minzi OM, Sasi P, Riedel KD, Suda A, et al. Long-term efavirenz autoinduction and its effect on plasma exposure in HIV patients. Clin Pharmacol Ther. 2010;88(5):676-84.

Chapter 6: Discovery of Genetic Variants of the Kinases that Activate Tenofovir in a Compartment-Specific Manner

Abstract

Tenofovir (TFV) is used in combination with other antiretroviral drugs for human immunodeficiency virus (HIV) treatment and prevention. TFV requires two phosphorylation steps to become pharmacologically active; however, the kinases that activate TFV in cells and tissues susceptible to HIV infection have yet to be identified. Peripheral blood mononuclear cells (PBMC), vaginal, and colorectal tissues were transfected with siRNA targeting nucleotide kinases, incubated with TFV, and TFV-monophosphate (TFV-MP) and TFV-diphosphate (TFV-DP) were measured using mass spectrometry-liquid chromatography. Adenylate kinase 2 (AK2) performed the first TFV phosphorylation step in PBMC, vaginal, and colorectal tissues. Interestingly, both pyruvate kinase isozymes, muscle (PKM) or liver and red blood cell (PKLR), were able to phosphorylate TFV-MP to TFV-DP in PBMC and vaginal tissue, while creatine kinase, muscle (CKM) exclusively catalyzed this conversion in colorectal tissue. In addition, next-generation sequencing of the Microbicide Trials Network MTN-001 clinical samples detected 71 previously unreported genetic variants in the genes encoding these kinases. In conclusion, our results demonstrate that TFV is activated in a compartment-specific manner. Further, genetic variants have been identified that could negatively impact TFV activation, thereby compromising TFV efficacy in HIV treatment and prevention.

Introduction

Within the last decade, tenofovir (TFV), prescribed as tenofovir disoproxil fumarate in its prodrug formulation, has emerged as a critical component of antiretroviral combination therapy for the treatment of human immunodeficiency virus (HIV) (1, 2). More recently, oral as well as vaginal and rectal microbicide gel preparations of TFV have been investigated for use in pre-exposure prophylaxis (PrEP) as an HIV prevention strategy for individuals at high-risk of viral exposure (3-5). TFV is a drug desirable candidate for PrEP due to the long half-life of active drug TFV-diphosphate (TFV-DP) reported to be 53 h in vaginal tissue homogenate and up to 139 h in vaginal CD4+ cells following an oral dosing of HIV-uninfected women (6, 7). That being said, there has been discrepancy in the prophylactic effect observed for TFV-based regimens. For example, the Partners in Prevention study demonstrated a 67-75% reduction in HIV acquisition in serodiscordant heterosexual couples, iPrEx demonstrated a 44% reduction in men or transgender women who have sex with men, and FEM-PrEP and VOICE trials showed no significant reduction in the rate of infection in heterosexual women (8-10). This disparity has been primarily due to poor adherence. Adjusting for adherence, the differences among these clinical trials has been attributed to the increased accumulation of active drug in colon versus vaginal tissue. As such, these findings suggest that the enzymes responsible for TFV activation may differ between colon and vaginal tissue, however, this has not been tested thus far. Further, while yet to be explored, it can be envisioned that genetic variation in the nucleotide kinases that activate TFV could underlie observed

inter-individual differences in tissue TFV-DP concentrations that has been noted even when adherence is high (7, 11, 12).

As TFV requires phosphorylation by nucleotide kinases in order to become pharmacologically active, both local mucosal tissue cell phosphorylation and distant peripheral blood CD4+ cell phosphorylation with secondary migration to mucosal tissue may be critical in achieving effective TFV-DP concentrations. If mucosal tissue phosphorylation is an essential contribution to mucosal tissue cell TFV-DP concentrations, then the kinases responsible for TFV transformation are expressed in cells and tissues associated with HIV infection (2, 13). To date, the expression profiles of nucleotide kinases in peripheral blood mononuclear cells (PBMC), vaginal tissue, and colorectal tissue have not been characterized and data demonstrating kinase activity towards TFV and TFV-MP are lacking. In vitro studies using human T-lymphoid cells demonstrated the mitochondrial and cytosolic enzyme adenylate kinase isoform 2 (AK2) could catalyze the phosphorylation of TFV to form TFV-monophosphate (TFV-MP) (14-16). Experimental evidence is deficient, however, with regards to the nucleotide kinase(s) capable of transforming TFV-MP to TFV-DP. TFV-MP has been reported as a substrate of NME/NM23 nucleoside diphosphate kinase 1 (NME1) as this enzyme demonstrates broad activity towards purine nucleoside diphosphates (2, 17). Yet, in separate studies, NME1 exhibited low to non-detectable rates of catalysis, while creatine kinase, muscle (CKM) efficiently phosphorylated TFV-MP and minor catalytic efficiency towards TFV-MP was demonstrated by rabbit pyruvate kinase, muscle (PKM) (18, 19). Nevertheless, although these kinases exhibit activity towards TFV or TFV-MP using in vitro model

systems, whether or not they are expressed in cells and tissues susceptible to HIV infection is unknown.

In the present study, we characterized nucleotide kinase expression in PBMC, vaginal tissue, and colorectal tissue in order to identify those that catalyze the phosphorylation of TFV to TFV-MP and TFV-MP to TFV-DP. Towards this end, we knocked down the protein expression of AK2, CKM, PKM, pyruvate kinase, liver and red blood cell (PKLR), and guanylate kinase 1 (GUK1) using siRNA. Neither PKLR nor GUK1 have been previously reported to activate TFV; however, PKLR exhibits an approximate 70% amino acid sequence identity to the isozyme PKM and GUK1 has been demonstrated to phosphorylate the antiviral drug adefovir which is structurally similar to TFV.(20) Taking these studies a step further, we wanted to leverage our identification of the nucleotide kinases that activate TFV and test for the existence of genetic variants in *AK2*, *CKM*, *PKM*, and *PKLR*. To do so, we performed next-generation targeted sequencing of genomic DNA isolated from the plasma of 142 HIV-uninfected female participants of the Microbicide Trials Network study MTN-001 (11). In this work, we have demonstrated at an enzymatic level that TFV is activated in a tissue-specific manner. We also put forth an innovative concept that variation in the genes that encode the nucleotide kinases that activate TFV may contribute to inter-individual differences observed clinically. Taken together, these findings represent a shift in thinking about the factors that govern variability in TFV efficacy and pharmacokinetics.

Materials and Methods

siRNA knockdown of nucleotide kinases

PBMC were obtained from Bioreclamation (Westbury, NY), and fresh vaginal and colorectal biopsies were obtained from the Johns Hopkins University School of Medicine Tissue Bank (Baltimore, MD). Donor information is as follows: PBMC (n=3; 38 y.o. male, 24 y.o. female, and 27 y.o. female); vaginal tissue (n=3; 31 y.o. female, 48 y.o. female, and 37 y.o. female); colorectal tissue (n=3; 35 y.o. male, 39 y.o. female, 42 y.o. male). All donors were healthy, HIV-uninfected individuals. Nucleotide kinases were knocked down using siGENOME siRNA (Dharmacon, GE Healthcare Life Sciences, Lafayette, CO). PBMC and tissues transfected with non-targeting siRNA were used as controls. For transfection of PBMC, a Neon™ Transfection System (Life Technologies, Fredrick, MD) was used. Electroporation conditions were as follows: pulse voltage 2100 V, pulse width 15 ms, 1 pulse, 1 x 10^6 cells, and 500 nM siRNA. For tissue electroporation, a total of 5 mg of tissue was used for a single electroporation. The tissues were electroporated in 0.4 cm cuvettes (Bio-Rad, Hercules, CA) using a Gene Pulser Xcell™ electroporater (Bio-Rad). A square waveform (500 V and 10 ms) and 500 nM of siRNA was used.

Immunoblotting of nucleotide kinases

Following electroporation, tissues were cultured for 24 h and PBMC for 48 h in DMEM supplemented with 10% FBS prior to homogenization. For immunoblots, 10 μg of homogenized cells and tissues were resolved by SDS-PAGE gel electrophoresis. Proteins were transferred onto a nitrocellulose membrane and blotted with AK2, CKM,

PKM, PKLR, and GUK1 antibodies (Thermo Fisher Scientific, Waltham, MA). Anti-β-actin was used for normalization (Cell Signaling, Danvers, MA).

Detection of TFV, TFV-MP, and TFV-DP using ultra-high performance liquid chromatography-tandem mass spectrometry

TFV (10 μM; NIH AIDS Reagent Program) was added to the culture medium 24 h (for vaginal and colorectal tissues) or 48 h (for PBMC) after electroporation with siRNA. Following 12 h of incubation with TFV, the tissues and cells were harvested and homogenized in 70% methanol. Samples were centrifuged for 10 min at 1,500 x g at 4ºC and the supernatant was dried under vacuum. An ultra-high performance liquid chromatography-tandem mass spectrometry (uHPLC-MS/MS) assay was developed for the quantification of TFV, TFV-MP, and TFV-DP using a Dionex Ultimate 3000 uHPLC system coupled to a TSQ Vantage Triple Stage Quadrupole mass spectrometer (Thermo Fisher Scientific). Analytes were separated using a Hypersil GOLD-C18 column (3 μm, 100 mm x 1 mm, Thermo Fisher Scientific) at a flow rate of 0.05 mL/min. Solvent A was 2 mM ammonium phosphate (Thermo Fisher Scientific) with 3 mM hexylamine (Thermo Fisher Scientific) in water, pH 9.2, and solvent B was acetonitrile (Thermo Fisher Scientific). The gradient used is as follows: 9% B from 0 to 0.5 min, 9% B to 60% B from 0.5 to 15.5 min, 60% B to 9% B from 15.5 to 15.6 min, and held at 9% B until 29.6 min. In selected reaction monitoring mode, fragment ions were detected by positive ionization using the following transitions (Q1→Q3): TFV (*m/z* 288→176), TFV-MP (*m/z* 368→270), and TFV-DP (*m/z* 448→270). Dried cell and tissue extracts were reconstituted in 100 μL mobile phase A for uHLPC-MS/MS analysis.

Clinical samples

Plasma was obtained from HIV-uninfected females (n=142) enrolled in the Microbicide Trials Network study MTN-001 across seven study sites: Umkomaas and Botha's Hill, Durban, South Africa; Makerere University-Johns Hopkins University Research Collaboration, Kampala, Uganda; Case Western Reserve University in Cleveland, OH, United States of America (USA); University of Pittsburgh, Pittsburgh, PA, USA; University of Alabama at Birmingham, Birmingham, AL, USA; Bronx-Lebanon Hospital Center, New York City, NY, USA (11). The current analysis was approved by the Johns Hopkins Medicine IRB (NA_00016287).

Genomic DNA isolation

Genomic DNA was isolated from 200 µL of plasma using the GeneJET Whole Blood Genomic DNA Purification Mini Kit (Thermo Fisher Scientific, Waltham, MA). Purified DNA was eluted using 50 µL of elution buffer.

Sample preparation for Next-generation sequencing

Samples were prepared following the TSCA library preparation guide using 50 ng of template DNA per reaction. Agencourt AMPure XP beads (Beckman Coulter, Inc., Brea, CA) were used for PCR clean-up and library normalization was performed according to the TSCA protocol. The final pooled DNA library (6 µL) was diluted in 594 µL HT1 buffer and spiked with 1% PhiX. One technical control was included per sample batch and runs were sequenced using an Illumina MiSeq sequencing platform generating 150 bp paired-end reads.

Next-generation sequencing targeted enrichment design

Sequencing was performed using the Illumina TruSeq custom amplicon v1.5 kit (San Diego, CA). Custom probes targeting the exonic regions of *AK2*, *CKM*, *PKM*, and *PKLR* were generated in silico using Illumina DesignStudio software. The chromosomal coordinates used were as follows: *AK2* 1:33473531 – 1:33502522; *CKM* 19:45809661 – 19:45826243; *PKM* 15:72492805 – 15:72523694; *PKLR* 1:155259074 – 1:155271235. The final design included 102 amplicons. All genetic variants reported in this study have been submitted to the SNP database under the submitter handle "BUMPUSLAB."

Next-generation sequencing data analysis

Secondary analysis of the base calls and Phred-like quality score (Qscore) generated by Real Time Analysis software was performed using on-instrument MiSeq Reporter software. Reads were mapped to the GRCh37 (hg19) reference assembly using a banded Smith-Waterman algorithm and variant calling was carried out using the Genome Analysis Toolkit. Variant call format files were annotated using Illumina VariantStudio software. Raw variant calls were filtered applying a coverage threshold > 30X, a minimum base call Qscore of 30, and an alternate variant frequency > 20%. Variants were cross-referenced with the National Center for Biotechnology Information database of Single Nucleotide Polymorphisms. The phenotypic consequence of missense variants was assigned using (sorts intolerant from tolerant substitutions; J. Craig Venter Institute online tool) and PolyPhen (polymorphism phenotyping; Harvard University online tool) in silico prediction tools where amino acid substitutions were scored. A SIFT score < 0.05 was suggestive of a damaging amino acid substitution and > 0.05 a tolerated

substitution, whereas a PolyPhen score > 0.908 was suggestive of a probably damaging, 0.447-0.908 a possibly damaging, or < 0.447 a benign amino acid substitution (21, 22).

Statistical Analysis

Statistical analyses were performed using GraphPad Prism (San Diego, CA). Two-tailed unpaired *t* tests were performed and significance was denoted as follows: *, $p \leq 0{\cdot}05$; **, $p \leq 0{\cdot}01$; ***, $p \leq 0{\cdot}001$.

Results

Nucleotide kinase activation of TFV in cells and tissues susceptible to HIV infection

In order to identify the nucleotide kinases that activate TFV in PBMC, vaginal, and colorectal tissue, we delivered siRNA targeted to AK2, GUK1, PKM, PKLR, and CKM to cells and tissues followed by incubation with TFV to test the impact on drug activation. The experiments described herein were performed in cells and tissues from healthy, HIV-uninfected donors that were not administered TFV. Candidate kinases were screened using immunoblotting in order to test for their expression in PBMC, vaginal, and colorectal tissues shown in Figure 1. The non-targeting, or no target, siRNA lane in the representative immunoblot is commensurate with basal expression of each kinase in PBMC, colon, and vaginal tissues, respectively. We found that AK2, which has been previously reported to catalyze the phosphorylation of TFV to TFV-MP, was expressed ubiquitously in the cells and tissues investigated in this study. A similar protein expression profile was observed for the nucleotide kinase GUK1. Interestingly, of the candidates examined for the transformation of TFV-MP to TFV-DP, PKM and PKLR were detectable in both PBMC and vaginal tissue, while basal expression of either

isoenzyme was not detectable in colorectal tissue using immunoblot analyses. In contrast, CKM was observed to be exclusively expressed in colorectal tissue and not detectable at the protein level in PBMC or vaginal tissue. It is important to note that NME1, which has been reported to transform TFV-MP to TFV-DP with weak catalytic efficiency, was not detectable at the protein level in PBMC, vaginal tissue, or colorectal tissue (data not shown).

Guided by our preliminary findings, siRNA was used to knockdown the following nucleotide kinases AK2, GUK1, PKM, and PKLR in PBMC (n=3), AK2, GUK1, and CKM in colorectal tissue (n=3), and AK2, GUK1, PKM, and PKLR in vaginal tissue (n=3). Decreased expression of each targeted kinase was evaluated by immunoblot analysis relative to the non-targeting siRNA control (Figure 1). The intracellular formation of TFV metabolites was detected using uHPLC-MS/MS and the impact of enzyme loss-of-function on TFV-MP and TFV-DP formation following incubation with TFV are shown as bar graphs in Figure 1. When AK2 was knocked down, TFV-MP decreased to 17 ± 1.4% (17/100 ± 1.4/100), 9.5 ± 1.1% (9.5/100 ± 1.1/100), and 12 ± 1.5% (12/100 ± 1.5/100; p-value = 3.4E-6, 3.6E-5, and 7.2E-5) of the non-targeting siRNA control in PBMC, colorectal tissue, and vaginal tissue, respectively. Knockdown of AK2 protein expression also resulted in a decrease of TFV-DP to 13 ± 1.7% (13/100 ± 1.7/100), 15 ± 2.3% (15/100 ± 2.3/100), and 9 ± 2.2% (9/100 ± 2.2/100; p-value = 3.9E-6, 4.5E-6, and 2.7E-5) of non-targeting control in PBMC, colorectal tissue, and vaginal tissue, respectively. Knockdown of PKM decreased TFV-DP to 33 ± 5.8% (33/100 ± 5.8/100) and 27 ± 4.3% (27/100 ± 4.3/100; p-value = 2.7E-5 and 8.2E-5) of control in

PBMC and vaginal tissue, respectively. Additionally, knockdown of PKLR decreased TFV-DP to 78 ± 6.6% (78/100 ± 6.6/100) and 81 ± 7.4% (81/100 ± 7.4/100; p-value = 0.008 and 0.017) of control in PBMC and vaginal tissue, respectively. When CKM was knocked down in colorectal tissue, TFV-DP was decreased to 8 ± 2.9% (8/100 ± 2.9/100; p-value = 2.2E-5) of control. The observed tissue-specific activation of TFV has been summarized in Figure 2.

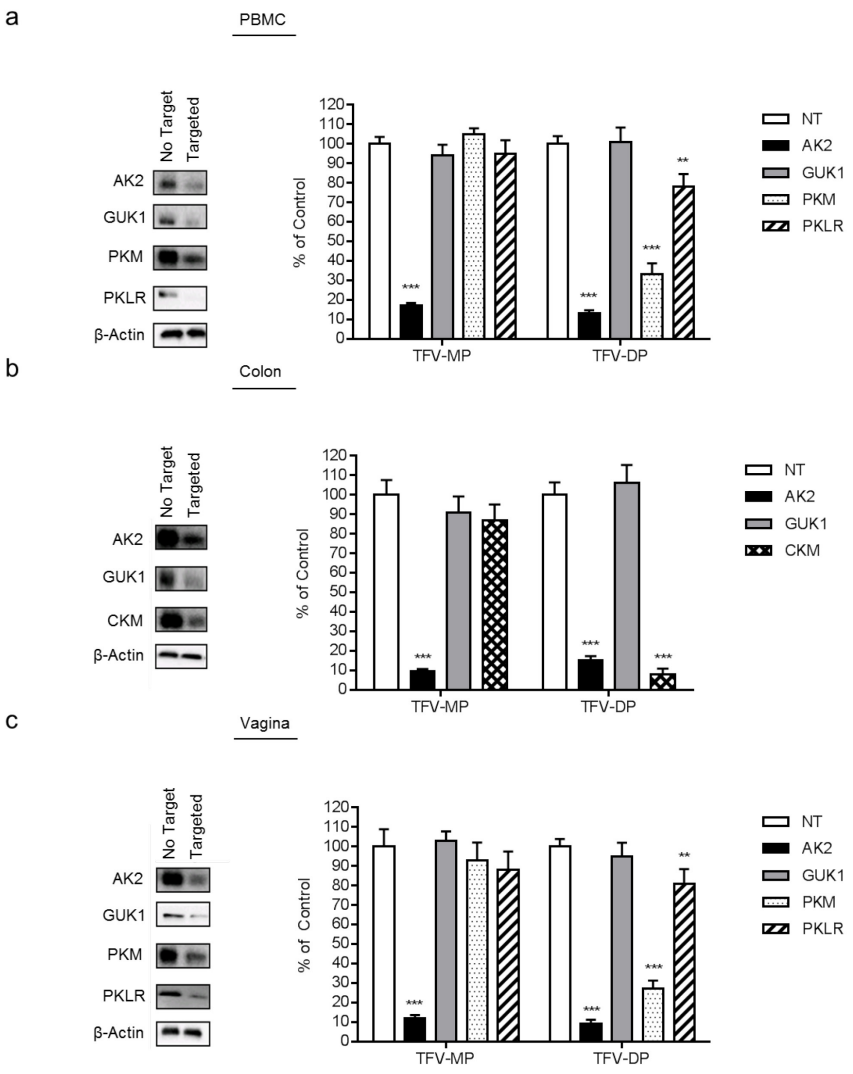

Figure 1. Targeted siRNA knockdown of nucleotide kinases in PBMC, colorectal tissue, and vaginal tissue and the resulting impact on TFV-MP and TFV-DP intracellular formation. PBMC, colorectal tissue, and vaginal tissue were electroporated with 500nM non-targeting siRNA or siRNA targeting AK2, GUK1, PKM, PKLR, and CKM and incubated for 24 h or 48 h for tissue or PBMC, respectively. Representative immunoblots demonstrate decreased nucleotide kinase expression with each targeted

siRNA treatment relative to the non-targeting siRNA control. siRNA treated (A) PBMC, (B) colorectal tissue, and (C) vaginal tissue were incubated with 10 μM TFV for 12 h (n=3 per treatment). Intracellular anabolites were extracted from which TFV-MP and TFV-DP were detected using uHPLC-MS/MS as depicted in the corresponding bar graphs showing mean ± standard deviation for each treatment. Statistical analyses were performed using a two-tailed unpaired *t* test to compare relative levels of anabolite production between non-targeted and targeted siRNA conditions; * = $p \leq 0.05$; ** = $p \leq 0.01$; *** = $p \leq 0.001$.

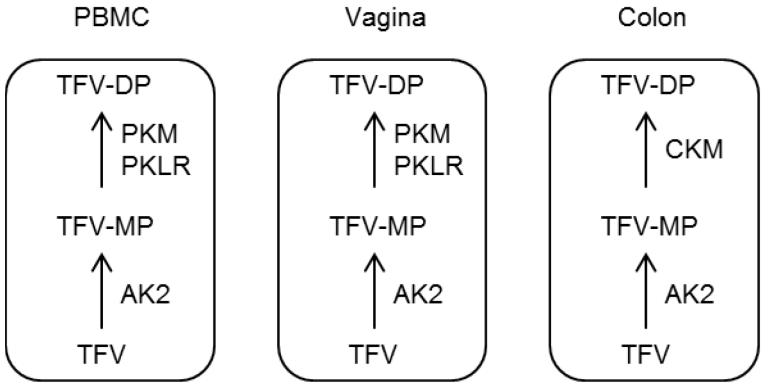

Figure 2. Schematic summarizing the intracellular activation of the antiretroviral drug TFV in cells and tissues susceptible to HIV infection. AK2 can transform TFV to TFV-MP in PBMC, colorectal, and vaginal tissues. PKM and PKLR can transform TFV-MP to the active anabolite TFV-DP in PBMC and vaginal tissue, while CKM can transform TFV-MP to TFV-DP in colorectal tissue.

MTN-001 participant demographics and ethnicities

For this retrospective study, we obtained plasma from 142 of the total 144 participants of the Microbicide Trials Network study MTN-001, and their demographics

and self-identified ethnicities are summarized in Table 1. An approximate half of these participants were enrolled at the United States study sites (USA; n=72) and the remaining participants were enrolled at either the South Africa (SA; n=46) or Uganda (UGA; n=24) study sites.

MTN-001 participant demographics and ethnicities n = 142		
Study site	Self-identified ethnicity	n (% of n)
USA		72
	African American	35 (49)
	European American	32 (44)
	Asian	2 (3)
	Multi-ethnic	2 (3)
	Hispanic	1 (1)
SA		46
	African	37 (80)
	Asian	5 (11)
	Multi-ethnic	3 (7)
	Bhaca	1 (2)
UGA		24
	African	24 (100)

Table 1. MTN-001 participant demographics and self-identified ethnicities. Plasma samples were obtained from 142 HIV-uninfected female participants of the MTN-001 clinical trial for genomic DNA isolation. Participants were enrolled in study sites across the United States (USA; n=72), South Africa (SA; n=46), and Uganda (UGA; n=24).

Next-generation sequencing of MTN-001 clinical samples

In order to test for the existence of genetic variants within the nucleotide kinases that activate TFV, we designed a targeted assay to sequence the exonic regions of *AK2*, *CKM*, *PKM*, and *PKLR*. Of the 142 MTN-001 participants sequenced in this study, we

observed 57 subjects (40%, 57/142) to carry single-base variations or deletions in their DNA that may result in a mutation at the amino acid level. Though this assay was targeted to exonic regions, we detected genetic variation within flanking intronic regions as well. The distribution of the variants and deletions detected for each kinase are depicted using a Venn diagram in Figure 3. In 40 participants, we observed genetic variants within only one nucleotide kinase, while 17 individuals carried variants within two (n=16) or three (n=1) nucleotide kinases.

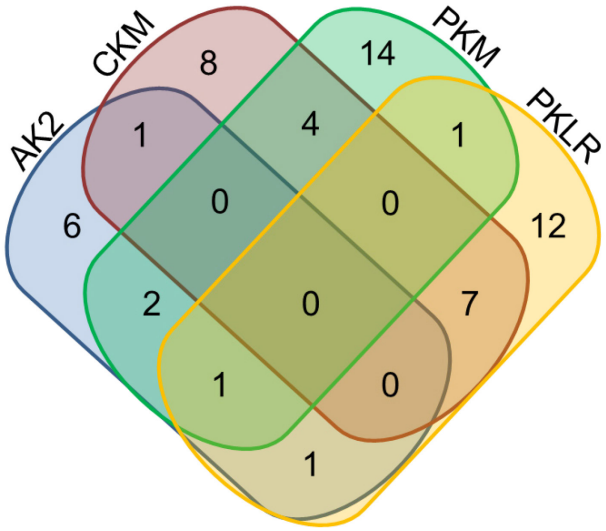

Figure 3. Distribution of nucleotide kinase genetic variants detected in 57 MTN-001 participants. Each colored oval is representative of a nucleotide kinase *AK2* (blue), *CKM* (red), *PKM* (green), and *PKLR* (yellow). Non-overlapping regions demonstrate the number of participants observed to carry single nucleotide variants (SNVs) and deletions within only one gene (n=40; *AK2* n=6, *CKM* n=8, *PKM* n=14, *PKLR* n=12). Overlapping regions demonstrate the number of participants that were observed to carry SNVs and deletions in more than one gene (n=17). For example, moving down the left-hand side of

the diagram, six participants carried *AK2* genetic variants alone, two participants carried variants for *AK2* and *PKM*, one participant carried variants for *AK2*, *PKM*, and *PKLR*, and one participant carried variants for *AK2* and *PKLR*.

Targeted sequencing of *AK2*

A total of 12 previously unreported single nucleotide variants (SNVs) and deletions that may impact the protein-coding potential of the *AK2* mRNA transcript were detected in 11 participants, six enrolled in USA study sites, two in SA, and three in UGA. Of the detected *AK2* variants, seven missense variants, which cause a mutation at the amino acid level for the encoded protein, were detected in seven heterozygous individuals at a frequency of one individual per variant (Table 2). Using in silico tools, three of the observed missense variants were predicted to have a deleterious and damaging impact on protein function with a frequency of 2% (3/142 individuals).

Study site	Ethnicity	AK2 variant (ref. > alt.)	cDNA position	Coding DNA sequence position	Protein position	Amino acid (ref. > alt.)	Exon	SIFT prediction	PolyPhen prediction
USA	African American	A > G	249	166	56	S > P	2/6	Deleterious (0.02)	Probably damaging (0.95)
USA	European American	T > C	451	368	123	D > G	4/6	Deleterious (0)	Possibly damaging (0.452)
SA	African	A > G	511	428	143	L > P	5/6	Deleterious (0)	Probably damaging (1)
SA	African	G > A	516	433	145	H > Y	5/6	Deleterious (0)	Probably damaging (1)
USA	African American	A > G	583	500	167	I > T	6/6	Deleterious (0.03)	Possibly damaging (0.632)
UGA	African	T > A	622	539	180	E > V	6/6	Tolerated (0.27)	Benign (0.009)
UGA	African	G > T	743	660	220	F > L	6/6	Tolerated (0.08)	Benign (0.079)

Table 2. *AK2* missense variants detected in MTN-001 participants. A total of seven previously unreported *AK2* missense variants were detected in seven heterozygous MTN-001 participants for the coding DNA reference sequence NM_001625.3. The functional consequence of resulting amino acid mutations were predicted using SIFT and PolyPhen in silico tools. A SIFT score < 0.05 was suggestive of a damaging amino acid substitution and > 0.05 a tolerated substitution. A PolyPhen score > 0.908 was suggestive of a probably damaging, 0.447-0.908 a possibly damaging, or < 0.447 a benign amino acid substitution. Deleterious and probably damaging *AK2* missense variants was observed at a frequency of 2% (3/142 individuals).

Targeted sequencing of *CKM*

A total of 18 previously unreported SNVs and deletions that may impact the protein-coding potential of the *CKM* mRNA transcript were detected in 17 participants, eight enrolled in USA study sites, four in SA, and five in UGA. Of the detected SNVs, 15 heterozygous participants were found to carry 15 *CKM* missense variants with a frequency of one individual per variant (Table 3). Using in silico tools, four of the observed missense variants were predicted to have a deleterious and damaging impact on protein function with a frequency of 3% (4/142 individuals). Further, the following reference single nucleotide polymorphism (SNP) missense variants rs11559024 (NM_001824.4:c.248T>C) and rs17357122 (NM_001824.4:c.497G>A) were detected in two heterozygous USA participants (one individual per variant), and rs17875625 (NM_001824.4:c.728C>A) was detected in one heterozygous SA participant. Of the detected reference SNPs, only rs17875625 was predicted to have a deleterious and damaging impact on protein function.

Study site	Ethnicity	CKM variant (ref. > alt.)	cDNA position	Coding DNA sequence position	Protein position	Amino acid (ref. > alt.)	Exon	SIFT prediction	PolyPhen prediction
USA	European American	A > G	419	244	82	Y > H	3/8	Deleterious (0.02)	Possibly damaging (0.474)
USA	African American	T > C	435	260	87	E > G	3/8	Deleterious (0.04)	Possibly damaging (0.467)
SA	African	C > T	462	287	96	R > H	3/8	Tolerated (0.07)	Probably damaging (0.976)
UGA	African	G > A	464	289	97	H > Y	3/8	Deleterious (0)	Probably damaging (0.985)
UGA	African	C > T	564	389	130	R > H	4/8	Deleterious (0)	Probably damaging (0.966)
USA	European American	C > T	674	499	167	G > S	5/8	Deleterious (0.01)	Benign (0.307)
SA	African	A > G	680	505	169	F > L	5/8	Tolerated (1)	Benign (0.003)
USA	African American	A > G	692	517	173	Y > H	5/8	Deleterious (0)	Possibly Damaging (0.725)
USA	Hispanic	C > T	758	583	195	D > N	5/8	Tolerated (0.06)	Benign (0.099)
UGA	African	G > C	779	604	202	L > V	5/8	Deleterious (0.03)	Possibly damaging (0.878)
UGA	African	T > A	969	794	265	K > M	7/8	Deleterious (0)	Possibly damaging (0.799)
USA	African American	T > C	981	806	269	H > R	7/8	Tolerated (0.27)	Benign (0.002)
SA	African	A > T	1080	905	302	L > Q	7/8	Deleterious (0)	Probably damaging (0.919)
USA	African American	A > G	1125	950	317	L > P	7/8	Deleterious (0)	Probably damaging (0.999)
USA	European American	T > C	1280	1105	369	K > E	8/8	Tolerated (0.1)	Benign (0.001)

Table 3. *CKM* missense variants detected in MTN-001 participants. A total of 15 previously unreported *CKM* missense variants were detected in 15 heterozygous MTN-001 participants for the coding DNA reference sequence NM_001824.4. The functional consequence of resulting amino acid mutations were predicted using SIFT and PolyPhen in silico tools. A SIFT score < 0.05 was suggestive of a damaging amino acid substitution and > 0.05 a tolerated substitution. A PolyPhen score > 0.908 was suggestive of a probably damaging, 0.447-0.908 a possibly damaging, or < 0.447 a benign amino acid substitution. Deleterious and probably damaging *CKM* missense variants was observed at a frequency of 3% (4/142 individuals).

Targeted sequencing of *PKM*

A total of 19 previously unreported SNVs and deletions that may impact the protein-coding potential of the *PKM* mRNA transcript were detected in 19 participants, nine enrolled in USA study sites, five in SA, and five in UGA. Of the detected SNVs, 14 *PKM* missense variants were detected in 14 heterozygous participants at a frequency of one individual per variant (Table 4). In silico tools were unable to predict the functional impact of the observed missense variants due to the lack of sequence diversity required for the performed multiple sequence alignments. In addition to the observed *PKM* SNVs, three heterozygous USA participants (one individual per variant) were found to carry the following reference SNPs: stop gained variants rs180716407 (NM_001206796.1:c.14G>C) and rs151078084 (NM_001206796.1:c.1354G>A) and the missense variant rs147939689 (NM_001206796.1:c.389C>A).

Study site	Ethnicity	PKM variant (ref. > alt.)	cDNA position	Coding DNA sequence position	Protein position	Amino acid (ref. > alt.)	Exon
USA	African American	C > T	643	244	82	A > T	3/12
USA	Asian	G > C	753	354	118	N > K	3/12
SA	African	T > A	754	355	119	T > S	3/12
USA	European American	A > T	919	520	174	S > T	5/12
SA	African	A > T	1052	653	218	L > Q	6/12
UGA	African	T > C	1103	704	235	Y > C	6/12
UGA	African	C > A	1483	1084	362	D > Y	8/12
USA	Multiracial	T > C	1489	1090	364	I > V	8/12
UGA	African	C > T	1600	1201	401	A > T	8/12
UGA	African	T > C	1628	1229	410	K > R	9/12
USA	African American	T > G	1642	1243	415	T > P	9/12
SA	Asian	C > T	1820	1421	474	R > Q	10/12
UGA	African	C > T	1897	1498	500	A > T	10/12
USA	European American	T > C	2114	1715	572	K > R	12/12

Table 4. *PKM* missense variants detected in MTN-001 participants. A total of 14 previously unreported *PKM* missense variants were detected in 14 heterozygous MTN-001 participants for the coding DNA reference sequence NM_001206796.1. SIFT and PolyPhen in silico tools could not predict the functional impact of the observed missense variants with a high degree of confidence due to the lack of sequence diversity that is required for the performed multiple sequence alignments.

Targeted sequencing of *PKLR*

A total of 22 previously unreported SNVs and deletions that may impact the protein-coding potential of the *PKLR* mRNA transcript were detected in 21 participants, 14 enrolled in USA study sites, four in SA, and three in UGA. Of the observed SNVs, 15 *PKLR* missense variants were detected in 15 heterozygous participants at a frequency of one individual per variant (Table 5). Using in silico tools, four of the detected missense variants were predicted to have both a deleterious and damaging impact on protein function with a frequency of 3% (4/142 individuals). The reference SNP missense variant missense variant rs147689373 (NM_000298.5:c.829C>T) was detected in one heterozygous SA participant.

Study site	Ethnicity	PKLR variant (ref. > alt.)	cDNA position	Coding DNA sequence position	Protein position	Amino acid (ref. > alt.)	Exon	SIFT prediction	PolyPhen prediction
SA	African	C > T	128	89	30	G > E	1/11	Deleterious (0.01)	Probably damaging (0.995)
SA	African	A > T	206	167	56	F > Y	2/11	Tolerated (0.29)	Benign (0.075)
USA	African American	T > A	251	212	71	E > V	2/11	Deleterious (0)	Probably damaging (0.919)
USA	African American	A > T	277	238	80	S > T	2/11	Tolerated (0.19)	Benign (0.087)
UGA	African	A > G	287	248	83	V > A	2/11	Tolerated (0.97)	Benign (0.001)
USA	African American	A > T	337	298	100	S > T	3/11	Tolerated (0.06)	Benign (0.32)
USA	European American	C > T	386	347	116	R > Q	3/11	Deleterious (0)	Probably damaging (0.996)
USA	Hispanic	G > A	674	635	212	P > L	5/11	Deleterious (0.03)	Benign (0.094)
USA	African American	T > C	730	691	231	I > V	5/11	Tolerated (0.86)	Benign (0.002)
USA	African American	C > T	814	775	259	V > M	6/11	Deleterious (0.03)	Possibly damaging (0.892)
UGA	African	T > C	908	869	290	K > R	6/11	Tolerated (0.24)	Possibly damaging (0.879)
USA	European American	G > T	990	951	317	H > Q	6/11	Tolerated (0.98)	Possibly damaging (0.577)
USA	African American	C > T	1066	1027	343	E > K	7/11	Deleterious (0)	Probably damaging (0.992)
USA	European American	T > C	1346	1307	436	Q > R	9/11	Tolerated (0.27)	Benign (0.423)
SA	African	C > T	1357	1318	440	E > K	9/11	Deleterious (0.05)	Possibly damaging (0.858)

Table 5. *PKLR* missense variants detected in MTN-001 participants. A total of 15 previously unreported *PKLR* missense variants were observed in 15 heterozygous MTN-001 participants for the coding DNA reference sequence NM_000298.5. The functional consequence of resulting amino acid substitutions were predicted using SIFT and PolyPhen in silico tools. A SIFT score < 0.05 was suggestive of a damaging amino acid substitution and > 0.05 a tolerated substitution. A PolyPhen score > 0.908 was suggestive of a probably damaging, 0.447-0.908 a possibly damaging, or < 0.447 a benign amino acid substitution. Deleterious and probably damaging *PKLR* missense variants was observed at a frequency of 3% (4/142 individuals).

Discussion

This study identified the nucleotide kinases that activate TFV in cells and tissues susceptible to HIV infection. Our data suggests that AK2 may be a key contributor to systemic and localized TFV activation as siRNA knockdown in PBMC, vaginal tissue, and colorectal tissue resulted in significantly decreased formation of TFV metabolites. Additionally, we demonstrated PKLR can contribute to TFV-DP formation in PBMC and vaginal tissue. PKLR is highly expressed in the liver and therefore may be critical for the activation of oral TFV preparations that undergo first-pass metabolism. Interestingly, we observed CKM protein expression to be limited to colorectal tissue. TFV-DP concentrations in colon exceed those in vaginal tissue with an oral dose of TFV and tissue-specific expression of CKM could contribute to this phenomenon. Further, although these data do not comprehensively explain the increased incidence of HIV PrEP failure in heterosexual individuals relative to men who have sex with men, our findings are in support of a genetic basis for the reported "colon advantage" described for tenofovir tissue distribution. Additionally in this study, we examined a potential role for the nucleotide diphosphate kinase NME1. We did not detect NME1 expression at the protein level in PBMC, vaginal, or colorectal tissue, suggesting NME1 is unlikely to contribute to the activation of TFV in the cells and tissues investigated.

Through our work, we identified *AK2*, *CKM*, *PKM*, and *PKLR* as candidates for examination in a retrospective clinical study. In doing so, we detected 71 previously unreported variants in the genes encoding these kinases. The coverage threshold implemented in our analyses was in line with the American College of Medical Genetics

and Genomics clinical laboratory standards for next-generation sequencing, increasing the confidence in the variants called.(23) These discovered variants, however, were not validated in parallel using Sanger sequencing. We detected seven genetic variants in *CKM*, *PKM*, and *PKLR* that have been reported in the SNP database. The *CKM* SNPs rs11559024 and rs17357122 detected in MTN-001 European American participants have frequencies of 1 – 3% in Western European populations as reported by the 1000 Genomes Project.(24) These populations also exhibit a comparable frequency for the *PKM* SNP rs180716407 detected in one European American participant, and African sub-populations of Nigeria, Kenya, and Sierra Leone have a frequency of 1 – 2% for the *PKLR* SNP rs147689373 detected in one South African participant. Population genetics aside, the impact of these discovered and reported genetic variants on enzymatic activity is unknown. For the detected missense variants, however, we were able to predict the phenotypic consequence of resulting amino acid mutations using in the silico bioinformatic tools SIFT and PolyPhen. For example, one MTN-001 participant carried the *CKM* missense variant NM_001824.4:c.389G>A, causing a deleterious and damaging amino acid mutation of R130H. In line with this, a study characterizing TFV-MP binding within the active site of CKM observed this particular amino acid residue R130 to form strong ionic interactions with its substrates.(19) Moreover, one can envision that such a mutation may interfere with substrate binding and, therefore, decrease rates of phosphorylation. That being said, the variants predicted in our study to negatively impact kinase function ultimately need to be recapitulated in vitro using site-directed mutagenesis to test their direct consequence on activity towards TFV and TFV-MP.

Due to the frequency of the genetic variants detected within the MTN-001 participants, we were unable to make strong correlations with our published TFV pharmacokinetic data.(11) Additionally, adherence is a confounding issue for HIV PrEP studies making it particularly difficult to execute these analyses in a retrospective study. As a proof of concept, however, it is worth noting an African American participant carrying a predicted dysfunctional missense variant for *PKLR* exhibited a three-fold greater ratio of TFV to TFV-DP in vaginal tissue compared to homozygous wild-type participants with daily use of a 1% TFV microbicide gel and is commensurate with lower TFV-DP tissue concentrations. In order to perform a powerful analysis, a pharmacokinetic study design is required in which healthy volunteers would be enrolled based on genotype in the same manner used for our recent study of the anti-HIV drug maraviroc.(25) Further, as this preliminary pharmacogenomics study was limited to females it would also be of interest to perform a similar analysis in men in order to investigate potential sexual dimorphisms in allele frequencies.

In conclusion, our results present a fundamental shift when considering the factors that govern TFV disposition as differing routes of activation could contribute to tissue-specific pharmacokinetic-pharmacodynamic relationships. Further, in identifying the nucleotide kinases responsible for TFV activation in PBMC, vaginal tissue, and colorectal tissue, we were able to perform targeted sequencing of the genes encoding these kinases using clinical samples of the MTN-001 Microbicide Trials Network study. We detected genetic variants in these kinases predicted to have deleterious and damaging phenotypes, demonstrating that there could be a genetic basis for inter-individual

variation in TFV drug levels. Taken together, the results from this study are pushing an important concept forward in that HIV PrEP is not a one-size-fits-all preventative approach, and these data can guide future clinical studies to investigate the impact of nucleotide kinase genetic variants on TFV pharmacokinetics.

References

1. Schooley RT, Ruane P, Myers RA, Beall G, Lampiris H, Berger D, et al. Tenofovir DF in antiretroviral-experienced patients: results from a 48-week, randomized, double-blind study. AIDS. 2002;16(9):1257-63.

2. Robbins BL, Srinivas RV, Kim C, Bischofberger N, Fridland A. Anti-human immunodeficiency virus activity and cellular metabolism of a potential prodrug of the acyclic nucleoside phosphonate 9-R-(2-phosphonomethoxypropyl)adenine (PMPA), Bis(isopropyloxymethylcarbonyl)PMPA. Antimicrob Agents Chemother. 1998;42(3):612-7. PMCID: 105507.

3. Baeten JM, Donnell D, Ndase P, Mugo NR, Campbell JD, Wangisi J, et al. Antiretroviral prophylaxis for HIV prevention in heterosexual men and women. N Engl J Med. 2012;367(5):399-410. PMCID: 3770474.

4. Mayer KH, Maslankowski LA, Gai F, El-Sadr WM, Justman J, Kwiecien A, et al. Safety and tolerability of tenofovir vaginal gel in abstinent and sexually active HIV-infected and uninfected women. AIDS. 2006;20(4):543-51.

5. Anton PA, Cranston RD, Kashuba A, Hendrix CW, Bumpus NN, Richardson-Harman N, et al. RMP-02/MTN-006: A phase 1 rectal safety, acceptability, pharmacokinetic, and pharmacodynamic study of tenofovir 1% gel compared with oral

tenofovir disoproxil fumarate. AIDS Res Hum Retroviruses. 2012;28(11):1412-21. PMCID: 3484811.

6. Derdelinckx I, Wainberg MA, Lange JM, Hill A, Halima Y, Boucher CA. Criteria for drugs used in pre-exposure prophylaxis trials against HIV infection. PLoS Med. 2006;3(11):e454. PMCID: 1630715.

7. Louissaint NA, Cao YJ, Skipper PL, Liberman RG, Tannenbaum SR, Nimmagadda S, et al. Single dose pharmacokinetics of oral tenofovir in plasma, peripheral blood mononuclear cells, colonic tissue, and vaginal tissue. AIDS Res Hum Retroviruses. 2013;29(11):1443-50.

8. Grant RM, Lama JR, Anderson PL, McMahan V, Liu AY, Vargas L, et al. Preexposure chemoprophylaxis for HIV prevention in men who have sex with men. N Engl J Med. 2010;363(27):2587-99. PMCID: 3079639.

9. Van Damme L, Corneli A, Ahmed K, Agot K, Lombaard J, Kapiga S, et al. Preexposure prophylaxis for HIV infection among African women. N Engl J Med. 2012;367(5):411-22. PMCID: 3687217.

10. Marrazzo JM, Ramjee G, Richardson BA, Gomez K, Mgodi N, Nair G, et al. Tenofovir-based preexposure prophylaxis for HIV infection among African women. N Engl J Med. 2015;372(6):509-18.

11. Hendrix CW, Chen BA, Guddera V, Hoesley C, Justman J, Nakabiito C, et al. MTN-001: randomized pharmacokinetic cross-over study comparing tenofovir vaginal gel and oral tablets in vaginal tissue and other compartments. PLoS One. 2013;8(1):e55013. PMCID: 3559346.

12. Patterson KB, Prince HA, Kraft E, Jenkins AJ, Shaheen NJ, Rooney JF, et al. Penetration of tenofovir and emtricitabine in mucosal tissues: implications for prevention of HIV-1 transmission. Sci Transl Med. 2011;3(112):112re4.

13. Kearney BP, Flaherty JF, Shah J. Tenofovir disoproxil fumarate: clinical pharmacology and pharmacokinetics. Clin Pharmacokinet. 2004;43(9):595-612.

14. Nobumoto M, Yamada M, Song S, Inouye S, Nakazawa A. Mechanism of mitochondrial import of adenylate kinase isozymes. J Biochem. 1998;123(1):128-35.

15. Robbins BL, Greenhaw J, Connelly MC, Fridland A. Metabolic pathways for activation of the antiviral agent 9-(2-phosphonylmethoxyethyl)adenine in human lymphoid cells. Antimicrob Agents Chemother. 1995;39(10):2304-8. PMCID: 162933.

16. Topalis D, Alvarez K, Barral K, Munier-Lehmann H, Schneider B, Veron M, et al. Acyclic phosphonate nucleotides and human adenylate kinases: impact of a borano group on alpha-P position. Nucleosides Nucleotides Nucleic Acids. 2008;27(4):319-31.

17. Bourdais J, Biondi R, Sarfati S, Guerreiro C, Lascu I, Janin J, et al. Cellular phosphorylation of anti-HIV nucleosides. Role of nucleoside diphosphate kinase. J Biol Chem. 1996;271(14):7887-90.

18. Koch K, Chen Y, Feng JY, Borroto-Esoda K, Deville-Bonne D, Gallois-Montbrun S, et al. Nucleoside diphosphate kinase and the activation of antiviral phosphonate analogs of nucleotides: binding mode and phosphorylation of tenofovir derivatives. Nucleosides Nucleotides Nucleic Acids. 2009;28(8):776-92.

19. Varga A, Graczer E, Chaloin L, Liliom K, Zavodszky P, Lionne C, et al. Selectivity of kinases on the activation of tenofovir, an anti-HIV agent. Eur J Pharm Sci. 2013;48(1-2):307-15.

20. Gentry BG, Gentry SN, Jackson TL, Zemlicka J, Drach JC. Phosphorylation of antiviral and endogenous nucleotides to di- and triphosphates by guanosine monophosphate kinase. Biochem Pharmacol. 2011;81(1):43-9.

21. Ng PC, Henikoff S. Predicting deleterious amino acid substitutions. Genome Res. 2001;11(5):863-74. PMCID: 311071.

22. Ramensky V, Bork P, Sunyaev S. Human non-synonymous SNPs: server and survey. Nucleic Acids Res. 2002;30(17):3894-900. PMCID: 137415.

23. Rehm HL, Bale SJ, Bayrak-Toydemir P, Berg JS, Brown KK, Deignan JL, et al. ACMG clinical laboratory standards for next-generation sequencing. Genet Med. 2013;15(9):733-47. PMCID: 4098820.

24. Abecasis GR, Auton A, Brooks LD, DePristo MA, Durbin RM, Handsaker RE, et al. An integrated map of genetic variation from 1,092 human genomes. Nature. 2012;491(7422):56-65. PMCID: 3498066.

25. Lu Y, Fuchs EJ, Hendrix CW, Bumpus NN. CYP3A5 genotype impacts maraviroc concentrations in healthy volunteers. Drug Metab Dispos. 2014;42(11):1796-802. PMCID: 4201129.

Chapter 7: Final Conclusions

With the advent of antiretroviral drug therapy in the late 1980s, human immunodeficiency virus (HIV) is no longer a death sentence, but remains to be a chronic disease. Of concern, however, an estimated 2.1 million individuals were newly infected with HIV globally as of 2015. Further, HIV remains to be a pandemic that requires attention from scientific researchers to push forward the development of novel drug therapies that mitigate viral resistance and improve overall safety profiles.

Rilpivirine (RPV), a second generation non-nucleoside reverse transcriptase inhibitor (NNRTI), was FDA approved in 2011 for administration to treatment-naïve HIV-infected individuals. We were the first to characterize and publish the human biotransformation of RPV. A reverse phase ultra-high performance liquid chromatography-tandem mass spectrometry assay was developed in order to detect RPV and characterize its polar metabolites using fragmentation spectra. By *in vitro* assay, we observed the cytochrome P450s CYP3A4 and CYP3A5 primarily contributed to the oxidative metabolism of RPV and the uridine diphosphate glucuronosyl transferases UGT1A1 and UGT1A4 could contribute to the conjugation of RPV and its metabolites. In addition to this work, we also developed and published a targeted metabolomics screen allowing for the investigation of intracellular small molecule homeostasis that may be impacted by chronic antiretroviral therapy. Further, these studies most importantly laid the foundation for the bioanalysis of RPV and its metabolites in the plasma of HPTN 076 study participants in addition to guiding the selection of drug metabolizing enzymes specific to RPV for next-generation sequencing.

In the former studies, it was observed RPV could modulate CYP3A4 mRNA expression through activation of the nuclear receptor and xenobiotic sensor pregnane X receptor (PXR). In line with this, efavirenz (EFV) a first generation NNRTI and the most-widely prescribed antiretroviral despite exhibiting a poor safety profile, was observed to be a more potent activator of PXR. Using an extensive panel of sixteen analogs, we explored the structure-activity relationship of EFV and PXR. These analyses primarily required the use of primary mouse hepatocytes in order to study PXR target gene modulation and required the development of a luciferase reporter assay to test for direct activation of the receptor. In doing so, we identified a lower size limit ranging from < 223 Da to > 289 Da for ligand-dependent activation of PXR. In addition, we observed that the incorporation of a hydroxyl group onto a PXR agonist did not impede ligand binding but attenuated PXR activation potentially through destabilizing a key hydrophobic area within the ligand-binding pocket. These findings may inform next-generation NNRTI development in order to dial out PXR activation to mitigate unwanted drug-drug interactions.

Building upon this work, we investigated other hepatic pathways that may be stimulated by EFV and/or impacted by PXR activation. To this end, we observed EFV, but not RPV, could disrupt hepatic cholesterol homeostasis by stimulating lipid droplet formation as evidenced in treatment of primary mouse hepatocytes. We were unable to be recapitulate this observation in primary human hepatocytes suggesting potential species-specific differences leading to the formation of this phenotype. EFV was also observed to increase the expression of the nuclear receptor small heterodimer partner (SHP), which has been implicated in facilitating the formation of dyslipidemia. That being said, further

studies need to be performed in order to determine whether an EFV-mediated increase of SHP has a causal role in lipid droplet formation.

In addition to studying antiretrovirals within the context of chronic HIV maintenance therapy, we also investigated RPV and the nucleoside reverse transcriptase inhibitor tenofovir (TFV) as pharmacological agents for HIV pre-exposure prophylaxis (PrEP). Moreover, in retrospective analyses using clinical samples from the HIV Prevention Trials Network Study HPTN 076 and the Microbicide Trials Network study MTN-001, we identified genetic variants in the genes encoding enzymes responsible for RPV metabolism (60 previously reported genetic variants in *CYP3A4*, *CYP3A5*, *UGT1A1* and *UGT1A4*) and TFV activation (71 previously unreported genetic variants in *AK2*, *CKM*, *PKM* and *PKLR*), respectively. These findings push an important concept forward of personalizing HIV therapy and PrEP by highlighting the potential contribution of genetic polymorphisms to pharmacokinetic inter-individual variability and drug-associated toxicity.

Julie Maylor Lade
(Formerly Julie Anne Maylor)
725 North Wolfe Street, Biophysics 307, Baltimore, MD 21205
443-823-3024
jmaylor1@jhmi.edu

Education

Doctorate of Philosophy Candidate, Pharmacology, Johns Hopkins University School of Medicine, Baltimore, MD, October 2016

Bachelor of Science, Chemistry, Gettysburg College, Gettysburg, PA, May 2009

Undergraduate Theses: Modification of Tripodal Tridentate N_3 Ligands to Complex $Re(CO)_3$; Copper (II) and α-Synuclein: Insight into the Mechanism of Parkinson's Disease Cumulative GPA: 3.72, Major GPA: 3.79

Research Experience

Doctorate of Philosophy Candidate, August 2012 – Present

Johns Hopkins University School of Medicine, Department of Pharmacology & Molecular Sciences under the mentorship of Dr. Namandjé N. Bumpus

Concentration: Drug metabolism and disposition of anti-HIV drugs in humans primarily through use of biological samples and isolated primary hepatocytes in conjunction with in vitro and in vivo studies performed using a murine animal model.

Genentech Graduate Student Intern, June – August 2015

Genentech, Department of Clinical Pharmacology under the supervision of Dr. Joseph A. Ware

Concentration: Investigation of the pharmacokinetics and pharmacodynamics of the third generation non-steroidal aromatase inhibitor, letrozole, in order to develop a

physiologically-based pharmacokinetic model using Simcyp.

Research Technologist, October 2009 – July 2012

Johns Hopkins University School of Medicine, Department of Pulmonary and Critical Care Medicine under the supervision of Dr. Larissa A. Shimoda

Concentration: Investigation of the molecular mechanism for hypoxic pulmonary hypertension mediated by the transcription factor, hypoxia-inducible factor 1α, and its effects on the regulation of and interaction with other key proteins in the pulmonary vasculature.

National Institutes of Health Undergraduate Student Intern, May – August 2007 and May – August 2008

National Heart, Lung and Blood Institute, Laboratory of Protein Conformation and Dynamics under the mentorship of Dr. Jennifer C. Lee

Concentration: Organic synthesis of fluorescent molecular probes for use in aggregational studies investigating structural dynamics of α-synuclein, a hallmark protein of Parkinson's Disease pathogenesis.

Research Skills

- Small molecule metabolite identification within the context of cytochrome P450- and uridine diphosphate glucuronosyltransferase-dependent metabolism using ultra-high performance liquid chromatography-mass spectrometry
- Evaluation of drug distribution in situ using matrix-assisted laser desorption ionization-mass spectrometry imaging

- Study of the transcriptional and translational regulation of the cytochromes P450 primarily mediated by pregnane X receptor activation
- Additional Technical and Experimental Skills – Proficient in the isolation of primary mouse hepatocytes, cell culture of primary isolates and cell lines, luciferase reporter assays, protein expression and purification, cell viability assays, P450 enzyme kinetic assays, P450 inhibition assays, drug-drug interaction studies, OCT1/OCT2 drug transporter uptake assays, siRNA and plasmid DNA transfections, qualitative and quantitative real-time PCR, intrinsic tryptophan quenching assays, isothermal titration calorimetry, sample preparation of genomic DNA from biological samples and sequencing of DNA using MiSeq benchtop next-generation sequencer, immunoblotting, immunoprecipitation, immunocytology, immunohistology, confocal and fluorescent microscopy

Awards and Honors

- American Society for Pharmacology and Experimental Therapeutics Division of Drug Metabolism Graduate Student Best Abstract Competition, First Place: Spring 2016
- American Society for Pharmacology and Experimental Therapeutics Division of Drug Metabolism Graduate Student Best Abstract Competition, First Place: Spring 2015
- American Society for Pharmacology and Experimental Therapeutics Graduate Student Travel Award: Spring 2015
- Johns Hopkins University Pharmacology and Molecular Sciences Scheinberg Travel Award: Fall 2013
- American Chemical Society Certification: Spring 2009

- Outstanding College Chemistry Major Award for the Southeastern Pennsylvania Section of the American Chemical Society: Spring 2009
- Gettysburg College Departmental Honors in Chemistry: Spring 2009
- Gettysburg College Magna Cum Laude: Spring 2009
- Gettysburg College Dean's List: Spring 2006, Fall 2006, Fall 2007, Spring 2008
- Gettysburg College Dean's Commendation List: Fall 2005, Fall 2008

Fellowships

- Pharmaceutical Research and Manufacturers of America Foundation Pre Doctoral Fellowship in Pharmacology/Toxicology: Awarded January 1, 2015 to December 31, 2016

Professional Society Memberships

- American Society for Pharmacology and Experimental Therapeutics: Fall 2014 – Present

Extracurricular Activities

- Founding and active member of the Pharmacology Student Initiative, a student-lead organization established for facilitating comradery amongst graduate students and faculty within the department of Pharmacology & Molecular Sciences: Spring 2015 – Present

Peer Reviewed Publications

1. **Lade JM**, To EE, Hendrix CW, Bumpus NN. Discovery of Genetic Variants of the Kinases that Activate Tenofovir in a Compartment-specific Manner. EBioMedicine. 2015 Jul 9;2(9):1145-52. doi: 10.1016/j.ebiom.2015.07.008. eCollection 2015 Sep.
2. Lai N, **Lade J**, Leggett K, Yun X, Baksh S, Chau E, Crow MT, Sidhaye V, Wang J, Shimoda LA. The aquaporin 1 C-terminal tail is required for migration and growth of pulmonary arterial myocytes. Am J Respir Cell Mol Biol. 2014 Jun;50(6):1010-20. doi: 10.1165/rcmb.2013-0374OC. PubMed Central PMID: 24328827.
3. **Lade JM**, Avery LB, Bumpus NN. Human biotransformation of the nonnucleoside reverse transcriptase inhibitor rilpivirine and a cross-species metabolism comparison. Antimicrob Agents Chemother. 2013 Oct;57(10):5067-79. doi:10.1128/AAC.01401-13. PubMed PMID: 23917319.
4. Pisarcik S, **Maylor J**, Lu W, Yun X, Undem C, Sylvester JT, Semenza GL, Shimoda LA. Activation of hypoxia-inducible factor-1 in pulmonary arterial smooth muscle cells by endothelin-1. Am J Physiol Lung Cell Mol Physiol. 2013 Apr 15;304(8):L549-61. doi: 10.1152/ajplung.00081.2012. Epub 2013 Feb 15. PubMed PMID: 23418090; PubMed Central PMCID: PMC3625988.
5. Undem C, Rios EJ, **Maylor J**, Shimoda LA. Endothelin-1 augments Na^+/H^+ exchange activity in murine pulmonary arterial smooth muscle cells via Rho kinase. PLoS One. 2012;7(9):e46303. doi: 10.1371/journal.pone.0046303. Epub

2012 Sep 28. PubMed PMID: 23029469; PubMed Central PMCID: PMC3460862.

6. Leggett K, **Maylor J**, Undem C, Lai N, Lu W, Schweitzer K, King LS, Myers AC, Sylvester JT, Sidhaye V, Shimoda LA. Hypoxia-induced migration in pulmonary arterial smooth muscle cells requires calcium-dependent upregulation of aquaporin 1. Am J Physiol Lung Cell Mol Physiol. 2012 Aug 15;303(4):L343-53. doi:10.1152/ajplung.00130.2012. Epub 2012 Jun 8. PubMed PMID: 22683574; PubMed Central PMCID: PMC3423828.
7. Luke T, **Maylor J**, Undem C, Sylvester JT, Shimoda LA. Kinase-dependent activation of voltage-gated Ca2+ channels by ET-1 in pulmonary arterial myocytes during chronic hypoxia. Am J Physiol Lung Cell Mol Physiol. 2012 May 15;302(10):L1128-39. doi: 10.1152/ajplung.00396.2011. Epub 2012 Mar 2. PubMed PMID: 22387294; PubMed Central PMCID: PMC3362260.
8. Abud EM, **Maylor J**, Undem C, Punjabi A, Zaiman AL, Myers AC, Sylvester JT, Semenza GL, Shimoda LA. Digoxin inhibits development of hypoxic pulmonary hypertension in mice. Proc Natl Acad Sci U S A. 2012 Jan 24;109(4):1239-44. doi: 10.1073/pnas.1120385109. Epub 2012 Jan 9. PubMed PMID: 22232678; PubMed CentralPMCID: PMC3268303.

Abstracts

1. **Lade JM** and **Bumpus NN.** Structure-Activity Analysis of Efavirenz-Mediated Activation of Pregnane X Receptor. FASEB J 30: 713.8, 2016.

2. **Lade JM**, Hendrix CW and **Bumpus NN.** Pharmacogenetic Analysis of Nucleotide Kinases that Metabolize the Antiviral Drug Tenofovir. FASEB J 29: 940.4, 2015.
3. **Lade JM** and **Bumpus NN.** Structure-Activity Analysis of Efavirenz-Mediated Modulation of Pregnane X Receptor Target Genes. FASEB J 29: 778.7, April 2015.
4. **Lade JM, Avery LA, Bumpus NN.** Characterization of the Biotransformation of the HIV Non-Nucleoside Reverse Transcriptase Inhibitor Rilpivirine. Drug Metabolism Reviews, Abstracts from the 10th International ISSX Meeting 45:1-286, 2014.
5. **Maylor J**, Zaiman A and Shimoda LA. Endogenous and pharmacological inhibition of calpain decreases migration of hypoxic pulmonary arterial smooth muscle cells (PASMCs). FASEB J 26:873.11, 2012.
6. Lai N, **Maylor J**, Leggett K, Undem C, Crow M, and Shimoda LA. Aquaporin 1(AQP1) Mediates Migration and Growth in Pulmonary Arterial Smooth Muscle Cells (PASMCs). FASEB J 26:871.1, 2012.
7. **Maylor J**, Undem C, Crow MT and Shimoda LA. Over-expression of wild-type Na^+/H^+ exchanger isoform 1 (NHE1) in Pulmonary Arterial Smooth Muscle Cells (PASMCs) Stimulates Migration and Growth. FASEB J 25: 1034.16, 2011.
8. Undem C, **Maylor J**, Sylvester JT, Semenza GL, and Shimoda LA. Acriflavine Attenuates the Development of Hypoxic Pulmonary Hypertension. FASEB J 25: 1034.15, 2011.

9. Leggett K, **Maylor J** and Shimoda LA. AQP1 plays a critical role in hypoxia-induced migration of pulmonary arterial smooth muscle cells. FASEB J 25:1034.13, 2011.
10. **Maylor JA**, Lu W, Pisarcik S, Walker J, Undem C, Myers AC and Shimoda LA. Reciprocal regulation of Na^+/H^+ exchanger isoform 1 (NHE1) and Na^+/H^+ exchange regulatory factor 1 (NHERF1) in Hypoxic Pulmonary Arterial Smooth Muscle Cells (PASMCs). FASEB J 24:1023.24, 2010.

Oral Presentations

Julie Lade, David Li and Namandjé Bumpus. January 13, 2016. Working Toward Personalizing HIV Treatment and Chemoprevention. Partnering Toward Discovery seminar series. Johns Hopkins University School of Medicine in Baltimore, MD.

Julie M. Lade, Craig W. Hendrix and Namandjé N. Bumpus. August 13, 2015. Pharmacogenetic Analysis of Nucleotide Kinases that Metabolize the Antiviral Drug Tenofovir. Invited talk by Dr. Bill Smith, Senior Director of Drug Metabolism. Gilead Sciences, Inc. Department of Drug Metabolism in Foster City, CA.

Julie M. Lade, Craig W. Hendrix and Namandjé N. Bumpus. March 30, 2015. Pharmacogenetic Analysis of Nucleotide Kinases that Metabolize the Antiviral Drug Tenofovir. Drug Metabolism Division's platform session on Biotransformation and Drug Transport. Experimental Biology Conference in Boston, MA.

Poster Presentations

Julie M. Lade, Herschel Wade and Namandjé N. Bumpus. April 2016. Structure-Activity Analysis of Efavirenz-Mediated Activation of Pregnane X Receptor. Presented at the Experimental Biology Conference in San Diego, CA.

Julie M. Lade, Craig W. Hendrix and Namandjé N. Bumpus. March 2015. Pharmacogenetic Analysis of Nucleotide Kinases that Metabolize the Antiviral Drug Tenofovir. Presented at the Experimental Biology Conference in Boston, MA.

Julie M. Lade and Namandjé N. Bumpus. March 2015. Structure-Activity Analysis of Efavirenz-Mediated Modulation of Pregnane X Receptor Target Genes. Presented at the Experimental Biology Conference in Boston, MA.

Julie M. Lade and Namandjé N. Bumpus. May 2014. Comparison of the Metabolism of the Anti-HIV Drug Rilpivirine in Sex- and Age-Matched Primary Mouse Hepatocytes. Presented at the Microsomes and Drug Oxidations 20th International Symposium in Stuttgart, Germany.

Julie M. Lade, Lindsay B. Avery and Namandjé N. Bumpus. September 2013. Characterization of the Biotransformation of the HIV Non-Nucleoside Reverse Transcriptase Inhibitor Rilpivirine. Presented at the International Society for the Study of Xenobiotics in Toronto, Ontario, Canada.

Julie Maylor, Ari Zaimen and Larissa A. Shimoda, April 2012. Endogenous and pharmacological inhibition of calpain decreases migration of hypoxic pulmonary arterial smooth muscle cells (PASMCs). Presented at the Experimental Biology Conference in San Dieogo, CA.

Julie Maylor, Clark Undem, Michael T. Crow and Larissa A. Shimoda, April 2011. Over-expression of wild-type Na^+/H^+ exchanger isoform 1 in Pulmonary Arterial Smooth Muscle Cells Stimulates Migration and Growth. Presented at the Experimental Biology Conference in Washington D.C.

Julie Maylor, Wenju Lu, Sarah Pisarcik, Jasmine Walker, Clark Undem, Allen C. Myers and Larissa A. Shimoda, April 2010. Reciprocal regulation of Na^+/H^+ exchanger isoform 1 and Na^+/H^+ exchange regulatory factor 1 in Hypoxic Pulmonary Arterial Smooth Muscle Cells. Presented at the Experimental Biology Conference in Anaheim, CA.